Study of the decay $B^0 \to K_S^0 \pi^0$ at Belle II

A Thesis

Submitted to the

Tata Institute of Fundamental Research, Mumbai

for the degree of Doctor of Philosophy

in Subject Board of Physics

by

Sagar Hazra

Department of High Energy Physics

Tata Institute of Fundamental Research

Mumbai

February, 2024

Final Version Submitted in February, 2024

Dedicated to my parents

Declaration

This thesis is a presentation of my original research work. Wherever contributions of others are involved, every effort is made to indicate this clearly, with due reference to the literature, and acknowledgement of collaborative research and discussions.

The work was done under the guidance of Professor Gagan Mohanty at the Tata Institute of Fundamental Research, Mumbai, India.

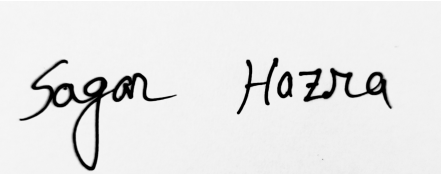

[**Sagar Hazra**]
Date: 28th February 2024

In my capacity as supervisor of the candidate's thesis, I certify that the above statements are true to the best of my knowledge.

[**Prof. Gagan Mohanty**]
Date: 28th February 2024

Acknowledgment

I want to convey my gratitude and heartfelt appreciation to all those who have supported and provided guidance throughout my journey in completing this thesis. Their invaluable support and encouragement were vital in making this research project a reality. First and foremost, I extend my heartfelt gratitude to Prof. Gagan Mohanty, my thesis advisor, for granting me the opportunity to participate in the Belle II experiment. His patient guidance, enthusiastic encouragement, and valuable, constructive suggestions throughout the planning and development of this project work were indispensable in making this thesis a reality. He has provide me the opportunity to work independently and offered essential emotional support during challenging moments. He also offered strong encouragement to work from home during the COVID pandemic, which greatly aided in advancing my progress on the thesis. Fortunately, throughout my entire Ph.D. journey, I received his dedicated attention for reviewing papers and documents in addition to his numerous responsibilities. He has been highly efficient in taking care of all my official requirements without any inconvenience. He has offered numerous experimental and theoretical explanations that further deepened my interest in this field.

I want to convey my deep appreciation to Prof. Martin Sevior for his outstanding support and assistance in ensuring the success of my second project. I would also like to extend my gratitude to Dr. Diego Tonelli for his dedicated attention in helping me make plans and providing valuable suggestions. At times, he may have made my life challenging by constantly pushing me to achieve the highly sought-after Belle's results, but at the end, this drive played a crucial role in completing my Ph.D. in time.

I extend my thanks to every member of the Belle II collaboration for their unwavering dedication to ensure the experiment's smooth operation through their continuous hard work. In particular, I express my gratitude to Prof. Takeo Higuchi and Dr. Thibuad Humair, the convenors of the time-dependent analysis group, for their consistent review and valuable suggestions. I would also like to express my appreciation to the charmless group convenors, Dr. Mirco Dorigo and Dr. Pablo Goldenzweig, for their helpful suggestions and comments. I would like to extend my thanks to my internal reviewers, Prof. Takeo Higuchi, Prof. Anjan Giri, and Prof. Chunhui Chen, for their thorough review of my internal note and paper. I also wish to express my gratitude to Prof. Andrzej Bozek and Dr. Jitendra Kumar for contributing vital ideas and suggestions that played a key role in the success of my first project.

I thank TIFR Mumbai and the Department of High Energy Physics for offering me an exceptional opportunity and the necessary infrastructure to complete this work. I wish to express my appreciation to my doctoral thesis monitoring committee, comprised of Prof. Gagan Mohanty, Prof. Venugopal Achanta, and Prof. Pravata Kumar Mohanty, for their invaluable comments and suggestions throughout the duration of my Ph.D.

It is with immense pleasure that I express my gratitude to my colleagues and seniors from the DHEP-TIFR group. I extend a special appreciation to Dr. Abdul Basith Kaliyar for his unwavering support and assistance throughout my Ph.D. journey. He has been instrumental in assisting me with formulating plans and navigating challenging academic pressures. I would also like to express my gratitude to Soumen and Debashis for their assistance during the early phase of my Ph.D. journey. I am also appreciative of the assistance provided by other members of the DHEP group, namely Rahul, Abhradeep, Mintu, Rishabh, and Pruthvi. I also wish to express my gratitude to Samikshya for her collaboration and assistance.

I also greatly enjoyed my time in Mumbai, as the city offers a wealth of attractions to visit, excellent restaurants to dine at, and access to skilled medical professionals for healthcare needs.

I am also filled with gratitude for my parents, Krishna and Barnali, and my brother, Subha, for their unconditional love and support. I am grateful for the support that I have received from my girlfriend, Jayashri, over the past five years.

I would like to express my gratitude to my friends Supriya, Purna, Suman, Sebabrata, Rajesh, and Vivek for regularly engaging in phone conversations with me as we have been geographically separated due to our respective professions.

Abstract

The $B^0 \to K_S^0\pi^0$ decay is dominated by $b \to s$ loop amplitudes. Such flavor-changing-neutral-current transitions are highly suppressed in the standard model and provide an indirect route to search for new physics. The excellent neutral-particle reconstruction capability of Belle II allows a unique measurement of *CP* violation asymmetry in this neutral *B*-meson decay channel as an important consistency test of the standard model. We perform a measurement of the *CP*-violating parameters C and S in $B^0 \to K_S^0\pi^0$ at Belle II using a sample of 387×10^6 $B\bar{B}$ events recorded in e^+e^- collisions at a center-of-mass energy corresponding to the $\Upsilon(4S)$ resonance. These parameters are determined by fitting the proper decay-time distribution of a sample of 415 signal events. We obtain $\mathcal{B} = (11.15^{+0.69}_{-0.67} \pm 0.61) \times 10^{-6}$, $C = -0.04^{+0.14}_{-0.15} \pm 0.05$ and $S = 0.75^{+0.20}_{-0.23} \pm 0.04$, where the first uncertainties are statistical and the second are systematic. In the latter part, we report a particle identification (PID) framework developed based on ionization energy loss information in the silicon-strip vertex detector (SVD) of Belle II for charged pions and kaons using $D^{*+} \to D^0(\to K^-\pi^+)\pi^+$ decay samples. The introduction of additional information from the SVD is found to improve the overall PID performance in the low momentum region.

Publications and public documents

1. Measurement of *CP* violation in $B^0 \to K_S^0\pi^0$ decays at Belle II, Phys. Rev. Lett. **131**, 111803 (2023).

2. The Design, Construction, Operation and Performance of the Belle II Silicon Vertex Detector, JINST **17**, P11042 (2022).

3. First decay-time-dependent analysis of $B^0 \to K_S^0\pi^0$ at Belle II, Belle II Public Document, arXiv:2206.07453.

4. Low-momentum charged hadron identification using SVD, Belle II Public Document, BELLE2-NOTE-PL-2020-028.

Belle II Internal Note

1. S. Hazra, G. B. Mohanty and A. B. Kaliyar, Belle II Analysis Note on "Measurements of *CP* violation in $B^0 \to K_S^0\pi^0$ decays at Belle II", BELLE2-NOTE-PH-2022-065.

2. S. Hazra, A. B. Kaliyar and G. B. Mohanty, Belle II Technical Note on "Low-momentum charged hadron identification using SVD", BELLE2-NOTE-TE-2020-019.

List of Figures

1.1 Experimental constraints of the CKM triangle in the $\bar{\rho} - \bar{\eta}$ plane [16]. 7

1.2 Dominant box diagrams for the $B_q^0 - \overline{B_q^0}$ transitions ($q = d$ or s). 8

1.3 Feynman diagram of the dominant amplitude contributing to $B^0 \to K_S^0 \pi^0$. . . . 10

1.4 Summary of experimental results of CP violation in the $B^0 \to K_S^0 \pi^0$ decay. . . . 12

2.1 A schematic diagram of the SuperKEKB collider. 14

2.2 A schematic diagram of the Belle II detector. 15

2.3 The configuration of the entire PXD support framework, including the installed sensor ladders and external services. 16

2.4 Belle II SVD with its complete set of four layers. 17

2.5 Comparison between wire configurations of the (top) Belle II and (bottom) Belle CDC [44]. 19

2.6 A schematic view of the TOP counter module (top) and of its principle of operation (bottom) [47]. 20

2.7 The principle of PID operation (left) of the proximity focusing with non-homogeneous aerogel radiator (right) of the ARICH subdectector [50]. 21

3.1 Reconstructed K_S^0 mass distribution for signal and background events. 25

3.2 Reconstructed photon energy distributions for backward-endcap (upper-left), barrel (upper-right), and forward-endcap (lower) ECL region. 26

3.3 Reconstructed π^0 mass (left) and $|\cos\theta_{\rm hel}|$ (right) distributions. 27

3.4 $M_{\rm bc}$ and ΔE distributions of signal B candidates. 27

3.5 2D scatter plots ΔE–$M_{\rm bc}$ (left) and ΔE–$M'_{\rm bc}$ (right) for signal (upper), $B\overline{B}$ (middle) and $q\overline{q}$ (lower) events. 29

3.6 B-candidate multiplicity distribution in the signal simulated sample. 30

4.1 BDT output distributions (left) for signal and background events and ROC curve (right) for background rejection vs. signal efficiency. 33
4.2 M'_{bc} and ΔE distributions obtained after the continuum suppression. 34
4.3 C'_{BDT} distribution for the signal simulated sample. 34
4.4 M'_{bc} and ΔE distributions for $B\overline{B}$ background events. 35

5.1 $q \cdot r$ distributions for signal and background in simulated events. 37
5.2 Distribution of Δt_{err} for B^0 and $\overline{B}^0$ tag-separated in $B^0 \to K^0_{\mathrm{S}}\pi^0$ (upper) and $B^0 \to J/\psi K^0_{\mathrm{S}}$ (lower). 39
5.3 Number of PXD and SVD hits of both K^0_{S} daughters combined vs. Δt_{err} distribution for the $B^0 \to K^0_S\pi^0$ sample. 40
5.4 Number of PXD and SVD hits of both K^0_{S} daughters combined vs. Δt_{err} distribution for the $B^0 \to J/\psi K^0_S$ sample. 40
5.5 Distributions of Δt_{err} with different criteria on PXD hits. 41
5.6 Δt and Δt_{err} distributions in simulated signal events. 42
5.7 Correlation between Δt and Δt_{err} distributions in signal simulated sample. . . . 42
5.8 Fit projections of residual $\mathcal{R}(\Delta t_{\mathrm{rec}} - \Delta t_{\mathrm{MC}})$ distribution from simulated $B^0 \to K^0_{\mathrm{S}}\pi^0$ (left) and $B^0 \to J/\psi K^0_{\mathrm{S}}$ (right) events. 44
5.9 Normalized Δt_{err} distributions between signal and background events (left). Comparison between data and MC shown in right. 44

6.1 Comparison of normalized PDF shapes between TD and TI events. 47
6.2 2D scatter plots for different fit variables in signal simulation events. 48
6.3 2D scatter plots for different fit variables in $B\overline{B}$ simulation events. 49
6.4 2D scatter plots for different fit variables in $q\overline{q}$ simulation events. 49
6.5 Comparison of the normalized shape of ΔE in bins of Δt for signal (left) and continuum (right) components. 50
6.6 Comparison of the normalized shape of ΔE in bins of C'_{BDT} for signal (left) and continuum (right) components. 50
6.7 Comparison of the normalized shape of Δt in bins of C'_{BDT} for signal (left) and continuum (right) components. 51
6.8 Comparison of the normalised shape of M'_{bc} in bins of C'_{BDT} for signal (left) and continuum (right) components. 51

6.9 Example 4D fit projections for sixth $q \cdot r$ bin in signal simulation events. 53

6.10 Example fit projections of $B^0/\overline{B^0}$ tag separated for all $q \cdot r$ bins in signal simulation events. 54

6.11 4D fit projections for integrated $q \cdot r$ bin in $B\overline{B}$ simulation events. 55

6.12 4D fit projections for integrated $q \cdot r$ bin in continuum simulation events. 56

7.1 Various event yields and corresponding pull distributions. 59

7.2 C, S, and corresponding pull distributions. 60

7.3 Results of the linearity test for S, C, and signal yield. 61

7.4 Results of the likelihood profile for S, C, and signal yield. 62

8.1 3D fit projections for the $B^+ \to \overline{D}^0\pi^+$ simulation sample. 65

8.2 3D fit projections for the $B^+ \to \overline{D}^0\pi^+$ data sample. 66

9.1 Example 2D fit projections for the sixth $q \cdot r$ bin in signal simulation events. . . 68

9.2 2D fit projections for the integrated $q \cdot r$ bin in $B\overline{B}$ simulation events. 69

9.3 2D fit projections for the integrated $q \cdot r$ bin in continuum simulation events. . . 69

9.4 Lifetime fit projections in the 400 fb^{-1} simulation sample. 71

9.5 Lifetime fit projections in the 361.5 fb^{-1} data sample. 71

9.6 Fit projections of Δt (left) and M_{bc} (right) for CP fit in the 189.8 fb^{-1} data sample. 72

10.1 Signal enhanced CP fit projections of ΔE (upper-left), M'_{bc} (upper-right), C'_{out} (lower-left), and Δt (lower-right) shown for the 1 ab^{-1} simulated sample integrated in the seven $q \cdot r$ bins. 75

10.2 Signal enhanced B^0 lifetime fit projections of ΔE (upper-left), M'_{bc} (upper-right), C'_{out} (lower-left), and Δt (lower-right) shown for the data sample flavor integrated in 362 fb^{-1}. 78

10.3 Distributions of (a) M'_{bc}, (b) ΔE, (c) C'_{BDT}, and (d) Δt with fit projections overlaid for both B^0 and $\overline{B}^0$ candidates satisfying the criteria $5.27 < M'_{\mathrm{bc}} < 5.29\,\mathrm{GeV}$, $-0.15 < \Delta E < 0.10\,\mathrm{GeV}$, $|\Delta t| < 10.0\,\mathrm{ps}$, and $C'_{\mathrm{BDT}} > 0.0$ (except for the variable displayed). The solid curves represent the fit projection, while various fit components are explained in the legends. 80

10.4 Projection of the fit results onto Δt separately for tagged B^0 and $\bar{B}^0$ candidates after subtracting background with the ${}_s\mathcal{P}$lot method [78]; the asymmetry, defined as $[N(B^0_{\text{tag}}) - N(\bar{B}^0_{\text{tag}})]/[N(B^0_{\text{tag}}) + N(\bar{B}^0_{\text{tag}})]$, is displayed underneath, along with the projection of the fit result. 81

11.1 Simultaneous fit results on $B^+ \to \bar{D}^0\pi^+$ for events that pass the selection i.e., BDT> 0.6. 83

11.2 Simultaneous fit results on $B^+ \to \bar{D}^0\pi^+$ for events that fail the selection i.e., BDT < 0.6. 84

12.1 Results of the Δm fit to data (left) and MC (right) events. 91

12.2 Comparison of kaon and pion momentum between the *sPlot* and truth-matched signal events. 92

12.3 Comparison of kaon and pion momentum between data and simulation events with the latter scaled to the number of data events. 93

12.4 Schematic of the path of a charged track and the distance traversed in a silicon sensor. 94

12.5 $\mathrm{d}E/\mathrm{d}x$ distribution for pions in the momentum range 300–315 MeV fitted to a Landau convolved with a Gaussian function. 95

12.6 $\mathrm{d}E/\mathrm{d}x$ distributions for pions in the momentum range 300–315 MeV (left and right after removing one and two $\mathrm{d}E/\mathrm{d}x$ values, respectively) fitted to the sum of a Gaussian and an asymmetric Gaussian function. 95

12.7 Scatter plot of $\mathrm{d}E/\mathrm{d}x$ values of charged pions and kaons as a function of their momentum for data (left) and simulation (right) events. 96

12.8 $\mathrm{d}E/\mathrm{d}x$ mean of pions and kaons as a function of their momentum. 96

12.9 Binary kaon ID distribution in data (left) and simulation (right) events for SVD alone for a momentum less than 1 GeV 98

12.10 Binary kaon ID distributions in data (left) and simulation (right) events for a momentum less than 1 GeV 98

12.11 K efficiency and π fake rate vs momentum without (left) and with (right) SVD for binary ID $\mathcal{L}(K/\pi) > 0.5$. 99

12.12 Efficiency vs. fake rate with and without SVD for a momentum less than 1 GeV. 99

A.1 Comparison of BDT input variables between signal and background simulated $B^0 \to K_S^0\pi^0$ events. 104
A.2 Comparison of BDT input variables between signal and background simulated $B^0 \to K_S^0\pi^0$ events. 105
A.3 Comparison of BDT input variables between signal and background simulated $B^0 \to K_S^0\pi^0$ events. 106
A.4 Comparison of BDT input variables between signal and background simulated $B^0 \to K_S^0\pi^0$ events. 107

B.1 The distribution of fit variables shapes in $B\overline{B}$ background events. 109
B.2 The distribution of fit variables shapes in $q\overline{q}$ background events. 110
B.3 Distribution of Δt shape between signal and sideband region. 110

C.1 Efficiency vs. fake rate with and without SVD for a momentum ranging from 1.5 to 2.5 GeV. 112
C.2 $\mathrm{d}E/\mathrm{d}x$ distributions for pions after removing four (left) and two (right) $\mathrm{d}E/\mathrm{d}x$ values, fitted to the sum of a Gaussian and an asymmetric Gaussian function. . 113

List of Tables

1.1 Characteristics of quarks and leptons in the SM [4]. 3

1.2 Characteristics of bosons in the SM [4]. 3

2.1 List of quantities used in Eqs. (2.1- 2.2). 18

3.1 Summary of the final selections applied on final-state particles. 28

3.2 Linear coefficients between ΔE–M_{bc} and ΔE–M'_{bc}. 28

5.1 The definition of each r-bin interval and corresponding flavor tagging parameters for simulation. 37

5.2 The definition of each r-bin interval and corresponding flavor tagging parameters for data. 37

5.3 Resolution function parameters derived from $B^0 \to K^0_{\mathrm{S}}\pi^0$ signal simulated fit. . 45

6.1 Linear correlation coefficients among different fit variables. 48

7.1 Fitter details of the 7 $q \cdot r$ bin simultaneous fit. 58

7.2 Ensemble toy experiment results using 361.5 fb^{-1} simulation events. 58

8.1 Summary of selections applied on $B \to D\pi$ final-state particles. 64

8.2 PDFs used to model ΔE, M'_{bc} and C'_{out} for $B^+ \to \bar{D}^0\pi^+$. G, AG, CB, KDE, A, Poly1, and Poly3 denote Gaussian, asymmetric Gaussian, Crystal Ball, Kernel density estimation, ARGUS, first, and third-order polynomial, respectively. . . 64

8.3 Data-MC correction factors determined with the $B^+ \to \bar{D}^0\pi^+$ control mode. . . 64

9.1 Summary of selections applied on $B^0 \to J/\psi K^0_{\mathrm{S}}$ final-state particles. 68

9.2 Lifetime fit results in the 400 fb^{-1} simulation sample. 70

9.3 Lifetime fit results in the 361.5 fb^{-1} data sample. 70

9.4 *CP* fit results in the 189.8 fb^{-1} data sample. 72
9.5 Data-simulation correction factors of the Δt PDF. 73

10.1 Parameters determined from *CP* fit in the 1 ab^{-1} generic simulation sample. . . 74
10.2 Correlation among fit parameters. 76
10.3 Parameters determined from B^0 lifetime fit in 362 fb^{-1} Data sample. 77

11.1 Systematic uncertainties (relative) contributing to the branching fraction. 85
11.2 Systematic uncertainties (absolute) contributing to time-dependent *CP* asymmetries. 88

12.1 List of selection criteria used for the D^* selection. 91

A.1 Importance of BDT variables 103

Contents

1 Introduction **2**

1.1 *CP* violation in SM . . . 3

1.1.1 CKM matrix . . . 4

1.2 *CP* violation in neutral B meson . . . 7

1.3 Motivation to study the $B^0 \to K_S^0 \pi^0$ decay . . . 10

2 The Belle II experiment **13**

2.1 SuperKEKB accelerator . . . 13

2.2 Belle II detector . . . 14

2.2.1 Pixel Detector (PXD) . . . 15

2.2.2 Silicon-strip Vertex Detector (SVD) . . . 16

2.2.3 Central Drift Chamber (CDC) . . . 18

2.2.4 Time-Of-Propagation (TOP) counter . . . 19

2.2.5 Aerogel Ring-Imaging Cherenkov detector (ARICH) . . . 20

2.2.6 Electromagnetic Calorimeter (ECL) . . . 21

2.2.7 K_L^0 and μ detector (KLM) . . . 22

2.3 Trigger system . . . 23

3 Event reconstruction and selection **24**

3.1 Data and simulation sample . . . 24

3.2 K_S^0 selection . . . 24

3.3 π^0 selection . . . 25

3.4 Candidate B selection . . . 26

3.5 Modified $\boldsymbol{M_{\mathrm{bc}}}$ . . . 28

3.6 Best candidate selection . . . 30

3.7 Signal efficiency and self-crossfeed 30

4 Background studies **31**

4.1 Continuum suppression 31

4.2 $B\overline{B}$ background 33

5 Flavour tagging and decay-time selection **36**

5.1 Flavour tagging 36

5.2 Δt and Δt_{err} selection 38

5.3 Resolution function 43

6 Time-dependent *CP* asymmetry measurement **46**

6.1 Fit strategy 46

6.2 Correlation among the fit variables 48

6.3 Signal modeling 52

6.4 $B\overline{B}$ background modeling 55

6.5 Continuum background modeling 56

7 Fitter check **57**

7.1 Ensemble toy experiment 57

7.2 Linearity test 61

7.3 Liklihood profile 61

8 Study of $B^+ \to \overline{D}^0(\to K_S^0\pi^0)\pi^+$ control sample **63**

8.1 Introduction and fit strategy 63

8.2 Fit result and correction factors 63

9 Study of $B^0 \to J/\psi(\mu^+\mu^-)K_S^0$ control sample **67**

9.1 Introduction and fit strategy 67

9.2 B lifetime measurement 70

9.3 C and S determination 72

9.4 Correction factors 72

10 Fit results **74**

10.1 Fit to simulation 74

10.2 Fit to data . . . 77
10.2.1 B^0 lifetime fit . . . 77
10.2.2 CP asymmetry and $\mathcal{B}$ fit . . . 79

11 Systematic uncertainties and summary 82
11.1 Systematic uncertainties in $\mathcal{B}$ . . . 82
11.2 Systematic uncertainties in C and S . . . 86
11.3 Summary . . . 89

12 Low-momentum π/K identification with SVD 90
12.1 Data and simulation sample . . . 90
12.2 Analysis method . . . 90
12.3 SVD $\mathrm{d}E/\mathrm{d}x$ calibration . . . 94
12.3.1 Reconstruction of $\mathrm{d}E/\mathrm{d}x$ . . . 94
12.3.2 Likelihood-based PID method . . . 95
12.4 SVD PID performance . . . 97
12.4.1 Efficiency and fake rate . . . 97
12.5 Summary . . . 100

13 Conclusion 101

A Suplementary information related to BDT training 102

B Supplementary information related to fit 108
B.1 Fit variables distribution across $q \cdot r$ bin . . . 108
B.2 Δt distribution between signal and sideband region . . . 108
B.3 C and S results for TD and TI subsamples . . . 111

C Supplementary information related to SVD $\mathrm{d}E/\mathrm{d}x$ 112
C.1 ROC plot . . . 112
C.2 Truncation of $\mathrm{d}E/\mathrm{d}x$ distribution . . . 113

Chapter 1

Introduction

Experiments using high energy accelerators are designed to probe our current understanding of matter either by searching for new particles or measuring the properties of known particles to test the theory prediction to a high precision. The goal of scientific research is to understand the detailed structure and operation of Nature, followed by the subsequent application. The matter-antimatter asymmetry stands as one of the significant mysteries in particle physics. There is not enough charge-parity (*CP*) asymmetry in the standard model (SM) to explain the matter-antimatter asymmetry observed in the universe, so we expect additional sources of *CP* violation.

The SM describes the elementary constituents of the universe and how they interact among one other via strong, electromagnetic, and weak interactions. In the SM, particles come in two categories: fermions and bosons. Fermions, comprising quarks and leptons [1–3], constitute the building block of matter. These particles possess half-integer spin values, and their characteristics are listed in Table 1.1. Bosons, comprising photon, $W^{\pm}$, Z^0, and gluons, are force carrying particles responsible for mediating interactions among particles. The strong interaction is mediated by gluons that are responsible for tightly binding quarks inside hardons. The electromagnetic interaction is mediated by the photon that is responsible for interaction among charged particles. The weak interaction is mediated by $W^{\pm}$ and Z^0 that are responsible for processes like beta decay and neutrino interactions. Bosons have spin 1 and their characteristics are listed in Table 1.2. The discovery of the Higgs boson at the Large Hadron Collider completes the list of SM particles. It is a scalar particle with mass ≈ 125 GeV and is responsible for providing mass to the fundamental particles.

Table 1.1: Characteristics of quarks and leptons in the SM [4].

Type	Name	Mass (MeV)	Charge (e)
Quarks	up (u)	$2.2^{+0.5}_{-0.3}$	$+\frac{2}{3}$
	down (d)	$4.7^{+0.5}_{-0.2}$	$-\frac{1}{3}$
	charm (c)	1270 ± 20	$+\frac{2}{3}$
	strange (s)	$93.4^{+8.6}_{-3.4}$	$-\frac{1}{3}$
	top (t)	172690 ± 300	$+\frac{2}{3}$
	bottom (b)	4180^{+30}_{-20}	$-\frac{1}{3}$
Leptons	electron (e)	$0.51099895000 \pm 0.00000000015$	-1
	electron neutrino (ν_e)	$< 2 \times 10^{-6}$	0
	muon (μ)	$105.6583755 \pm 0.0000023$	-1
	muon neutrino (ν_μ)	< 0.19	0
	tau (τ)	1776.86 ± 0.12	-1
	tau neutrino (ν_τ)	< 18.2	0

Table 1.2: Characteristics of bosons in the SM [4].

Boson	Interaction	Mass (MeV)	Charge (e)
gluon (g)	strong	0	0
photon (γ)	electromagnetic	$< 10^{-21}$	0
$W^\pm$	weak	80377 ± 12	± 1
Z^0	weak	91187.6 ± 2.1	0

In this chapter, we provide a concise overview of the theory and physics motivation for the study of neutral B meson decays to the final state of K^0_S and π^0 mesons. The study of this decay mode is important to test the isospin sum rule [30], which is a crucial null test of [31] the SM. We introduce the source of *CP* violation in the SM and different types of *CP* violation in the B meson sector, and finally present the physics motivation of this study.

1.1 *CP* violation in SM

The predominance presence of matter in the universe remains one of the key mysteries of modern physics. During the Big Bang, one would expect an equal amount of matter and antimatter in a universe with perfect symmetry. When they encounter each other, they would then mutually annihilate, leaving behind only energy. Nevertheless, what we actually observe contradicts

this expectation.

According to Andrei Sakharov [7], the three conditions necessary for explaining the observed imbalance between matter and antimatter in the universe are:
1. at least one baryon number violating process,
2. charge conjugation (C) and charge conjugation-parity (CP) symmetry violation, and
3. interaction out of thermal equilibrium.

Discrete CP symmetry is a fundamental concept in particle physics that involves the properties of subatomic particles and their interactions. It involves a joint operation of charge conjugation and parity transformations. The C operation results in a change of the particle into its corresponding antimatter. On the other hand, the P operation inverts the spatial coordinate ($z \to -z$) of a system. When we combine the operations of C and P on a particle, we obtain the mirrored image of the corresponding antiparticle. Since both electromagnetic and strong interactions exhibit symmetry under C and P operations individually, they must also exhibit symmetry under the combined CP operation. In 1956, Yang and Lee proposed that weak interaction may not obey the parity symmetry [8]. In 1957, C.S. Wu conducted a groundbreaking experiment involving the β decays of Cobalt-60 [9] and provided evidence for the violation of parity symmetry in the weak interaction. Yang and Lee were awarded the Nobel Prize in Physics in 1957 for their work, and Wu's significant contributions were also acknowledged, although she did not share the Nobel Prize. It was commonly believed that CP symmetry was always conserved in weak interactions. In 1964, Christenson, Cronin, Fitch, and Turlay made a discovery by observing the decay of long-lived neutral kaons into two pions, thus confirming the evidence of CP violation in weak interactions [10]. The discovered CP violation in weak interactions is on the order of 10^{-3}. In recognition of their contributions, Cronin and Fitch received the Nobel Prize in Physics in 1980.

1.1.1 CKM matrix

In 1963, Nicola Cabibbo explained the suppression of certain subatomic processes where the strangeness quantum number is not conserved by proposing a mixing between d and s quarks with just a single free parameter, namely the Cabibbo quark-mixing angle (θ_C) [11]. The d-type quarks constitute a weak eigenstate, which is a combination of two mass eigenstates through a rotation described by the following form

$$d' = \cos\theta_C \, d + \sin\theta_C \, s. \tag{1.1}$$

Subsequently, Glashow, Iliopoulos, and Maiani expanded upon this concept to encompass four quarks by postulating the existence of an additional 'up'-type quark, known as the charm (c) quark [12]. The c quark was predicted to exhibit coupling with the weak eigenstate

$$s' = -\sin\theta_C\, d + \cos\theta_C\, s. \tag{1.2}$$

Hence, the suppression in the flavor changing neutral current (FCNC) process of $K_{\rm L}^0 \to \mu^+\mu^-$ was explained by the introduction of the (c) quark. In 1974, the observation of the $c\bar{c}$ bound state, known as the J/ψ, provided an experimental confirmation of the GIM mechanism [13].

In 1973, Kobayashi and Maskawa proposed the idea that the inclusion of a third family of quarks could potentially provide an explanation for *CP* violation within the SM framework [14]. Hence, the mixing between mass (d, s, b) and weak (d', s', b') eigenstates is characterized by a 3×3 quark-mixing matrix, referred to as the CKM matrix [22, 23]. The representation of this matrix is

$$\begin{pmatrix} d' \\ s' \\ b' \end{pmatrix} = V_{\rm CKM} \begin{pmatrix} d \\ s \\ b \end{pmatrix} = \begin{pmatrix} V_{ud} & V_{us} & V_{ub} \\ V_{cd} & V_{cs} & V_{cb} \\ V_{td} & V_{ts} & V_{tb} \end{pmatrix} \begin{pmatrix} d \\ s \\ b \end{pmatrix}, \tag{1.3}$$

where the matrix element V_{ij} represents the strength of the corresponding quark transition $i \to j$. The CKM matrix is unitary by construction, meaning that it satisfies the condition $V_{\rm CKM}^\dagger V_{\rm CKM} = I = V_{\rm CKM} V_{\rm CKM}^\dagger$. Typically, a 3×3 complex matrix can be expressed using nine real and nine imaginary components. Due to the unitarity conditions, it becomes possible to eliminate six parameters, resulting in the presence of only three mixing angles and six phases. Out of the six phases, it is feasible to absorb five of them by redefining the quark fields. Various parameterizations of the CKM matrix can be found in the literature. The entire CKM matrix can now be represented with four independent parameters, three angles ($\theta_{12}, \theta_{23}, \theta_{32}$) and a single phase ($\delta_{13}$), as [4]

$$V_{\rm CKM} = \begin{pmatrix} c_{12}c_{13} & s_{12}c_{13} & s_{13}e^{-i\delta_{13}} \\ -s_{12}c_{23} - c_{12}s_{23}s_{13}e^{-i\delta_{13}} & c_{12}c_{23} - s_{12}s_{23}s_{13}e^{-i\delta_{13}} & s_{23}c_{13} \\ s_{12}s_{23} - c_{12}c_{23}s_{13}e^{-i\delta_{13}} & -c_{12}s_{23} - s_{12}c_{23}s_{13}e^{-i\delta_{13}} & c_{23}c_{13} \end{pmatrix} \tag{1.4}$$

where $s_{ij} = \sin\theta_{ij}$ and $c_{ij} = \cos\theta_{ij}$. The phase can be introduced into any of the nine elements, and in this case, it has been retained in the element that describes the transition between the first and third quark families. Multiple experimental findings indicate that the diagonal elements are approximately equal to one, while the off-diagonal elements are close to zero. There appears

to be a hierarchical pattern in the strength of the charged current couplings. Inspired by this pattern, Wolfenstein parametrized [15] the CKM matrix in terms of an expansion parameter $\lambda \approx \sin\theta_{12}$, such that $\sin\theta_{23} = A\lambda^2$ and $\sin\theta_{13}e^{-i\delta_{13}} = A\lambda^3(\rho - i\eta)$, where A, ρ, and η are the real parameters of order unity. Then the CKM matrix becomes

$$V_{\mathrm{CKM}} = \begin{pmatrix} 1-\lambda^2/2 & \lambda & A\lambda^3(\rho - i\eta) \\ -\lambda & 1-\lambda^2/2 & A\lambda^2 \\ A\lambda^3(1-\rho-i\eta) & -A\lambda^2 & 1 \end{pmatrix} + O(\lambda^4). \tag{1.5}$$

This parameterization is extensively used in the field of flavor physics and suggests that $b \to c$ transitions are more likely than $b \to u$ transitions. A nonzero value of η would indicate the presence of a phase in V_{ub} and V_{td}, which serves as the origin of *CP* violation in the SM. The unitarity condition for the CKM matrix results in the following relationship:

$$\sum_j V_{ij}V^*_{jk} = 0. \ \ (i \neq k) \tag{1.6}$$

The six orthogonality conditions lead to the formation of the six unitarity triangles in the complex plane:

$$V_{ub}V^*_{us} + V_{cd}V^*_{cs} + V_{td}V^*_{ts} = 0, \tag{1.7}$$

$$V_{ud}V^*_{cd} + V_{us}V^*_{cs} + V_{ub}V^*_{cb} = 0, \tag{1.8}$$

$$V_{us}V^*_{ub} + V_{cs}V^*_{cb} + V_{ts}V^*_{tb} = 0, \tag{1.9}$$

$$V_{cd}V^*_{td} + V_{cs}V^*_{ts} + V_{cb}V^*_{tb} = 0, \tag{1.10}$$

$$V_{ud}V^*_{td} + V_{us}V^*_{ts} + V_{ub}V^*_{tb} = 0, \tag{1.11}$$

$$V_{ud}V^*_{ub} + V_{cd}V^*_{cb} + V_{td}V^*_{tb} = 0. \tag{1.12}$$

All six unitarity triangles possess equal area, representing the amount of *CP* violation within the SM [16]. Among them, only the triangle corresponding to Eq. 1.12 exhibits sides of similar length, and it is particularly relevant for the study of B-meson decays. The angles of "the" unitarity triangle are defined as follows:

$$\phi_1 = \arg\left(\frac{-V_{cd}V^*_{cb}}{V_{td}V^*_{tb}}\right) \tag{1.13}$$

$$\phi_2 = \arg\left(\frac{-V_{td}V^*_{tb}}{V_{ud}V^*_{ub}}\right) \tag{1.14}$$

$$\phi_3 = \arg\left(\frac{-V_{ud}V^*_{ub}}{V_{cd}V^*_{cb}}\right). \tag{1.15}$$

The angles ϕ_1, ϕ_2, and ϕ_3 are also known as β, α, and γ, respectively, in literature. Numerous measurements have been conducted to precisely determine these angles, since any deviation from the SM prediction would suggest the presence of physics beyond the SM. The current understanding of the CKM triangle is summarized in Fig. 1.1.

The Belle [17] and *BABAR* [18] collaborations performed an analysis to determine the *CP* violation parameters in the decay process of $B^0 \to J/\psi K^0_S$. This is the first observation of *CP* violation within *B*-meson decays, confirming the validity of the CKM mechanism for *CP* violation. The level of *CP* violation expected within the SM is insufficient to account for the difference between matter and antimatter observed in the universe [19–21]. An additional source of *CP* violation is thus required to explain this difference. In recent years, extensive measurements have been performed to precisely quantify the *CP* predictions of the SM and to look for the existence of any potential discrepancies.

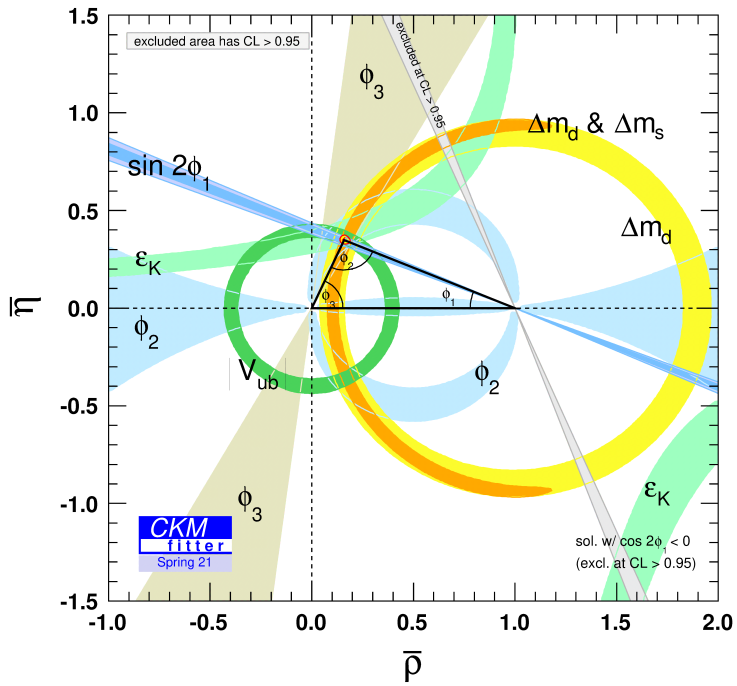

Figure 1.1: Experimental constraints of the CKM triangle in the $\bar{\rho} - \bar{\eta}$ plane [16].

1.2 *CP* violation in neutral *B* meson

A neutral B^0 meson is a bound state of a heavy bottom quark and a light down quark ($B^0 = \bar{b}d$, $\bar{B}^0 = b\bar{d}$). It is one of the most massive mesons ever observed, with a mass of 5279.66 ±

0.12 MeV and a relatively long lifetime of 1.519 ± 0.004 ps. One of the intriguing phenomena shown in Fig. 1.2, is related to neutral B^0 meson is the $B^0 - \overline{B^0}$ mixing, arising due to the difference between flavor and mass eigenstates. The mass eigenstates can be expressed as a

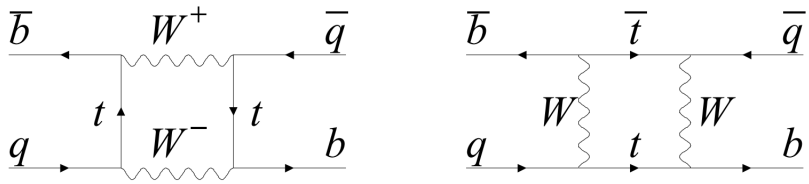

Figure 1.2: Dominant box diagrams for the $B_q^0 - \overline{B_q^0}$ transitions ($q = d$ or s).

linear combination of the flavor eigenstates,

$$|B_L\rangle = p|B^0\rangle + q|\overline{B^0}\rangle \tag{1.16}$$

$$|B_H\rangle = p|B^0\rangle - q|\overline{B^0}\rangle \tag{1.17}$$

Here, B^0 and $\overline{B^0}$ represent the flavor eigenstates, while B_L and B_H correspond to the lighter and heavier mass eigenstates, respectively, with p and q denoting the complex parameters. The time evolution of $|B_L\rangle$ and $|B_H\rangle$ is described as follows:

$$|B_L(t)\rangle = e^{-(im_L+\Gamma_L/2)t}|B_L(0)\rangle, \tag{1.18}$$

$$|B_H(t)\rangle = e^{-(im_H+\Gamma_H/2)t}|B_H(0)\rangle, \tag{1.19}$$

In these equations, m_L and m_H represent the masses of the eigenstates $|B_L\rangle$ and $|B_H\rangle$, respectively, while $\Gamma_L = 1/\tau_L$ and $\Gamma_H = 1/\tau_H$ stand for their respective decay widths. As the mass eigenstates B_H and B_L undergo separate evolutions without any mixing between them, it is easier to write the evolution of flavor eigenstates in terms of B^0 and $\overline{B^0}$. At $t = 0$,

$$|B^0(0)\rangle = \frac{1}{2p}(|B_L\rangle + |B_H\rangle) \tag{1.20}$$

At time t,

$$|B^0(t)\rangle = g_+(t)|B^0\rangle + \frac{q}{p}g_-(t)|\overline{B^0}\rangle, \tag{1.21}$$

$$|\overline{B^0}(t)\rangle = g_+(t)|\overline{B^0}\rangle + \frac{p}{q}g_-(t)|B^0\rangle, \tag{1.22}$$

where

$$g_{\pm}(t) = \frac{1}{2}[e^{-(im_L+\Gamma_L/2)t} \pm e^{-(im_H+\Gamma_H/2)t}] \tag{1.23}$$

Our goal is to study processes in which either B^0 or $\overline{B^0}$ decays into a final state f or its *CP*-conjugate state $\bar{f}$. Three kinds of *CP* violation can be manifested when both the B^0 and $\overline{B^0}$ mesons decay into the same final state (f) and exhibit some asymmetry in the decay process. The corresponding time-dependent *CP* asymmetry can be expressed as:

$$\begin{aligned} A(t) &= \frac{\Gamma[\overline{B^0}(t) \to f - \Gamma[B^0(t) \to f]]}{\Gamma[\overline{B^0}(t) \to f] + \Gamma[B^0(t) \to f]} && (1.24) \\ &= \frac{|\lambda_f|^2 - 1}{|\lambda_f|^2 + 1}\cos(\Delta m_d t) + \frac{2Im\lambda_f}{|\lambda_f|^2 + 1}\sin(\Delta m_d t) && (1.25) \\ &= -C\cos(\Delta m_d t) + S\sin(\Delta m_d t), && (1.26) \end{aligned}$$

where C and S are the direct and mixing-induced *CP* violation, respectively. The complex parameter λ_f is given by:

$$\lambda_f = \left(\frac{q}{p}\right)\left(\frac{\bar{\mathcal{A}}_f}{\mathcal{A}_f}\right), \tag{1.27}$$

where $\mathcal{A}_f$ and $\bar{\mathcal{A}}_f$ represent the amplitudes of $B^0 \to f$ and $\overline{B^0} \to f$ decays, respectively.

Three types of *CP* violation are defined as:

1) **Direct *CP* violation**

This type of *CP*-violation can appear when the decay rate of $B^0 \to f$ is different from that of $\overline{B^0} \to f$. This should satisfy the condition:

$$\frac{\mathcal{A}_f}{\overline{\mathcal{A}_{\bar{f}}}} \neq 1 \tag{1.28}$$

This form of *CP* violation can manifest in both neutral and charged B-mesons and arises due to interference between various amplitudes involving weak and strong phases.

2) ***CP* violation in mixing**

This type of *CP* violation can only occur in a neutral meson system and the corresponding condition is:

$$|\frac{q}{p}| \neq 1 \tag{1.29}$$

This kind of *CP* violation was first observed in the neutral kaon mixing and is detectable due to the significant difference in lifetimes between the $K^0_{\rm L}$ and $K^0_{\rm S}$ mass eigenstates. Conversely, this form of CP violation has a negligible effect in the neutral B^0 meson system.

3) ***CP* violation in interference between a decay with and without mixing**

This form of *CP* violation occurs when a neutral B^0 meson decays directly into a given final state or undergoes oscillation before decaying into the same final state (f). The condition for this *CP* violation is as follows:

$$Im(\lambda_f) \neq 0 \tag{1.30}$$

1.3 Motivation to study the $B^0 \to K_S^0\pi^0$ decay

The loop amplitude of $b \to s\bar{d}d$ is the dominant contributor to the decay $B^0 \to K^0\pi^0$. As shown in Fig. 1.3, this process involves the emission and reabsorption of a virtual W boson and a top quark, carrying a weak phase $\arg(V_{tb}V_{ts}^*)$. Among the three up-type quarks, namely up, charm, and top, the last one has the maximum contribution to the loop due to its large mass. The decay is significantly suppressed within the SM due to the relatively small value of $|V_{ts}|$. The study of this decay provides an opportunity to probe physics beyond the SM since non-SM particles could potentially propagate within the loop. The presence of such non-SM physics can be revealed through an asymmetry in the decay rates of *CP*-conjugate decays, which indicates the existence of *CP* violation [24].

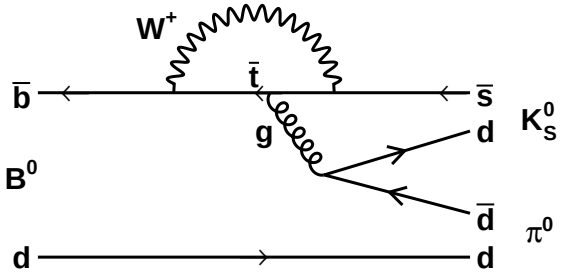

Figure 1.3: Feynman diagram of the dominant amplitude contributing to $B^0 \to K_S^0\pi^0$.

CP violation in the $B^0 \to K^0\pi^0$ channel can arise from two distinct phenomena: interference between two B^0 decay amplitudes, or interference between a B^0 decay amplitude and that of a $\bar{B}^0$ resulting from B^0–$\bar{B}^0$ mixing. These phenomena are quantified by the asymmetry parameters C and S, respectively. Assuming negligible contributions from subleading amplitudes with different weak phases and no *CP* violation in mixing, the expected values are $C = 0$ and $S = \sin 2\phi_1$, where ϕ_1 denotes $\arg\left(-V_{cd}V_{cb}^*/V_{td}V_{tb}^*\right)$. An additional weak phase is introduced by a color- and CKM-suppressed $b \to u\bar{u}s$ tree amplitude, which involves the emission of a W boson in the bottom-to-up-quark transition [25]. Consequently, this introduces a deviation from the expected S value of $\sin 2\phi_1$. Predictions of the resulting difference $\Delta S \equiv S - \sin 2\phi_1$, based

on QCD factorization, range between 0.01 and 0.12 [27, 32]. Similarly, the predicted value of C due to the color-suppressed tree amplitude ranges from −0.01 to 0.07 [27, 28]. One of the motivations for studying this decay is to determine the value of ΔS for the $b \to s$ loop transition. Note that the parameter $\sin 2\phi_1$ has been precisely measured to be 0.70 ± 0.02 in decays mediated by $b \to c\bar{c}s$ transitions, such as $B^0 \to J/\psi K_S^0$ [29].

Combining B-meson lifetimes (τ) with branching fractions ($\mathcal{B}$) and direct CP asymmetries of four $B \to K\pi$ decays related by isospin symmetry, the sum rule proposed in Ref. [30],

$$I_{K\pi} = \mathcal{A}_{CP}(K^+\pi^-) + \mathcal{A}_{CP}(K^0\pi^+)\frac{\mathcal{B}(K^0\pi^+)}{\mathcal{B}(K^+\pi^-)}\frac{\tau_{B^0}}{\tau_{B^+}} \tag{1.31}$$
$$-2\mathcal{A}_{CP}(K^+\pi^0)\frac{\mathcal{B}(K^+\pi^0)}{\mathcal{B}(K^+\pi^-)}\frac{\tau_{B^0}}{\tau_{B^+}} - 2\mathcal{A}_{CP}(K^0\pi^0)\frac{\mathcal{B}(K^0\pi^0)}{\mathcal{B}(K^+\pi^-)} = 0,$$

is expected to hold with an uncertainty below 1% and provides an important consistency test of the SM. The observed time-integrated $\mathcal{A}_{CP}$ value of $B^0 \to K^0\pi^0$ is diluted by an additional factor of $(1-2\chi_d)$ with respect to time-dependent asymmetry parameter C, where $\chi_d = 0.186 \pm 0.001$ [29] is the time-integrated $B^0 - \bar{B}^0$ mixing probability. In particular, $\mathcal{A}_{CP}$ is related to C through $\mathcal{A}_{CP} = (2\chi_d - 1) \cdot C$. Deviations from the isospin sum rule can be caused by either an enhancement of the color-suppressed tree amplitude or contributions from non-SM physics. The prediction of $\mathcal{A}_{CP}(K^0\pi^0)$ from this sum-rule is $+0.138 \pm 0.025$ [31], obtained using the latest known values of other quantities [29]. Combining measurements from *BABAR* and Belle [35,36], the Heavy Flavor Averaging Group finds $\mathcal{A}_{CP} = -0.01 \pm 0.10$ [29]. The dominant contribution to the uncertainty in this prediction comes from the uncertainty in $\mathcal{A}_{CP}(K^0\pi^0)$. Therefore, a precise measurement of $\mathcal{A}_{CP}(K^0\pi^0)$ is crucial for the consistency test of the SM.

The determination of the parameters C and S involves analyzing the differences in decay-time distributions between $B^0 \to K_S^0\pi^0$ and $\bar{B}^0 \to K_S^0\pi^0$ decays. Previous measurements of these parameters have been conducted by the *BABAR* and Belle experiments using 467×10^6 and 657×10^6 $B\bar{B}$ ($B = B^0$ or B^+) events, respectively [35, 36]. The corresponding measured C (S) values from these experiments are 0.13 ± 0.13 (0.55 ± 0.20) and −0.14 ± 0.14 (0.67 ± 0.32). Fig. 1.4 summarizes the experimental results on CP violation in the $B^0 \to K_S^0\pi^0$ decay. As the core part of my thesis, I have conducted the first measurement of C and S in the $B^0 \to K_S^0\pi^0$ decay from the Belle II experiment. Our analysis is based on a sample of $(387 \pm 6) \times 10^6$ $B\bar{B}$ events collected in e^+e^- collisions at a center-of-mass (c.m.) energy corresponding to the $\Upsilon(4S)$ resonance.

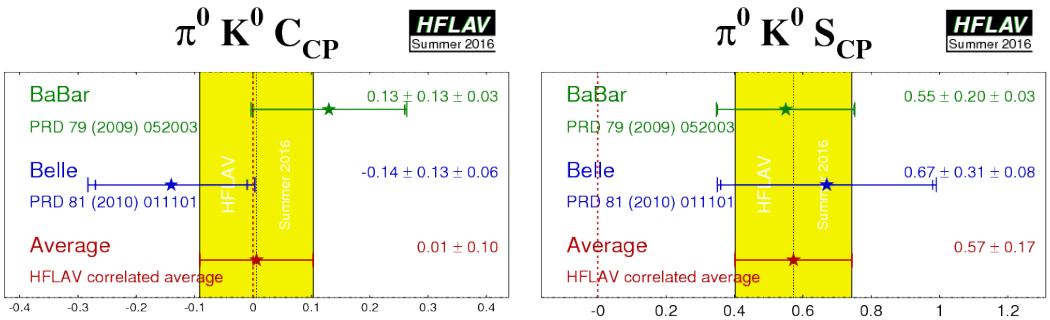

Figure 1.4: Summary of experimental results of *CP* violation in the $B^0 \to K_S^0\pi^0$ decay.

Chapter 2

The Belle II experiment

The Belle II experiment is operated by the international Belle II collaboration, which comprises 1170 physicists and engineers from 123 institutes spanning 27 countries, as of October 2023. The main goal of the experiment is to search for new physics in the flavor sector and to improve the precision of measurements of various SM parameters at the intensity frontier. Belle II is the successor to the Belle experiment and is operating at the SuperKEKB collider an asymmetric-energy e^+e^- collider located at the High Energy Accelerator Research Organisation (KEK) in Tsukuba, Japan. The Belle II detector is situated at the collision point of electrons and positrons within the accelerator complex. It has currently achieved a world-record luminosity of $4.7 \times 10^{34}\mathrm{cm}^{-2}\mathrm{s}^{-1}$ and collected a dataset of $362\,\mathrm{fb}^{-1}$ integrated luminosity at the $\Upsilon(4S)$ resonance. This chapter provides a brief description of the SuperKEKB accelerator and the Belle II detector.

2.1 SuperKEKB accelerator

SuperKEKB [37, 38] is an asymmetric electron-positron collider [39], as shown in Fig. 2.1. Asymmetric here means that the two counterrotating beams are accelerated to different energies: electrons to 7 GeV in the high energy ring (HER) and positrons to 4 GeV in the low energy ring (LER). Belle II has reduced the boost factor ($\beta\gamma$) from 0.43 to 0.29 when compared to its predecessor Belle experiment in order to mitigate intra-beam scattering. To compensate for the reduced boost, vertex detectors are installed just outside the interaction region. Due to the asymmetric beam energies, the $\Upsilon(4S)$ resonance and consequently, B^0 and $\overline{B^0}$ mesons are not created at rest, but rather in motion. This feature enables the separation of decay vertices of

produced B mesons, a crucial requirement for conducting time-dependent CP violation studies. The electron beam is produced within the linear accelerator (linac) using a short-pulse photon laser directed at a cold cathode. Positrons are generated by directing electrons toward a stationary tungsten target. The collider is called B factory as its aim is to copiously produce B and $\overline{B}$ meson pairs. The beam energies are chosen such that the $\Upsilon(4S)$ resonance is produced at an energy of 10.58 GeV, which mostly decays to a pair of B mesons. SuperKEKB is designed to have a 40 times higher luminosity than KEKB, with an instantaneous luminosity of $8 \times 10^{35}\text{cm}^{-2}\text{s}^{-1}$. The luminosity enhancement is achieved through the nano-beam approach [40], which is aimed to reduce the vertical beta function (β_y) at the interaction point (IP) by minimizing the effective longitudinal beam overlap. The two significant factors contributing to the increase in luminosity are roughly a doubling of beam currents and 20 times reduction in the β_y value at the IP.

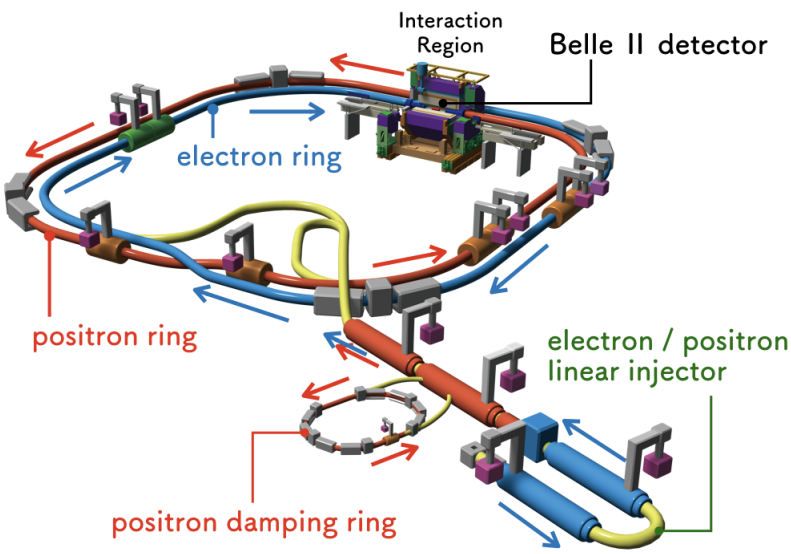

Figure 2.1: A schematic diagram of the SuperKEKB collider.

2.2 Belle II detector

Belle II, as described in Ref. [37], is a magnetic spectrometer that offers nearly full 4π solid-angle coverage. It consists of several subdetectors surrounding the interaction region in a cylindrical geometry around the beam pipe. Its primary purpose is to accurately reconstruct the final-state particles produced in e^+e^- collisions. The z-axis is collinear with the e^- beam direction and the polar angle θ is defined with respect to the z-axis. The detector is divided into

two sections depending on its θ coverage. The sections are the barrel ($32.2° < \theta < 128.7°$) and endcap ($12.4° < \theta < 31.4°$ or $130.7° < \theta < 155.1°$). Fig. 2.2 illustrates a general layout of the Belle II detector. Due to the improved detection systems of Belle II, it maintains similar performance levels to Belle even when exposed to higher beam background conditions. It has achieved such improved performance, largely due to a new pixel detector, a larger silicon-strip detector acceptance for K_S^0 reconstruction, and an improved PID system ensuring a better separation between charged pions and kaons. A detailed description of various subdetectors is provided in the following sections.

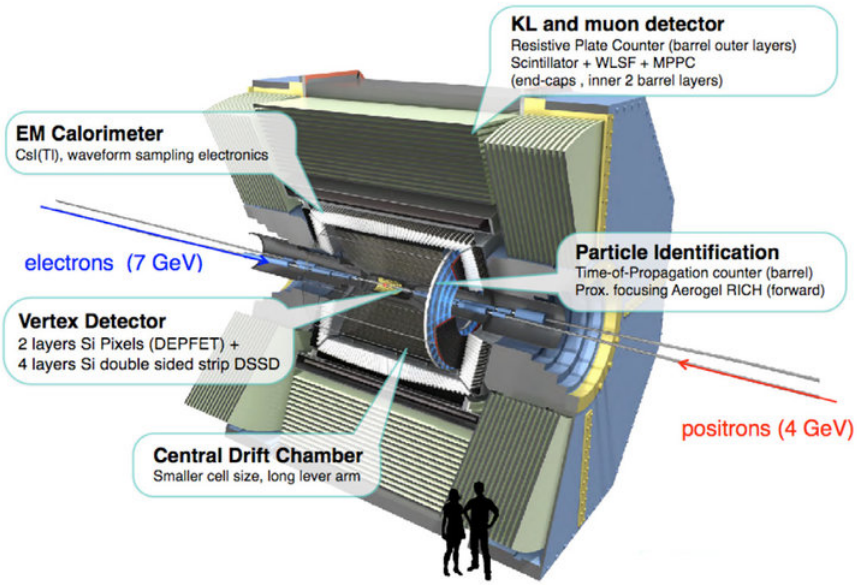

Figure 2.2: A schematic diagram of the Belle II detector.

2.2.1 Pixel Detector (PXD)

The SuperKEKB collider poses significant challenges due to high luminosities, resulting in subdetectors near the beam pipe experiencing exceptionally high hit rates from beam-related backgrounds like the Touschek effect and low-momentum-transfer quantum electrodynamics processes. These issues call for a careful consideration when designing the initial layers of the vertex detector. In the chosen nano-beam option, the 10-mm radius beam pipe in the interaction region presents both advantages and challenges. While it benefits the vertex reconstruction for physics purposes, it poses a challenge for the vertex detector due to the increased background proportional to the inverse square of the radius. To mitigate this, the innermost layers of the high-precision vertex detector employ pixel instead of strip sensors, which have a higher chan-

nel count and lower occupancy. The PXD uses the Depleted P-channel Field Effect Transistor (DEPFET) [41] technology, allowing thin sensors, while its readout electronics are located outside the acceptance region to minimize multiple scattering. Despite radiation hardness concerns, irradiation tests indicate that the DEPFET technology can effectively handle the radiation levels. The PXD comprises two layers, positioned at 14 and 22 mm from the IP, with excellent segmentation and resolution capabilities. The full PXD installation is performed during the 2022 shutdown, while the data used for our study were recorded with a partial second PXD layer covering one-sixth of the azimuth. The arrangement of the entire support structure, including the sensor ladders that have been installed, is shown in Fig. 2.3. The PXD's challenges, coupled with the chosen technology and its detailed design, still allow a precise B-meson decay vertex measurement in the demanding SuperKEKB environment.

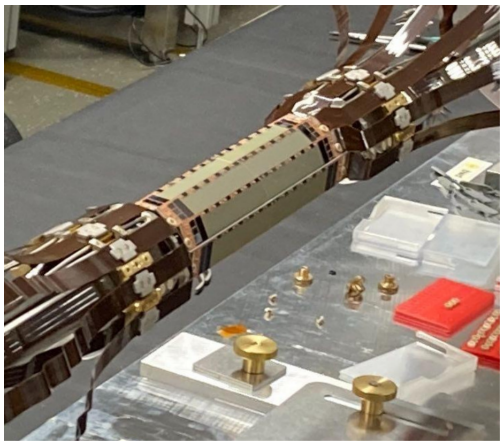

Figure 2.3: The configuration of the entire PXD support framework, including the installed sensor ladders and external services.

2.2.2 Silicon-strip Vertex Detector (SVD)

The SVD [42] consists of four layers of double-sided silicon strip sensors located at a radius of 38, 80, 115, and 140 mm from the IP, covering an angular acceptance from 17° to 150°. These layers are responsible for linking track information from the central drift chamber (CDC) to the PXD and tracking low-momentum charged particles with momenta as low as 50 MeV. The position resolution of the strips is approximately 20 μm, which is adequate for their placement at this radius. In the forward region, layers 4, 5, and 6 are tilted to reduce the material budget and sensor cost. The SVD comprises around 220,000 reading strips with a width of 320 μm, and to minimize the material budget, the read out circuits are placed directly on top of the sensors (the Origami scheme) to avoid exceeding 0.6% radiation length (X_0). APV25 chips are

used, each having 128 channels and a time resolution of approximately 3 ns. Fig. 2.4 shows the complete four-layer configuration of the Belle II SVD. The SVD plays a crucial role in

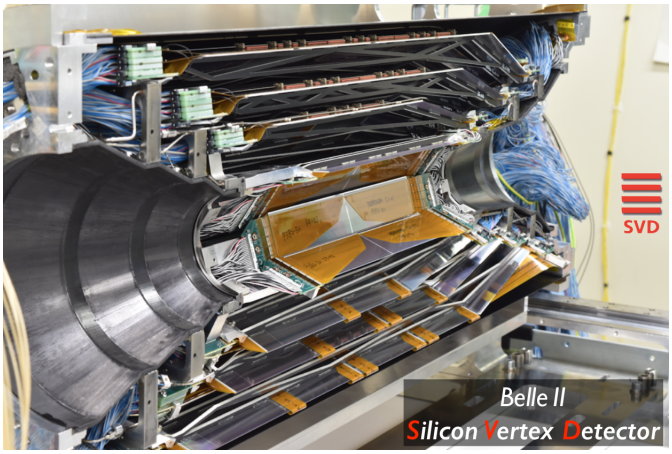

Figure 2.4: Belle II SVD with its complete set of four layers.

reconstructing charged particle tracks and decay vertices, particularly needed for *CP* violation measurements, where precise time measurements are essential. The longitudinal position resolution of the vertex detector is approximately 10 μm for high-momentum tracks, taking into account the particle's incoming angle and material thickness. The SVD's ability to handle low-momentum particles and its importance in enhancing the Belle II experiment's performance is evident from its design and capabilities.

Low-momentum particles are unable to reach the CDC, the main tracking subdetector of the experiment, owing to their highly curved trajectory. This means that the charged particle tracks can only be reconstructed with the vertex detector, which acts as an inner tracking system. We use specific ionization ($\mathrm{d}E/\mathrm{d}x$) by these low-momentum particles in the SVD to identify them. The Bethe-Bloch formula [43] describes the mean energy loss of a charged particle traversing through the detector as a function of its velocity:

$$\left\langle -\frac{dE}{dx} \right\rangle = Kz^2 \frac{Z}{A} \frac{1}{\beta^2} \left[\frac{1}{2} \ln \left(\frac{2m_e c^2 \beta^2 \gamma^2 T_{\max}}{I^2} \right) - \beta^2 - \frac{\delta(\beta\gamma)}{2} \right]. \tag{2.1}$$

For low momentum ($\beta \ll 1$), this relation reduces to

$$\left\langle -\frac{dE}{dx} \right\rangle \approx 4\pi n \frac{z^2}{m_e v^2} \left(\frac{e^2}{4\pi\epsilon_0} \right)^2 \ln \left(\frac{2m_e v^2}{I} \right). \tag{2.2}$$

by neglecting β^2 because of its small value and replacing βc by v. Various terms used in Eqs. (2.1- 2.2) are introduced in Table 2.1.

Table 2.1: List of quantities used in Eqs. (2.1- 2.2).

Symbol	Definition
Z	Atomic number of the detector material
A	Atomic mass of the detector material
K	$\frac{4\pi N_A r_e^2 m_e c^2}{A} = 0.307075\,\mathrm{MeV/cm}$
N_A	Avogadro's number
r_e	Classical electron radius
z	Charge of the incident particle
m_e	Electron's mass
I	Mean excitation energy
$\delta(\beta\gamma)$	Density effect correction
$T_{\max}$	Maximum kinetic energy per collision
n	Electron density of the detector material
ϵ_0	Permittivity of vacuum

The minimum energy loss in silicon detectors occurs near $\beta\gamma \approx 3$ regardless of the particle type. A particle that loses minimum energy producing the smallest possible signal in the SVD is called a minimum ionizing particle (MIP) and provides an important benchmark for testing the subdetector. As evident from Eqs. (2.1- 2.2), the formula for energy loss via ionization only depends on the particle velocity through $\beta\gamma$. Thus, if we plot the energy loss for different types of particles over their momentum $p = \beta\gamma mc$, the same $\beta\gamma$ curve can be used to describe them only scaled by their mass m. For different particles, the behavior of the curve will be different. This difference forms the basis of the $\mathrm{d}E/\mathrm{d}x$ PID method, which has been exploited in the case of SVD to distinguish various charged particles. Details can be found in Chapter 12.

2.2.3 Central Drift Chamber (CDC)

The CDC of the Belle II detector performs multiple functions. Firstly, it is the key responsible for reconstructing charged particle tracks with high precision and accurately measuring their momenta. Secondly, the CDC contributes to PID based on $\mathrm{d}E/\mathrm{d}x$ measurements within its gas volume. Finally, the CDC plays a pivotal role in providing efficient and reliable trigger signals for events involving charged particles. The CDC's design at Belle II closely follows that of its predecessor, Belle, as the Belle CDC had operated reliably for over a decade without any significant issues. It consists of 56 layers containing 14,336 sense wires immersed in

a helium-ethane gas mixture. These layers are organized into superlayers, with alternating axial and stereo wire configurations (shown in Fig. 2.5), allowing for a three-dimensional track reconstruction. The CDC's outer radius has been expanded to 1130 mm to accommodate the SVD and to avoid high-radiation areas near the IP, while the inner radius is set at 160 mm. This design change, along with improvements in readout electronics to handle higher trigger rates, enhances the CDC's performance at Belle II. Furthermore, the CDC is crucial for PID through $\mathrm{d}E/\mathrm{d}x$ measurements, where different particles exhibit distinct energy loss characteristics. This information becomes particularly essential for low-momentum tracks that may not reach other PID devices. In summary, the CDC at Belle II is not only a primary tracking device but also a key component for PID and trigger generation, ensuring the success of the experiment in studying charged particles.

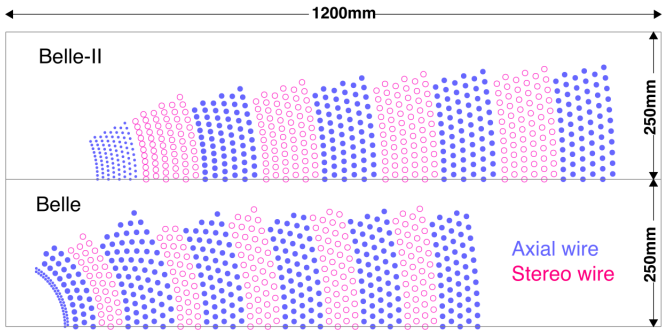

Figure 2.5: Comparison between wire configurations of the (top) Belle II and (bottom) Belle CDC [44].

2.2.4 Time-Of-Propagation (TOP) counter

To improve our ability to distinguish between charged kaons and pions as well as to adapt to a higher background environment, the PID system in the barrel region of Belle II has undergone a significant upgrade. The Belle time-of-flight and aerogel Cherenkov counters are replaced by a Time-Of-Propagation (TOP) counter [45]. The TOP counter consists of 16 modules surrounding the CDC, each comprising a 2.5 m long quartz bar, a prism, a focusing mirror, and Multi-Channel Plate Photomultipliers (MCP-PMTs). This innovative system measures the time of propagation of Cherenkov photons (shown in Fig. 2.6) internally reflected within the quartz bar, providing precise (x, y) coordinates and timing information. This information allows the reconstruction of the Cherenkov angle (θ_C), when combined with the particle's momentum and impact point on the quartz bar, and enables the calculation of likelihood values for dif-

ferent mass hypotheses. A focusing system [46] is introduced to mitigate the chromaticity of Cherenkov photons and optimize the PID performance. The TOP's primary goal is to improve kaon and pion separation, but it also contributes to the identification of other charged particles, resulting in a well-rounded PID scheme for Belle II.

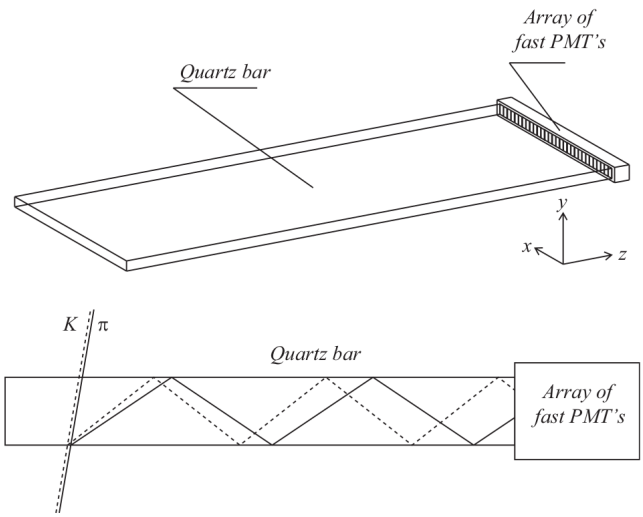

Figure 2.6: A schematic view of the TOP counter module (top) and of its principle of operation (bottom) [47].

2.2.5 Aerogel Ring-Imaging Cherenkov detector (ARICH)

In the forward endcap region of Belle II, the primary objective is to achieve an effective identification of charged particles spanning their entire kinematic range. The Aerogel Ring-Imaging Cherenkov (ARICH) subdetector has been strategically designed to meet this challenge, aiming to distinguish between kaons and pions across a significant portion of their momentum spectrum and to provide additional discrimination capabilities for pions, muons, and electrons below 1 GeV. The ARICH system incorporates several components to fulfill its mission. It begins with an aerogel radiator that serves as the active material where Cherenkov photons are generated by the traversing charged particle. An expansion volume follows, allowing these Cherenkov photons to form distinguishable rings on the photodetector surface. The array of position-sensitive photodetectors plays a crucial role by efficiently detecting single Cherenkov photons even in the presence of a high magnetic field, ensuring high-resolution measurements in two dimensions. Furthermore, a well-designed readout system supports the photodetector in providing essential data for PID. The ARICH's structural choices and criteria align with the goal of optimizing performance. To ensure the detection of a sufficient number of photons

for PID (typically around 10 per ring image), the length of the aerogel radiator is designed to span several centimeters. At the same time, the desired Cherenkov angle resolution requires an expansion gap of approximately 20 cm and a radiator thickness that remains within a few centimeters [48], with the photodetector granularity at a few millimeters. Two main challenges have been successfully addressed during the ARICH's development: increasing the number of detected Cherenkov photons and developing a photodetector capable of functioning reliably within the high magnetic field environment of Belle II. To enhance the Cherenkov angle resolution, a unique solution has been implemented, involving a non-homogeneous radiator [49] with multiple layers of aerogel with different refractive indices. This innovative approach enables the overlapping of Cherenkov rings on the photon detector, significantly reducing the effects of emission point uncertainty. Fig. 2.7 shows a schematic view of the ARICH subdetector. Moreover, the ARICH relies on a hybrid avalanche photodetector (HAPD) of the proximity-focusing type as its baseline choice, further ensuring efficient single photon detection. This combination of engineering solutions and careful design choices makes the ARICH subdetector an essential component of Belle II's PID system in the forward endcap region, significantly enhancing its PID capabilities and contributing to the overall success of the endeavor.

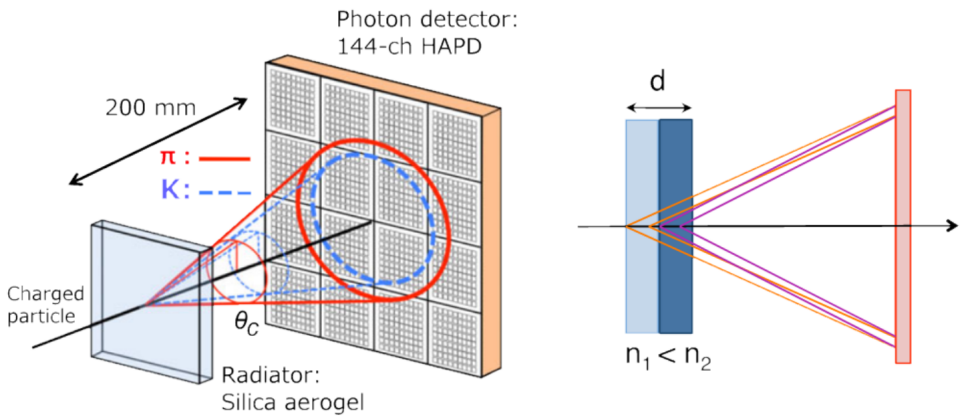

Figure 2.7: The principle of PID operation (left) of the proximity focusing with non-homogeneous aerogel radiator (right) of the ARICH subdectector [50].

2.2.6 Electromagnetic Calorimeter (ECL)

The ECL plays a pivotal role at Belle II in achieving high-resolution measurements of photon energies spanning a range from 20 MeV to 4 GeV. This capability is crucial as a significant portion of B-meson decay products consists of neutral pions (π^0), which decay into two photons. The ECL is constructed using CsI(Tl) crystals chosen for their exceptional attributes,

including high light output, relatively short radiation length, robust mechanical properties, and cost effectiveness. Its multifaceted role encompasses photon detection with high efficiency, precise determination of photon energy and angular coordinates, electron identification, trigger signal generation, and both online and offline luminosity measurements. The ECL system comprises a 3 m long barrel section with an inner radius of 1.25 m and annular endcaps positioned at $z = 1.96$ m (forward) and $z = -1.02$ m (backward) relative to the IP, covering the polar angle range of $12.4° < \theta < 155.1°$ with small gaps between the barrel and endcaps. The barrel portion consists of a tower structure housing 6624 CsI(Tl) crystals, each shaped as a truncated pyramid measuring approximately 6×6 cm^2 in cross-section and 30 cm in length ($\approx 16.1\ X_0$). The endcaps incorporate 2112 CsI(Tl) crystals of varying shapes, bringing the total crystal count to 8736, with a cumulative mass of approximately 43 tons. Each crystal is equipped with photodiodes, preamplifiers, and external shaper boards for scintillation light readout. This configuration, coupled with advanced electronics, significantly enhances the ECL's performance, offering energy resolutions of 4% at 100 MeV and 1.6% at 8 GeV, as well as angular resolutions of 13 and 3 mrad at low and high energies, respectively, with a remarkable π^0 mass resolution of 4.5 MeV. Furthermore, to address the challenge posed by high backgrounds and maintain efficiency, Belle II's ECL has seen substantial upgrades in its electronics, incorporating waveform-sampling readout electronics and deploying machine learning techniques such as Boosted Decision Trees (BDT) for PID, leading to a notable reduction in fake rates and an overall improvement in identification efficiency.

2.2.7 K_L^0 and μ detector (KLM)

The K_L^0 and muon detector (KLM), situated outside the superconducting solenoid of Belle II, features an alternating structure of 4.7 cm thick iron plates and active detectors. These iron plates act as both the magnetic flux return for the solenoid and material for K_L^0 mesons to shower hadronically, providing 3.9 interaction lengths in addition to the 0.8 interaction lengths of the calorimeter. The KLM comprises an octagonal barrel covering a polar angle range from 45° to 125°, with endcaps extending the coverage from 20° to 155°. It consists of 15 detector layers in the barrel and 14 in each endcap. Muons and non-showering charged hadrons with a momentum above approximately 0.6 GeV traverse the KLM in a nearly straight-line path. K_L^0 mesons that interact in the calorimeter or iron plates create hadronic showers detectable in the ECL, KLM, or both. The Belle KLM used glass-electrode resistive plate chambers (RPCs) [51], which demonstrated good performance but suffered from long dead times during electric field

recovery after a discharge. At SuperKEKB, higher background rates are expected, leading to the RPC efficiency degradation, particularly in the endcaps, where the shielding against external neutron and particle sources is limited. Consequently, at Belle II, the endcap RPCs are replaced with scintillators for improved performance.

2.3 Trigger system

The Belle II trigger system is an essential component designed to efficiently manage and select relevant physics events from the high background conditions expected at the accelerator, particularly in the face of increasing luminosity and varying beam parameters. To meet these challenges, the trigger system comprises both Level 1 (L1) hardware-based and High-Level Trigger (HLT) software-based components. The L1 trigger incorporates multiple subtrigger systems from various subdetectors, each gathering specific trigger information and sending it to the Global Decision Logic (GDL), which makes the final decision. The sub trigger systems include the CDC for charged track information, ECL for energy deposit and cluster data, barrel and endcap PID for precise timing and hit topology, and KLM for muon track information. The trigger scheme used at Belle II is based on a successful Belle triggering scheme [52], though it incorporates new technologies, replacing old components with Field Programmable Gate Arrays (FPGAs) for a configurable trigger logic. The system aims to maintain a maximum average trigger rate of 30 kHz, with a fixed latency of about $5\mu s$ and a timing precision of less than 10 ns. It employs multiple independent subtriggers to reduce the L1 trigger rate effectively. Beyond the L1 trigger, the HLT further refines event selection based on fully reconstructed objects, with a goal of reducing event rates to the maximum design output rate value of 10 kHz while ensuring high efficiency. The Belle II trigger system is thus designed to adapt to changing background conditions and to achieve the necessary event selection for physics studies, with ongoing development to handle rising event rates as well as to optimize data acquisition and storage.

Chapter 3

Event reconstruction and selection

3.1 Data and simulation sample

We use the simulation samples for event selection, background studies, and to prepare the fit models. We use signal-only simulated events to determine the signal model and estimate the selection efficiency. The so-called generic sample consists of simulated events that include $e^+e^- \to q\bar{q}$ ($q = u, d, s, c$), $B^0\bar{B}^0$ and B^+B^- processes in realistic proportions, corresponding to about three times that of the $\Upsilon(4S)$ data. We use EvtGen [53] to generate $\Upsilon(4S) \to B\bar{B}$ with the subsequent B-meson decays and Photos [54] to incorporate final-state radiation from charged particles. The simulation of $q\bar{q}$ background relies on the Kkmc generator [55] interfaced to Pythia [56]. The detector response for final-state particles is simulated with Geant4 [57]. Both collision and simulated data samples are reconstructed using the Belle II software [58, 59].

3.2 K_S^0 selection

The K_S^0 candidates are selected from a merged K_S^0 list, of secondary vertex [60] objects, and the candidates reconstructed from $\pi^+\pi^-$. We suppress the contamination from prompt K_S^0 and Λ decays using two BDT classifiers [61]. These BDTs rely mostly on kinematic information from the K_S^0 and its decay products, along with the PID information of the latter. We require the dipion invariant mass to lie between 489 and 507 MeV, which is 3σ window around the mean of the K_S^0 mass distribution. The reconstructed K_S^0 mass distribution in the signal MC sample is shown in Fig. 3.1.

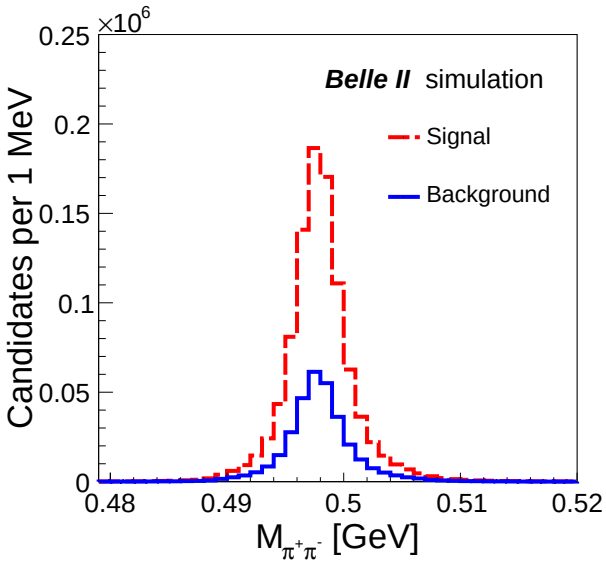

Figure 3.1: Reconstructed K_S^0 mass distribution for signal and background events.

3.3 π^0 selection

We use a π^0 list containing the $\pi^0 \to \gamma\gamma$ decay candidates that undergo a mass-constraint fit. The π^0 candidates are retained if their final-state photons detected in the barrel and endcap ECL have an energy greater than 35 and 153 MeV, respectively. Figure 3.2 shows the reconstructed energy distribution of photons obtained from the simulation sample. We require the diphoton mass to lie between 116 and 150 MeV which is ($\pm 3\sigma$) window around the mean of the π^0 mass distribution. The absolute cosine of the angle between the higher-energy photon's direction in the π^0 rest frame and the π^0 direction in the lab frame, $|\cos\theta_{\rm hel}|$, must also be less than 0.972. These criteria suppress contributions from misreconstructed π^0 candidates. Figure 3.3 shows the reconstructed π^0 mass and $|\cos\theta_{\rm hel}|$ distributions obtained from the simulation sample. The optimized criteria mentioned above are determine through a comprehensive grid scan, where we select a list of variables and corresponding selection points for each of them. Subsequently, we evaluate the performance of each individual configuration and select the optimized criterion by maximizing the figure-of-merit ($\frac{S}{\sqrt{S+B}}$), where $S(B)$ represents the number of signal (background) events in a 1ab^{-1} generic sample. For the selection of signal and background, we choose the truth-matched signal events and the remaining events in the generic sample, respectively.

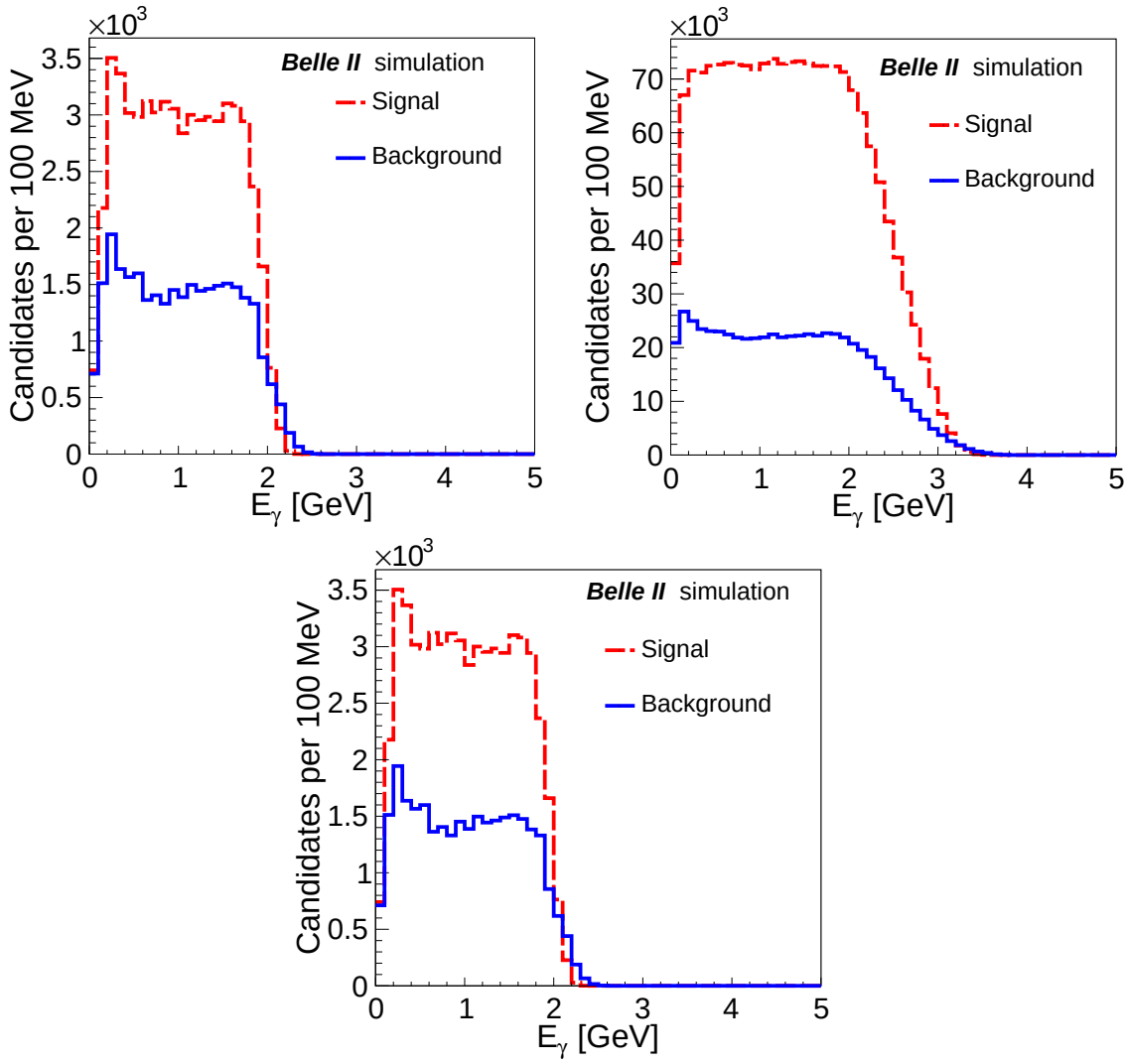

Figure 3.2: Reconstructed photon energy distributions for backward-endcap (upper-left), barrel (upper-right), and forward-endcap (lower) ECL region.

3.4 Candidate B selection

The B-meson candidate is reconstructed by combining a K_S^0 with a π^0 candidate. For this purpose, we use two kinematic variables: the beam-energy-constrained mass ($M_{\rm bc}$) and the energy difference (ΔE), defined as

$$\begin{aligned} M_{\rm bc} &= \sqrt{E_{\rm beam}^2 - |\vec{p}_B|^2}, \\ \Delta E &= E_B - E_{\rm beam}, \end{aligned} \tag{3.1}$$

where $E_{\rm beam}$ is the beam energy, E_B and $\vec{p}_B$ are respectively the reconstructed energy and momentum of the B meson; all calculated in the c.m. frame. The treeFitter algorithm [63, 64] is used to fit the signal-side B_{CP} decay vertex. For the reconstruction of B_{CP}, an IP constraint is

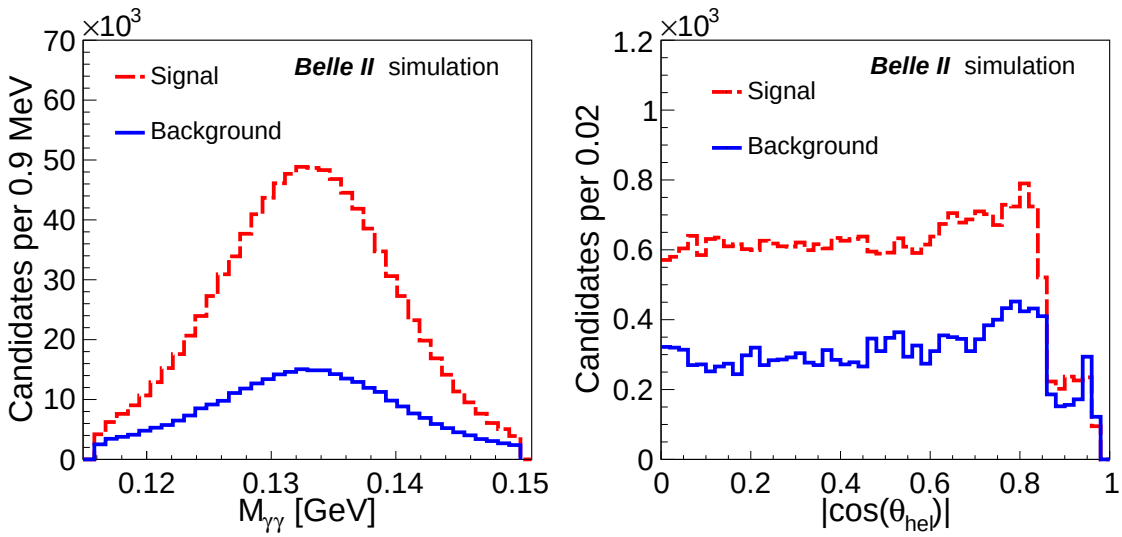

Figure 3.3: Reconstructed π^0 mass (left) and $|\cos\theta_{\rm hel}|$ (right) distributions.

applied, which ensures that the flight direction of each K_S^0 candidate aligns with its vertex displacement direction relative to the IP. The tag-side $B_{\rm tag}$ vertex is reconstructed with tracks that are not associated with the $B^0 \to K_S^0\pi^0$ candidate. The RAVE algorithm [65] is used to fit the tag-side $B_{\rm tag}$ decay vertex. It is used for the tag-side because it allows the weighting of contributions from tracks that are displaced from the $B_{\rm tag}$ decay vertex, effectively reducing potential biases from secondary charm decays. The $M_{\rm bc}$ and ΔE distributions in the signal simulation sample are shown in Fig. 3.4. The final optimized selections are listed in Table 3.1.

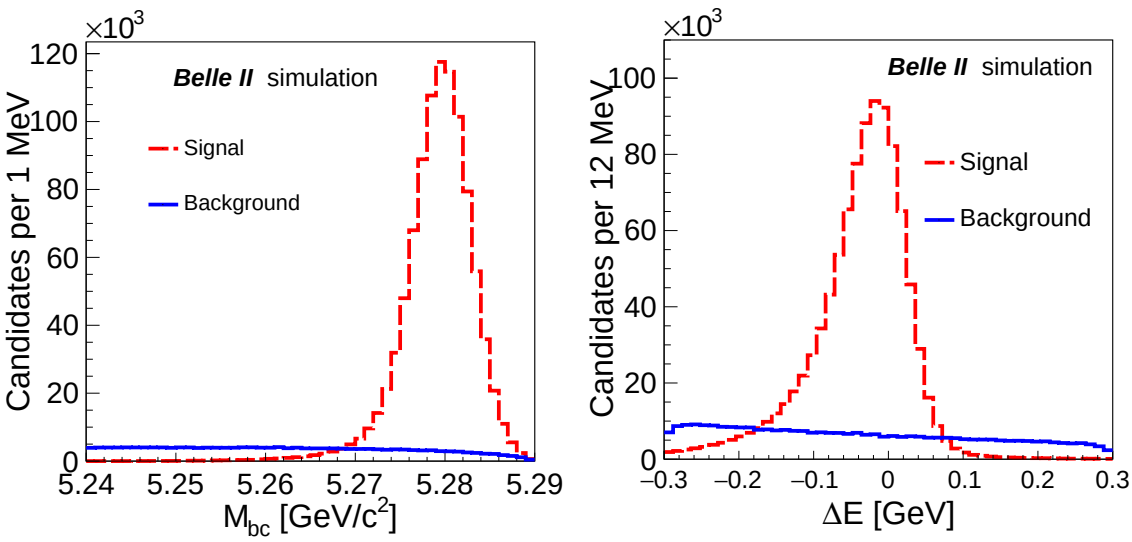

Figure 3.4: $M_{\rm bc}$ and ΔE distributions of signal B candidates.

Table 3.1: Summary of the final selections applied on final-state particles.

K^0_{S} selection	$489 < M_{\pi^+\pi^-} < 507\,\mathrm{MeV}$
π^0 selection	$116 < M_{\gamma\gamma} < 150\,\mathrm{MeV}$
	$\lvert\cos\theta_{\mathrm{hel}}\rvert < 0.972$
	E_γ (endcap) $> 153\,\mathrm{MeV}$
	E_γ (barrel) $> 35\,\mathrm{MeV}$

3.5 Modified M_{bc}

The presence of a π^0 meson in the final state causes a nontrivial correlation between ΔE and M_{bc} due to the energy leakage of its final-state photons. We introduce a modified M_{bc} to minimize this correlation by replacing the π^0 energy $E^*_{\pi^0}$ with $E^*_B - E^*_{K^0_{\mathrm{S}}}$:

$$M'_{\mathrm{bc}} = \sqrt{E^{*2}_{\mathrm{beam}} - \left(\vec{p}^{\,*}_{K^0_{\mathrm{S}}} + \frac{\vec{p}^{\,*}_{\pi^0}}{|\vec{p}^{\,*}_{\pi^0}|}\sqrt{(E^*_{\mathrm{beam}} - E^*_{K^0_{\mathrm{S}}})^2 - m^2_{\pi^0}}\right)^2}, \tag{3.2}$$

where the superscript $*$ denotes that the kinematic quantities are calculated in the c.m. frame. The 2D scatter plots between ΔE–M_{bc} and ΔE–M'_{bc} for all components are shown in Fig. 3.5. As listed in Table 3.2, we find that the linear correlation coefficients have been reduced for all event categories with the introduction of M'_{bc}.

Table 3.2: Linear coefficients between ΔE–M_{bc} and ΔE–M'_{bc}.

Category	ΔE–M_{bc}	ΔE–M'_{bc}
Signal	+18.9%	−0.7%
$B\overline{B}$	−6.4%	+4.4%
$q\overline{q}$	−0.4%	+0.4%

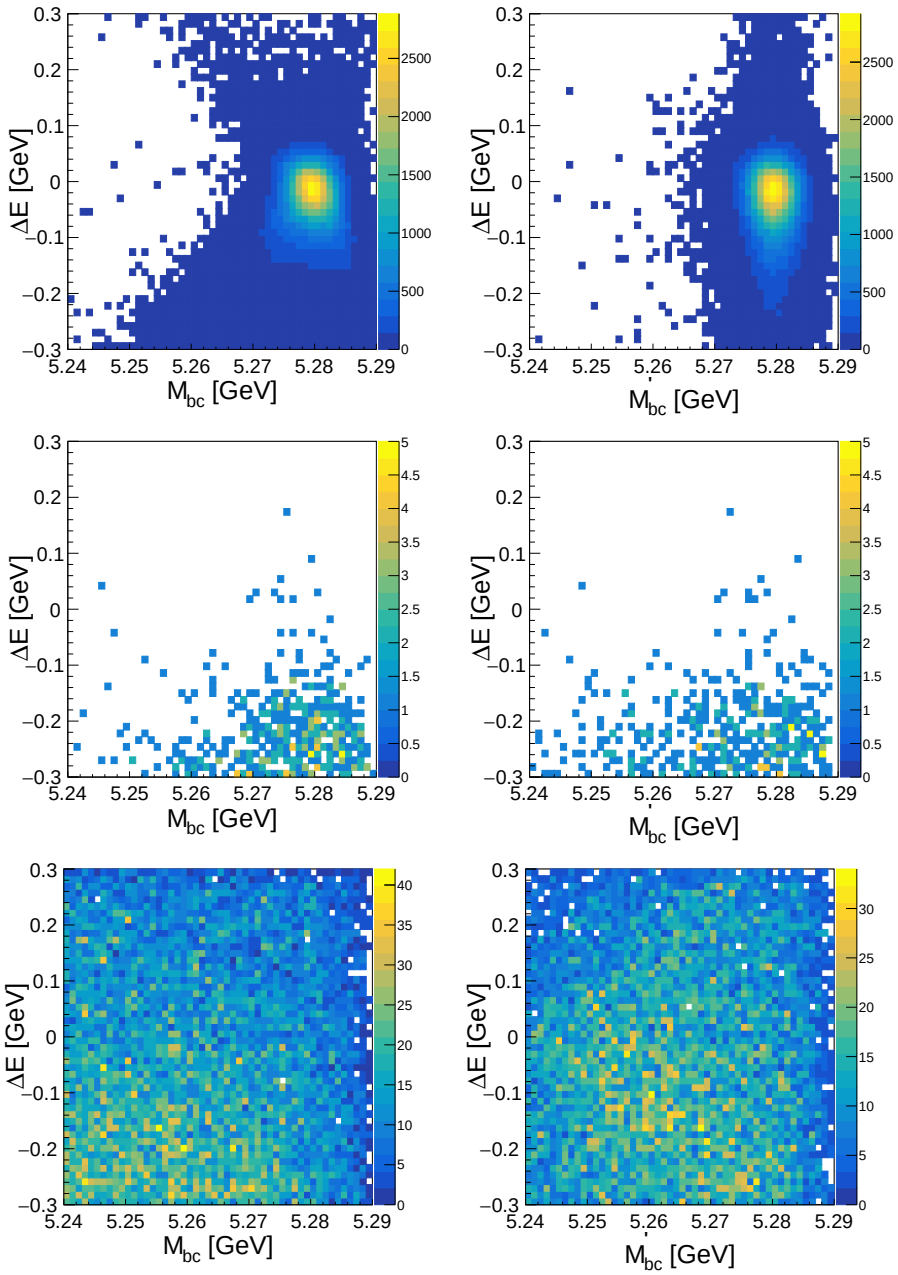

Figure 3.5: 2D scatter plots ΔE–M_{bc} (left) and ΔE–M'_{bc} (right) for signal (upper), $B\overline{B}$ (middle) and $q\overline{q}$ (lower) events.

3.6 Best candidate selection

After applying all selection criteria, 3% of the events are found to have more than one B candidate. Such multiple candidates come from random combinations of final-state particles. Figure 3.6 shows the distribution of B-candidate multiplicity in the signal simulated sample. In events with multiple candidates, we choose the one with the largest p-value resulting from the π^0-mass-constrained fit; if that criterion is ambiguous, we select the candidate with the largest p-value from the K_S^0-vertex fit. The best candidate selection (BCS) efficiency, defined as

$$\epsilon_{\mathrm{BCS}} = \frac{\text{No. of signal events with multiplicity} > 1 \text{ after BCS}}{\text{No. of total signal events with multiplicity} > 1} \tag{3.3}$$

is found to be 87% in the signal simulation sample.

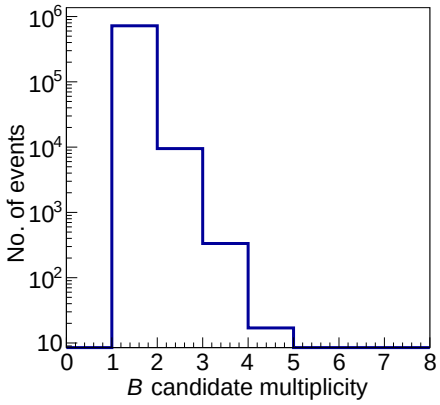

Figure 3.6: B-candidate multiplicity distribution in the signal simulated sample.

3.7 Signal efficiency and self-crossfeed

Following the application of BCS, we find a small number of misreconstructed events alongside correctly reconstructed events in our sample. The former events arise when the best B candidate is mistakenly reconstructed from the final-state particles of other B meson decays, and they are referred to as misreconstructed or self-crossfeed signal events. To identify such misreconstructed candidates, we utilize the generator-level information. We find:

$$\text{Efficiency of correctly reconstructed signal events} = \frac{N_{\mathrm{S}}}{N_{\mathrm{G}}} = 20.8\% \tag{3.4}$$

$$\text{Fraction of self-crossfeed signal events} = \frac{N_{\mathrm{SCF}}}{N_{\mathrm{S}} + N_{\mathrm{SCF}}} = 1.7\%, \tag{3.5}$$

where N_{S} (N_{SCF}) is the number of correctly reconstructed (self-crossfeed) candidates and N_{G} is the number of generated signal events. As SCF events represent a small fraction of the total signal events, we consider them as a part of signal as their PDF shapes are similar to signal.

Chapter 4

Background studies

4.1 Continuum suppression

The most dominant source of background is $e^+e^- \to q\overline{q}$ ($q = u, d, s, c$) continuum process. Continuum events result in final-state particles collimated into two back-to-back jets, whereas those from $e^+e^- \to \Upsilon(4S) \to B\overline{B}$ are almost uniformly distributed over the 4π solid angle. We exploit this difference in event topology to suppress the continuum background. We use continuum, $B^0\overline{B}^0$ and B^+B^- MC events, each equivalent to an integrated luminosity of $1\,\mathrm{ab}^{-1}$, to study various backgrounds. A BDT [62] classifier is used to combine the following event-shape variables.

• KSFW moments: Kakuno-San's modified Fox–Wolfram [66] (KSFW) moments H^{oo}_{xl} and H^{oo}_{l}. All reconstructed particles in an event are divided into two categories: B candidate final-state (denoted as s) and the ROE (denoted as o); H^{oo}_{xl} is decomposed into three categories: a charged particle part (c), a neutral particle part (n), and a missing particle part (m). The KSFW moments are then defined using the relation:

$$H^{so}_{xl} = \sum_i \sum_{j,x} |\vec{p}_{jx}| P_l(\cos\theta_{i,jx}),$$

where i runs over the B candidate final-states, jx indexes the ROE in the category x ($x = c, n, m$), $\vec{p}_{jx}$ is the momentum of particle jx, and $P_l(\cos\theta_{i,jx})$ is the lth order Legendre polynomial of the cosine of the angle between particles i and jx. Similarly

$$H^{oo}_{l} = \sum_j \sum_k |\vec{p}_j||\vec{p}_k| P_l(\cos\theta_{j,k}) \ (l = \text{even})$$

$$H_l^{oo} = \sum_j \sum_k Q_j Q_k |\vec{p}_j||\vec{p}_k| P_l(\cos\theta_{j,k}) \ (l = \text{odd}),$$

where j, k run over the ROE, and Q_j and Q_k are the charges of jth and kth particles, respectively.

• KSFWVariables(mm2): missing mass squared.

• KSFWVariables(et): transverse energy.

• CLEO cones: These variables were introduced by the CLEO collaboration [67], based on the sum of the magnitudes of momenta of all particles within angular regions around the thrust axis in intervals of 10° resulting in nine concentric cones.

• thrustOm: The magnitude of thrust axis for the reconstructed B candidate, where the thrust is defined as:

$$T = \max_{\hat{n}} \frac{\sum_i \vec{p}_i \cdot \hat{n}}{\sum_i |\vec{p}_i|}$$

Here $\vec{p}_i$ is the momentum of the ith daughter of the reconstructed B candidate and $\hat{n}$ is a unit vector along the direction that maximizes the total longitudinal projection of momenta.

• cosTBTO: The cosine of the angle between the thrust axis of signal B and that of ROE.

• cosTBz: The cosine of the angle between the thrust axis of signal B and that of beam axis.

• thrustAxisCosTheta: The cosine of the polar angle of B momentum calculated in the c.m. frame

• R_2: The normalized second Fox–Wolfram moment, defined as:

$$R_2 = \frac{H_2}{H_0}, \text{ where } H_k = \sum_{i,j} |\vec{p}_i||\vec{p}_j| P_k(\cos\theta_{i,j}) \ (k\text{th order Fox–Wolfram moment}),$$

$\vec{p}_i$ ($\vec{p}_j$) is the momentum of the ith (jth) final-state of the reconstructed B candidate, θ_{ij} is the angle between $\vec{p}_i$ and $\vec{p}_j$, and P_k is the kth-order Legendre polynomial.

• cosHelicityAngleMomentum: The cosine of the angle between the two-body decay axis (or three-body decay plane) in B-frame and the momentum of the B meson in the lab frame.

We choose the variables whose correlations with ΔE and $M'_{\rm bc}$ are below 5% to avoid sculpting. Distributions of input variables and their importances can be found in Appendix A. The BDT output (Fig. 4.1) shows a clear difference between the two event categories. After applying a loose (0.6) continuum suppression requirement, the distributions of $M'_{\rm bc}$ and ΔE are shown in Fig. 4.2. This criterion allows us to reject approximately 93% of the continuum background while retaining 80% of the signal. We incorporate the remainder of the continuum suppression output as an additional dimension into the combined fit. By doing so, we enhance the precision of physics observables. Due to the complexity involved in analytically modeling the

distribution of the BDT classifier output, denoted as $C_{\rm BDT}$, we transform it into a new variable:

$$C'_{\rm BDT} = \ln\left(\frac{C_{\rm BDT} - 0.6}{1.0 - C_{\rm BDT}}\right), \tag{4.1}$$

$$\tag{4.2}$$

where 0.6 (1.0) is the minimum (maximum) possible value of the remaining $C_{\rm BDT}$ distribution. The $C'_{\rm BDT}$ can be parametrized by one or more Gaussian functions. Figure 4.3 shows the $C'_{\rm BDT}$ distribution for the simulated signal sample.

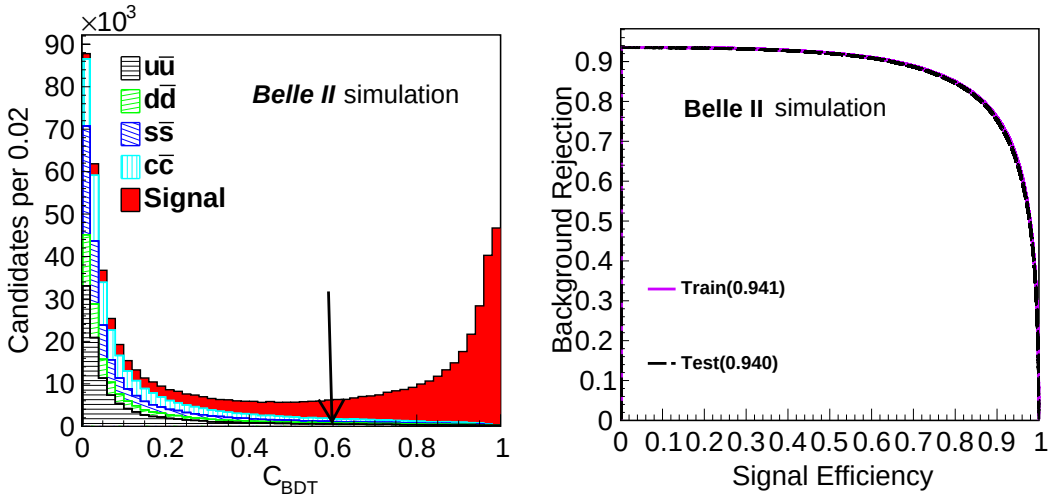

Figure 4.1: BDT output distributions (left) for signal and background events and ROC curve (right) for background rejection vs. signal efficiency.

4.2 $B\overline{B}$ background

We use 1ab^{-1} of simulated samples to evaluate the background contribution arising from B decays involving both CKM-favored $b \to c$ and rare $b \to u, d, s$ transitions within the signal region. Figure 4.4 shows the $M'_{\rm bc}$ and ΔE distributions corresponding to the $B\overline{B}$ background contribution in the simulated sample. We do not find any $B\overline{B}$ events peaking in the ΔE signal region. Mostly $B\overline{B}$ background comes from $B^+ \to \rho^+ K^0, K^{*+}(892)\pi^0, X_{s,u}\gamma, a_1^+(1260)K^0$ and $B^0 \to f_2(1270)K^0, f_0(980)K^0, X_{s,d}\gamma, K_S^0 K_S^0, K^0\eta'$ (arranged in a descending order). The first two decays have a dominant contribution in $B\overline{B}$ background that are 43% and 32% respectively.

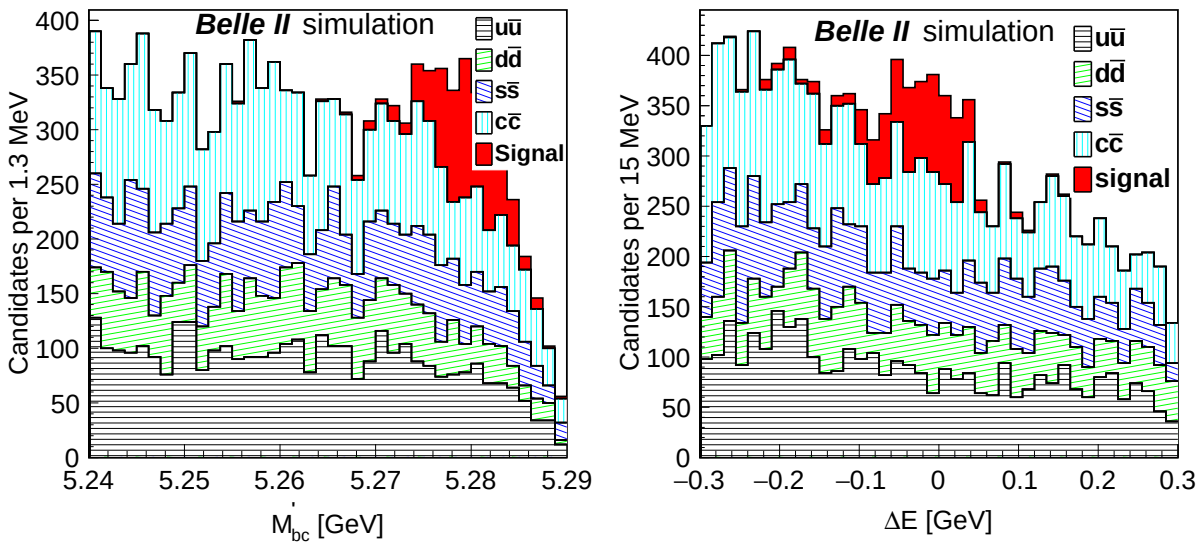

Figure 4.2: M'_{bc} and ΔE distributions obtained after the continuum suppression.

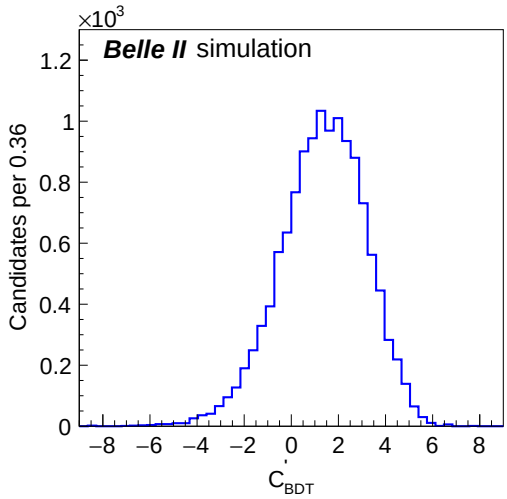

Figure 4.3: C'_{BDT} distribution for the signal simulated sample.

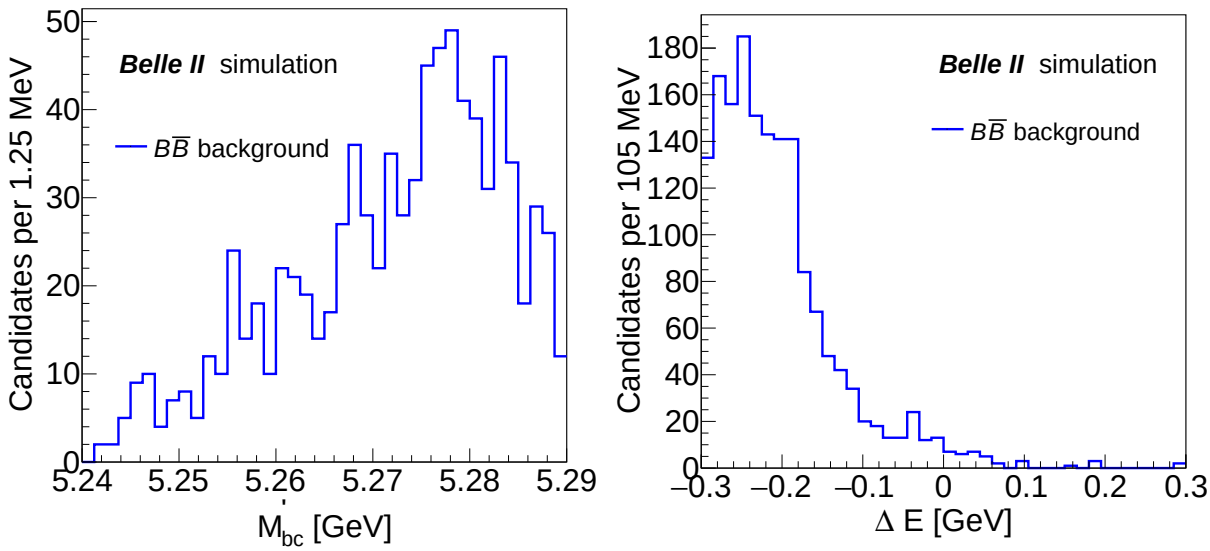

Figure 4.4: M'_{bc} and ΔE distributions for $B\overline{B}$ background events.

Chapter 5

Flavour tagging and decay-time selection

5.1 Flavour tagging

The b-flavor of the accompanying tag-side B meson (B_{tag}) is determined from inclusive properties of the particle's tracks that are not associated with the reconstructed $B^0 \to K_S^0\pi^0$ decays. Such tracks must have a minimum momentum of 50 MeV and at least one hit each in the PXD, SVD, and CDC subdetectors. We also apply a similar interaction region constraint as that used for tracks on the signal side. We use a category-based multivariate algorithm for B_{tag} flavor tagging [69]. The algorithm outputs two parameters, tag-side B meson flavor q (+1 for B^0 and 1 for $\overline{B}^0$) and r, which is an event-by-event tagging quality (dilution factor) ranging from zero for no flavor discrimination to one for unambiguous flavor assignment. Figure 5.1 shows the $q \cdot r$ distributions for signal and background components. The dataset is divided into seven r bins $(0, 0.1, 0.25, 0.45, 0.6, 0.725, 0.875, 1.0)$ that contain similar numbers of events, but have different signal-to-background ratios. We also employ the r-bin-dependent partial efficiency (ε_r), wrong tag fraction (w_r), difference in wrong tag fraction between B^0 and $\bar{B}^0$ (Δw_r), and partial efficiency difference between B^0 and $\bar{B}^0$ ($\Delta\varepsilon_r$) that are necessary to extract CP parameters. These tagging parameters are listed in Tables 5.1 and 5.2 and fixed to the values obtained from $B^0 \to D^{(*)-}\pi^+$ decays [69]. The tagging efficiency ε defined as the fraction of candidate events to which a flavor tag can be assigned. The effective tagging efficiency $\varepsilon_{\text{eff}} = \sum_r \varepsilon_r(1 - 2w_r)^2$ is $(30.0 \pm 1.2)\%$. The w_r and $\Delta\varepsilon_r$ values are in the ranges 2–48% and 0.8–3.6%, respectively.

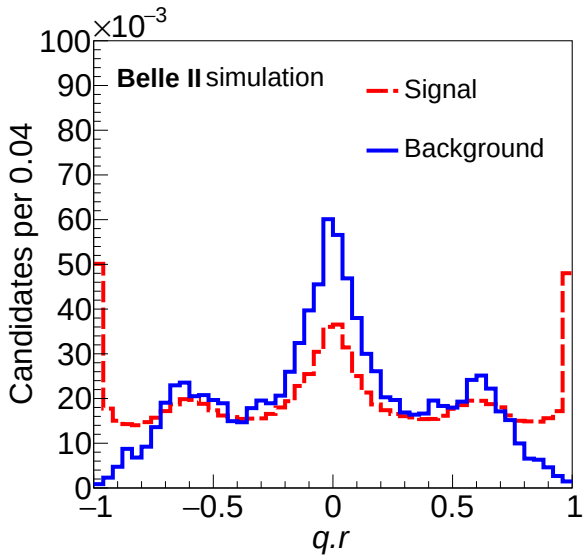

Figure 5.1: $q \cdot r$ distributions for signal and background in simulated events.

Table 5.1: The definition of each r-bin interval and corresponding flavor tagging parameters for simulation.

r-bin	r interval	ε_r	w_r	Δw_r	$\Delta\varepsilon_r$
0	0.000 – 0.100	0.1655	0.4725 ± 0.0031	−0.0008 ± 0.0063	−0.0143 ± 0.0071
1	0.100 – 0.250	0.1527	0.4137 ± 0.0032	0.0119 ± 0.0065	−0.0099 ± 0.0073
2	0.250 – 0.450	0.1585	0.3220 ± 0.0031	−0.0062 ± 0.0062	−0.0026 ± 0.0071
3	0.450 – 0.600	0.1385	0.2291 ± 0.0031	−0.0007 ± 0.0062	0.0003 ± 0.0075
4	0.600 – 0.725	0.1203	0.1638 ± 0.0031	−0.0040 ± 0.0062	0.0185 ± 0.0079
5	0.725 – 0.875	0.1134	0.0930 ± 0.0027	−0.0141 ± 0.0055	0.0281 ± 0.0078
6	0.875 – 1.000	0.1511	0.0181 ± 0.0017	−0.0039 ± 0.0034	−0.0228 ± 0.0064

Table 5.2: The definition of each r-bin interval and corresponding flavor tagging parameters for data.

r-bin	r interval	ε_r	w_r	Δw_r	$\Delta\varepsilon_r$
0	0.000 – 0.100	0.1580	0.4804 ± 0.0054	−0.0068 ± 0.0108	−0.0240 ± 0.0122
1	0.100 – 0.250	0.1553	0.4240 ± 0.0054	0.0381 ± 0.0109	0.0138 ± 0.0123
2	0.250 – 0.450	0.1652	0.3410 ± 0.0051	−0.0188 ± 0.0102	−0.0115 ± 0.0118
3	0.450 – 0.600	0.1392	0.2362 ± 0.0053	−0.0070 ± 0.0105	0.0088 ± 0.0126
4	0.600 – 0.725	0.1161	0.1675 ± 0.0053	0.0197 ± 0.0106	0.0368 ± 0.0135
5	0.725 – 0.875	0.1145	0.1073 ± 0.0048	−0.0005 ± 0.0096	−0.0202 ± 0.0133
6	0.875 – 1.000	0.1517	0.0274 ± 0.0030	0.0024 ± 0.0060	−0.0123 ± 0.0108

5.2 Δt and $\Delta t_{\rm err}$ selection

To measure the decay-time difference Δt, it is essential to accurately determine the positions of both the signal and tag-side B decay vertices. The information required to determine these vertices is obtained from the position and spread of the e^+e^- interaction region, which is represented by a three-dimensional Gaussian distribution. The position of the signal B vertex is determined by projecting the flight direction of $K^0_{\rm S}$, obtained from its decay vertex and momentum, back to the interaction region. We approximate Δt as $\Delta\ell/\beta\gamma\gamma^*$ [70], where $\Delta\ell$ is the distance between the signal and tag-side vertices along the direction of the e^- beam. $\beta\gamma$ (≈ 0.28) is the Lorentz boost of the $\Upsilon(4S)$ in the laboratory frame, and γ^* (≈ 1.002) is the Lorentz factor of the B^0 meson in the c.m. frame. The point where the $K^0_{\rm S}$ flight projection intersects with the interaction region offers a reliable estimate of the signal B decay vertex. This is due to the small transverse flight length of the B^0 meson ($\approx 40\,\mu$m) and the small transverse size of the interaction region ($\approx 10\,\mu$m) when compared to the B^0 flight length along the boost direction ($\approx 140\,\mu$m). In both the signal and control mode, we observe a double peak structure in the distribution of decay-time uncertainties ($\Delta t_{\rm err}$), as shown in Fig. 5.2. The nature of the distribution depends on the first hits of $K^0_{\rm S}$ tracks (both π^+ and π^-) in VXD. Specifically, in Figs. 5.3 and 5.4, we show the distribution of the number of PXD and SVD hits for both $K^0_{\rm S}$ daughters against $\Delta t_{\rm err}$. To better understand it, we have also studied $\Delta t_{\rm err}$ with different conditions of PXD hits as shown in Fig. 5.5. The first peak in $\Delta t_{\rm err}$ arises when the $K^0_{\rm S}$ decays within the inner part of the VXD, resulting in more hits in the PXD layers. On the other hand, the second peak occurs when neither of the $K^0_{\rm S}$ decay products have any PXD hit. In Figs. 5.2 and 5.5, we notice that in the control mode, the contribution of the second peak is smaller compared to the signal channel. This difference can be attributed to the momentum of K^0_S. In the control mode, the momentum of K^0_S is smaller compared to that in the signal mode, which leads to the majority of decays occurring inside the VXD. We select events in which Δt is well-measured by requiring $|\Delta t| < 10.0$ ps and $\Delta t_{\rm err} < 2.5$ ps as shown in Fig. 5.6, where $\Delta t_{\rm err}$ is estimated event-by-event. Figure 5.7 shows the correlation between Δt and $\Delta t_{\rm err}$, which is found to be less than 1%. Since these are independent quantities, applying a $\Delta t_{\rm err}$ criterion does not introduce any subtle biases. The Δt distribution of these events is fitted to determine C and S, what we call the first or time-dependent (TD) subsample. For the remaining events, about 40% of the total, the Δt distribution is not included in the fit. However, these events are still useful to constrain C, which is sensitive to the relative yields of B^0 and $\bar{B}^0$ decays. We refer to these

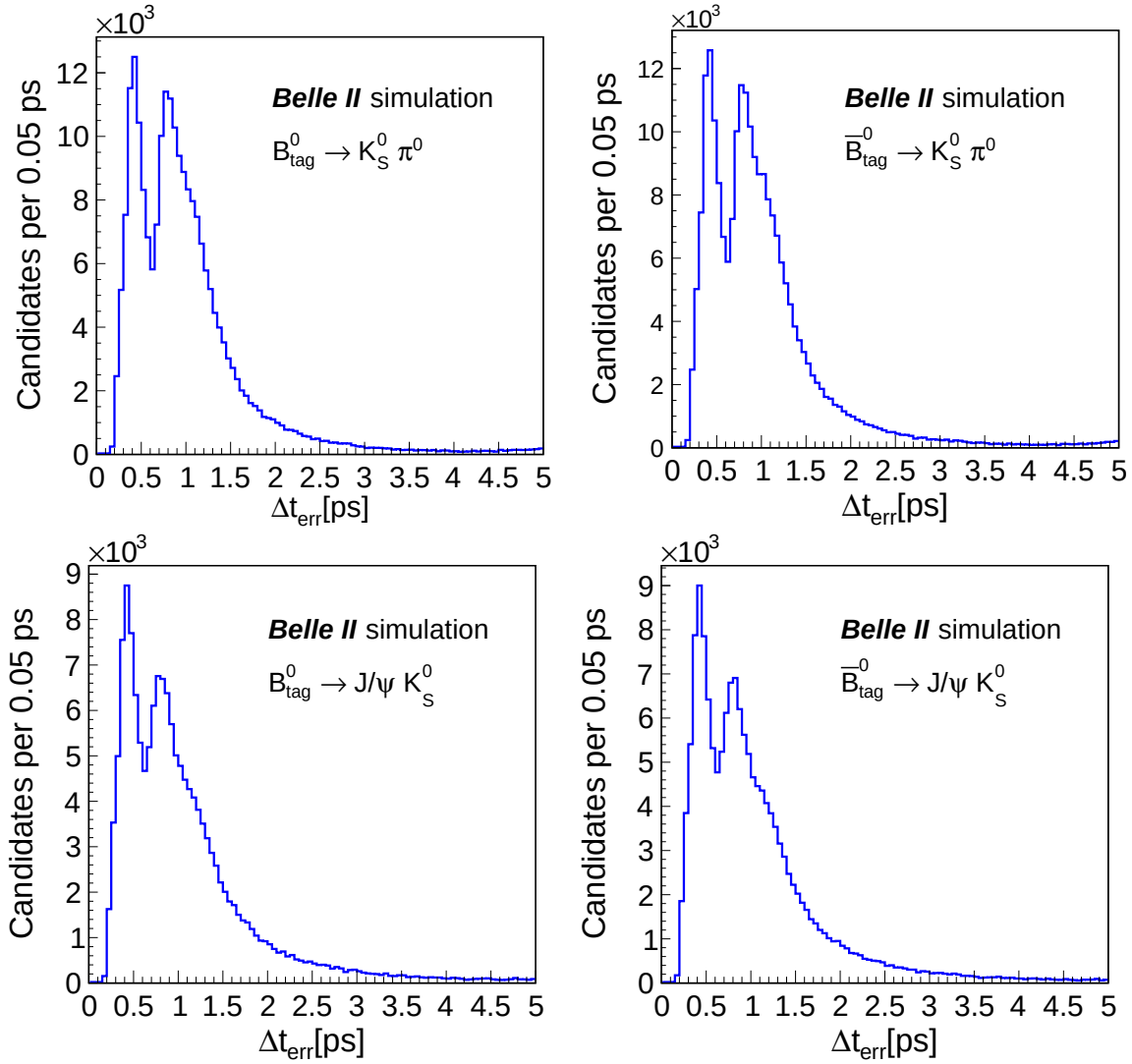

Figure 5.2: Distribution of $\Delta t_{\rm err}$ for B^0 and $\bar{B}^0$ tag-separated in $B^0 \to K_S^0\pi^0$ (upper) and $B^0 \to J/\psi K_S^0$ (lower).

events as the second or time-integrated (TI) subsample.

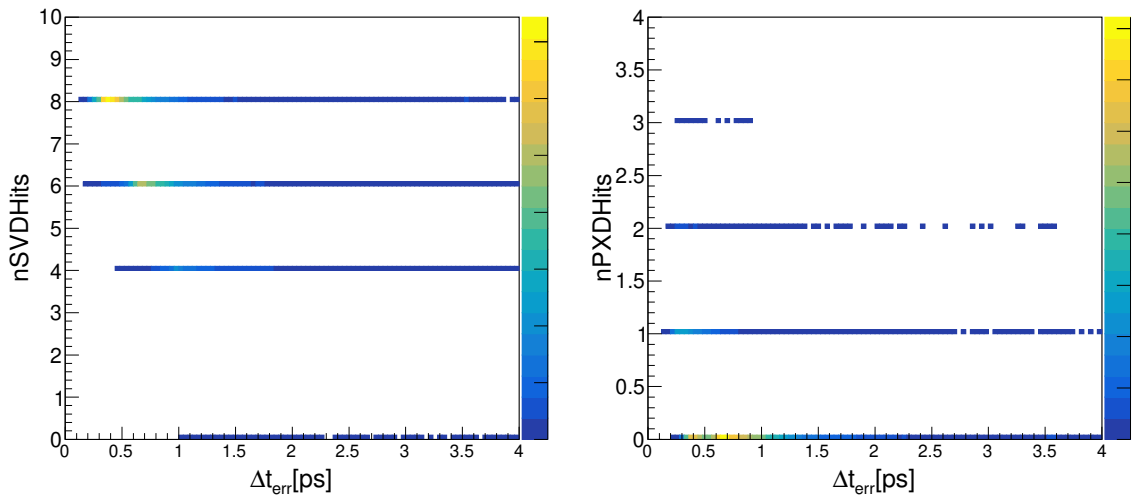

Figure 5.3: Number of PXD and SVD hits of both K_{s}^0 daughters combined vs. Δt_{err} distribution for the $B^0 \to K_S^0 \pi^0$ sample.

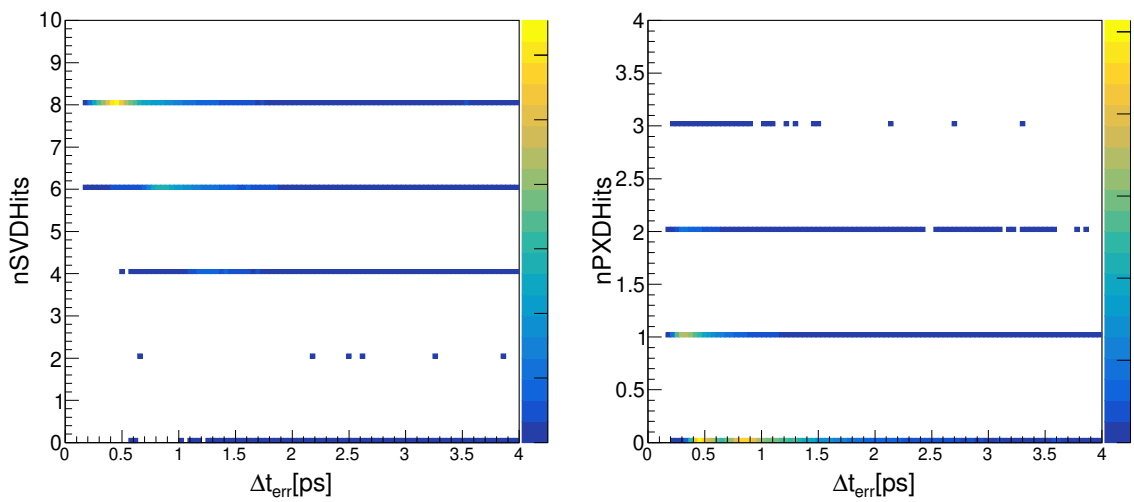

Figure 5.4: Number of PXD and SVD hits of both K_{s}^0 daughters combined vs. Δt_{err} distribution for the $B^0 \to J/\psi K_S^0$ sample.

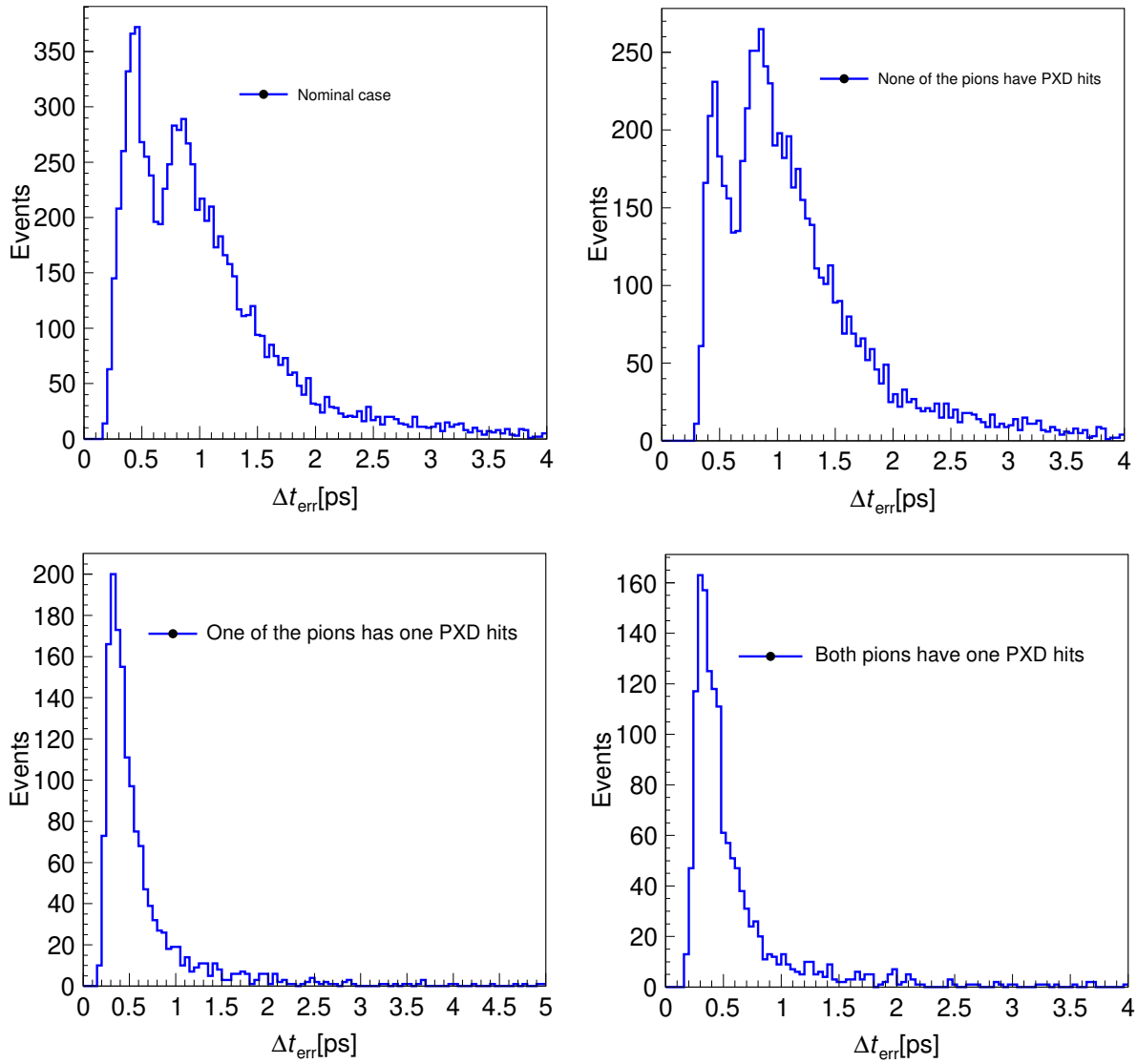

Figure 5.5: Distributions of Δt_{err} with different criteria on PXD hits.

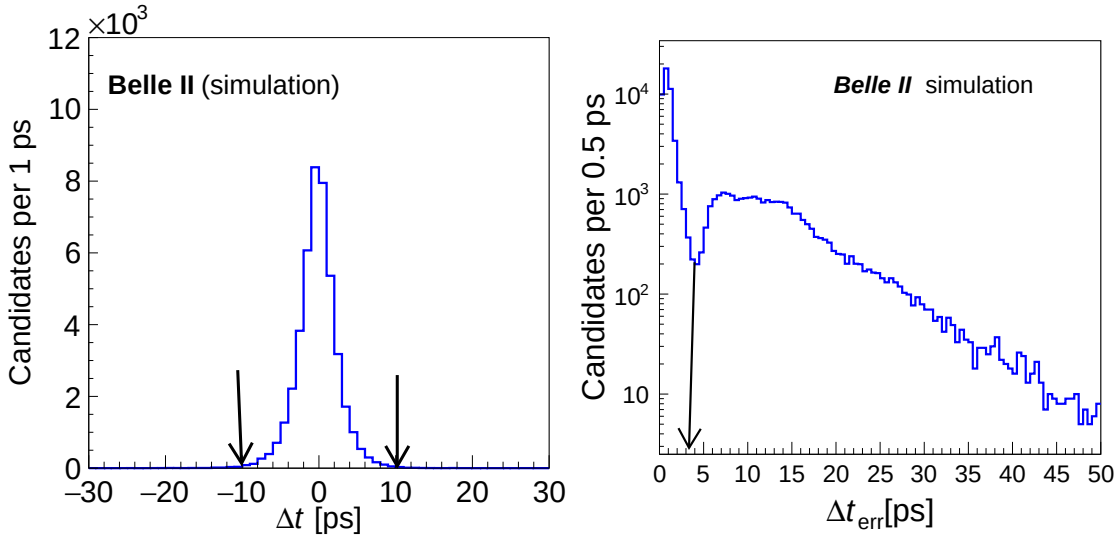

Figure 5.6: Δt and Δt_{err} distributions in simulated signal events.

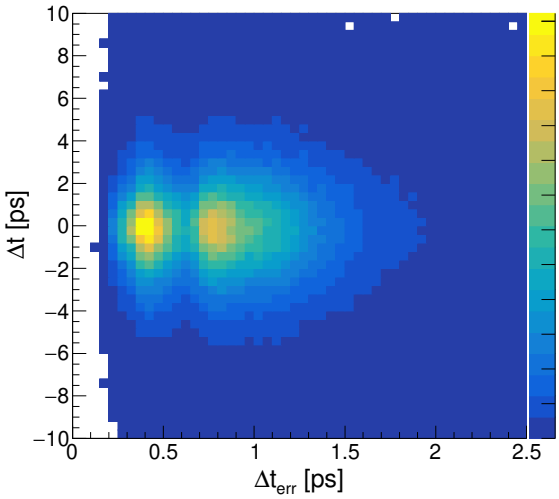

Figure 5.7: Correlation between Δt and Δt_{err} distributions in signal simulated sample.

5.3 Resolution function

In Fig. 5.8 we show the resolution function $\mathcal{R}(\Delta t_{\rm rec} - \Delta t_{\rm MC})$ that characterizes the distribution of residual $\Delta t_{\rm res} = \Delta t_{\rm rec} - \Delta t_{\rm MC}$, where $\Delta t_{\rm rec}$ and $\Delta t_{\rm MC}$ are the difference in decay times calculated using the measured and true value, respectively. We model the decay time resolution with a double Gaussian function convolved with an exponential tail, which is the simplified version of the resolution function used in Eq.12 [68]. The resolution function is defined as

$$\begin{aligned}\mathcal{R}(\Delta t_{\rm res}) = \quad & (1 - f_{\rm tail}) \cdot G(\Delta t_{\rm res}; \mu_{\rm main} \cdot \Delta t_{\rm err}, \sigma_{\rm main} \cdot \Delta t_{\rm err}) \\ & +(1 - f_{\rm exp}) \cdot f_{\rm tail} \cdot G(\Delta t_{\rm res}; \mu_{\rm tail} \cdot \Delta t_{\rm err}, \sigma_{\rm tail} \cdot \Delta t_{\rm err}) \\ & +f_{\rm tail} \cdot f_{\rm exp} \cdot G(\Delta t_{\rm res}; \mu_{\rm tail} \cdot \Delta t_{\rm err}, \sigma_{\rm tail} \cdot \Delta t_{\rm err}) \\ & \otimes(f_R \cdot \exp_R(-\Delta t_{\rm res}/C \cdot \Delta t_{\rm err}) \\ & +(1 - f_R) \cdot \exp_L(\Delta t_{\rm res}/C \cdot \Delta t_{\rm err})),\end{aligned} \tag{5.1}$$

where

- $\mu_{\rm main}$ and $\sigma_{\rm main}$ are the mean and sigma of the main Gaussian;
- $\mu_{\rm tail}$ and $\sigma_{\rm tail}$ are the mean and sigma of the tail Gaussian;
- C is an exponential constant describing the length of the exponential tail;
- $f_{\rm tail}$ is the fraction of events belonging to the tail Gaussian;
- $f_{\rm exp}$ is the fraction of events belonging to the exponential part;
- f_R is the fraction of events belonging to the right tail of the exponential part.

Table 5.3 presents the resolution function parameters obtained from the fit to the simulated signal of $B^0 \to K^0_S \pi^0$ decay. The simulation in Fig. 5.9 shows that the $\Delta t_{\rm err}$ distributions for both signal and background are identical. We also find a good agreement between data and simulation as shown in Fig. 5.9.

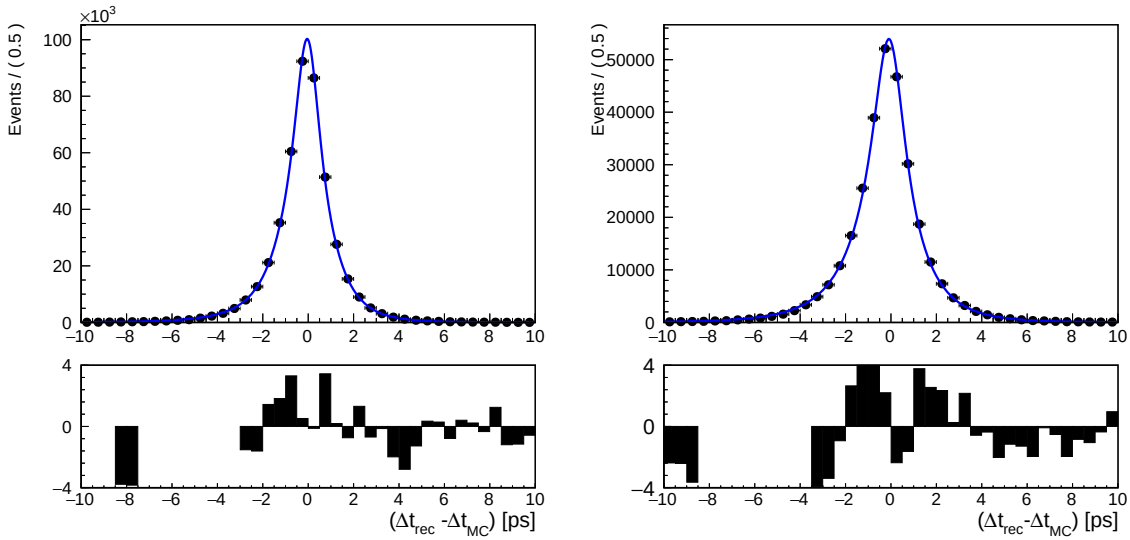

Figure 5.8: Fit projections of residual $\mathcal{R}(\Delta t_{\rm rec} - \Delta t_{\rm MC})$ distribution from simulated $B^0 \to K_S^0 \pi^0$ (left) and $B^0 \to J/\psi K_S^0$ (right) events.

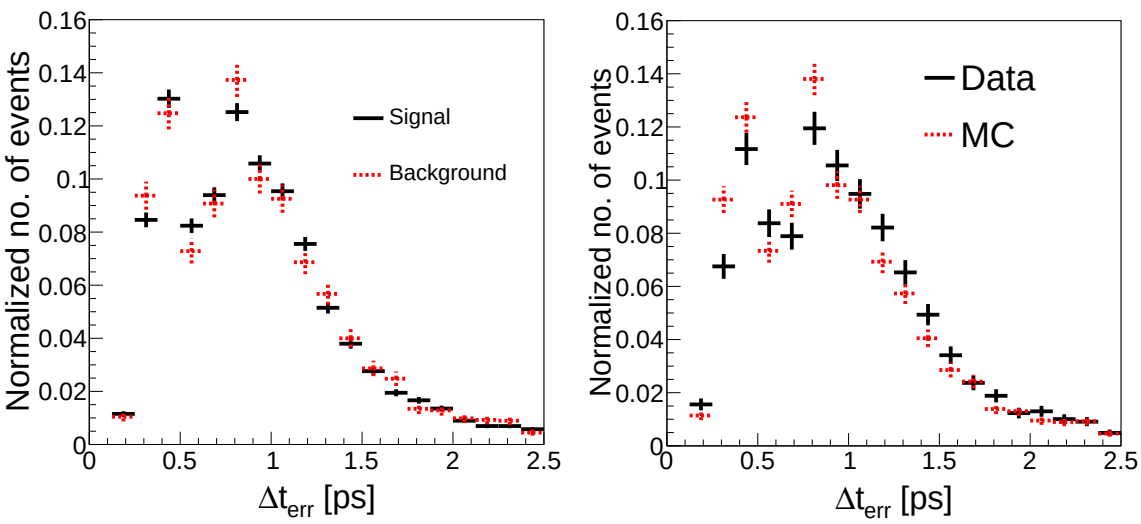

Figure 5.9: Normalized $\Delta t_{\rm err}$ distributions between signal and background events (left). Comparison between data and MC shown in right.

Table 5.3: Resolution function parameters derived from $B^0 \to K_S^0\pi^0$ signal simulated fit.

Parameters	value
μ_{main}	-0.1057 ± 0.0027
σ_{main}	1.1699 ± 0.0029
μ_{tail}	-0.6937 ± 0.0217
σ_{tail}	2.2574 ± 0.0156
C [ps^2]	1.3700 ± 0.0652
f_{tail}	0.1428 ± 0.0028
f_{exp}	0.1046 ± 0.0064
f_R	0.2000 ± 0.0163

Chapter 6

Time-dependent *CP* asymmetry measurement

6.1 Fit strategy

We perform an extended unbinned maximum-likelihood fit to the variables ΔE, $M'_{\rm bc}$, Δt, and $C'_{\rm BDT}$ in order to measure the *CP* parameters. For both subsamples, the likelihood includes one-dimensional probability density functions (PDFs) for $M'_{\rm bc}$, ΔE, and $C'_{\rm BDT}$; for the first subsample, the likelihood also includes a PDF for Δt that depends on the flavor tag q. The extended likelihood is

$$\mathcal{L}_{\rm TD} = \prod_r \frac{e^{-\sum_j n_{r,j}}}{N_r!} \prod_{i\varepsilon {\rm TD}}^{N_r} \sum_j n_{r,j} \mathcal{P}^i_{r,j}(\Delta E, M'_{\rm bc}, C'_{\rm out}, \Delta t), \tag{6.1}$$

$$\mathcal{L}_{\rm TI} = \prod_r \frac{e^{-\sum_j n_{r,j}}}{N_r!} \prod_{k\varepsilon {\rm TI}}^{N_r} \sum_j n_{r,j} \mathcal{P}^k_{r,j}(\Delta E, M'_{\rm bc}, C'_{\rm out}),$$

$$\mathcal{L}_{\rm Comb} = \mathcal{L}_{\rm TD} \cdot \mathcal{L}_{\rm TI}, \tag{6.2}$$

where $n_{r,j} = n_j \varepsilon_{r,j}$ is the yield of event category j for bin r, N_r is the total number of events for r bin, and $\mathcal{P}^i_{r,j}(\mathcal{P}^k_{r,j})$ is the PDF of the same category for event $i(k)$ in bin r. TD (TI) represents the subset of events with (without) Δt information. In the combined fit (TD+TI), we perform a simultaneous fitting of the two subsamples. The PDFs for $M'_{\rm bc}$, ΔE, and $C'_{\rm BDT}$ are taken to be the same for both subsamples, as shown in Fig 6.1.

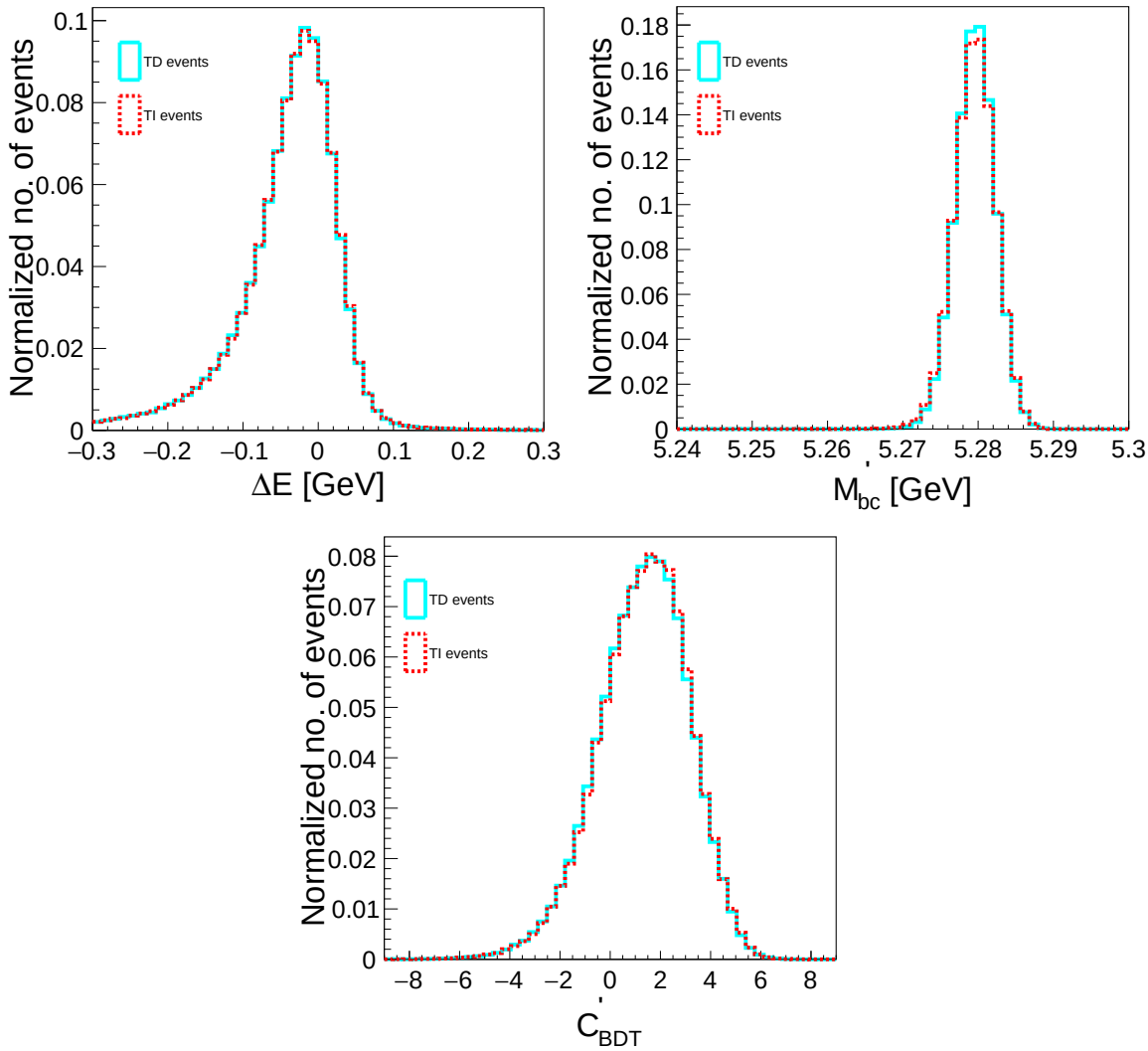

Figure 6.1: Comparison of normalized PDF shapes between TD and TI events.

6.2 Correlation among the fit variables

We check for the possible correlation among different fit variables. For this, we examine two-dimensional scatter plots for various event categories and calculate linear correlation coefficients among the variables. The 2D scatter plots illustrating the correlations between ΔE, Δt, and C'_{BDT} are presented in Figs. 6.2, 6.3, and 6.4. The linear correlations among all the fit variables are listed in Table 6.1. We find all the correlations to be below 5%. We also compare the normalized shapes of one variable in a few bins of the other, shown in from Fig. 6.5 to 6.8. We do not find any significant correlation among the variables.

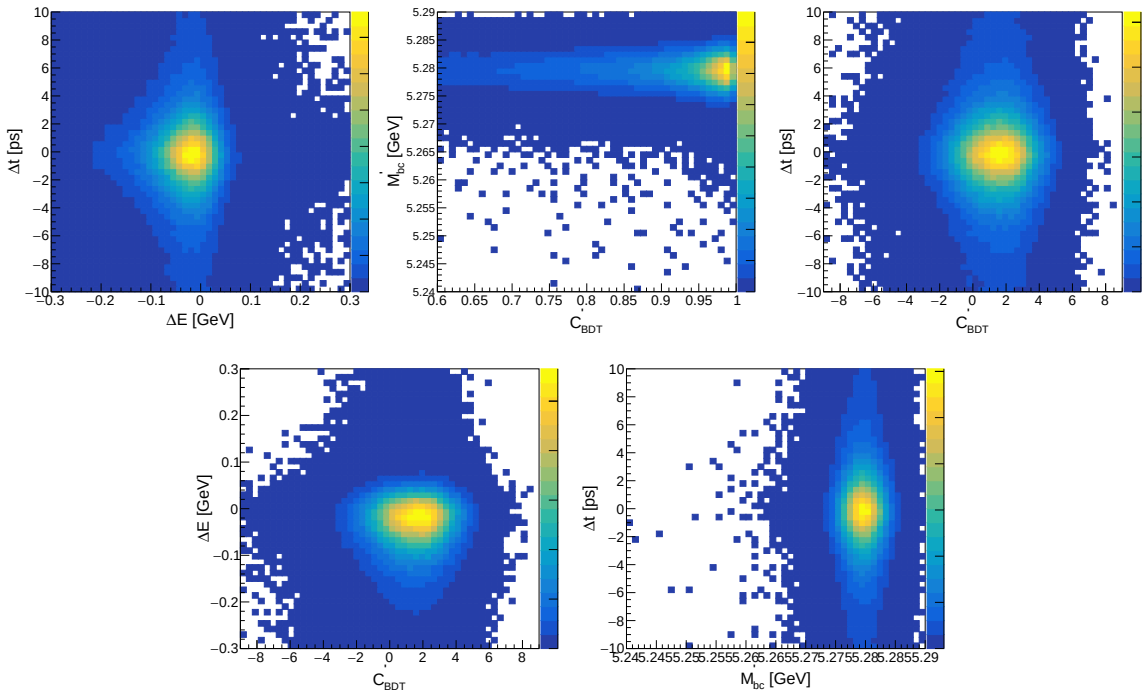

Figure 6.2: 2D scatter plots for different fit variables in signal simulation events.

Table 6.1: Linear correlation coefficients among different fit variables.

Category	ΔE–M'_{bc}	ΔE–Δt	M'_{bc}–C'_{BDT}	M'_{bc}–Δt	ΔE–C'_{BDT}	Δt–C'_{BDT}
Signal	0.7%	−0.01%	0.8%	0.7%	0.2%	0.3%
$B\overline{B}$	4.4%	−0.1%	2.1%	−0.6%	−3.7%	−3.4%
$q\overline{q}$	0.4%	−0.3%	−0.5%	0.5%	0.2%	−0.3%

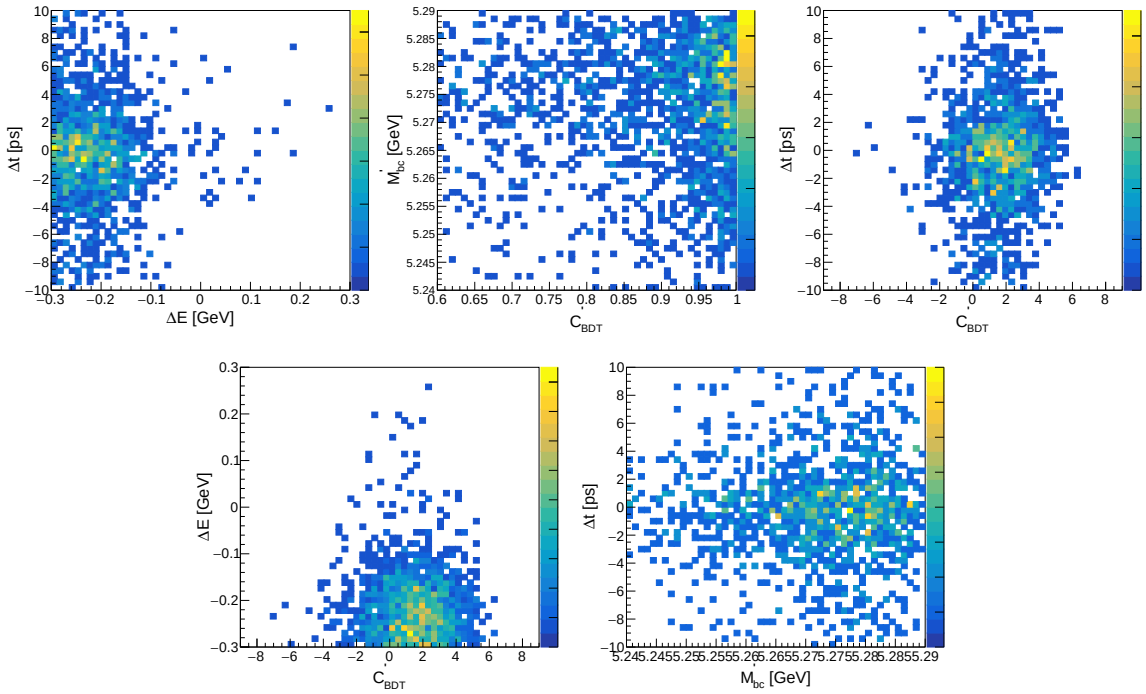

Figure 6.3: 2D scatter plots for different fit variables in $B\overline{B}$ simulation events.

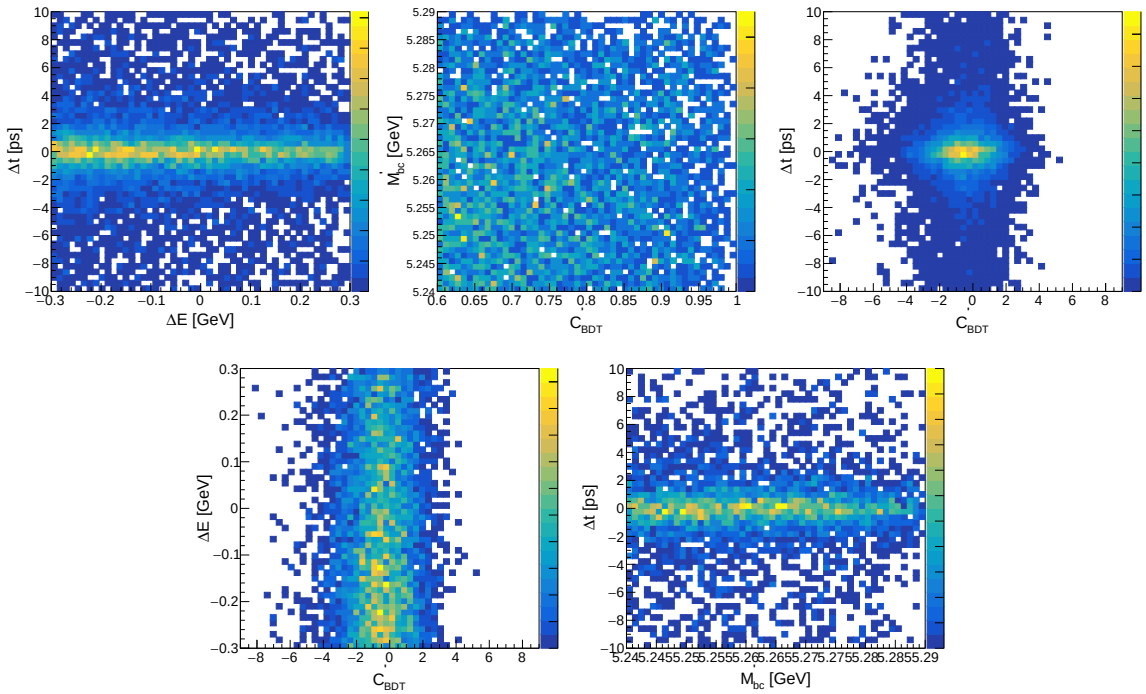

Figure 6.4: 2D scatter plots for different fit variables in $q\overline{q}$ simulation events.

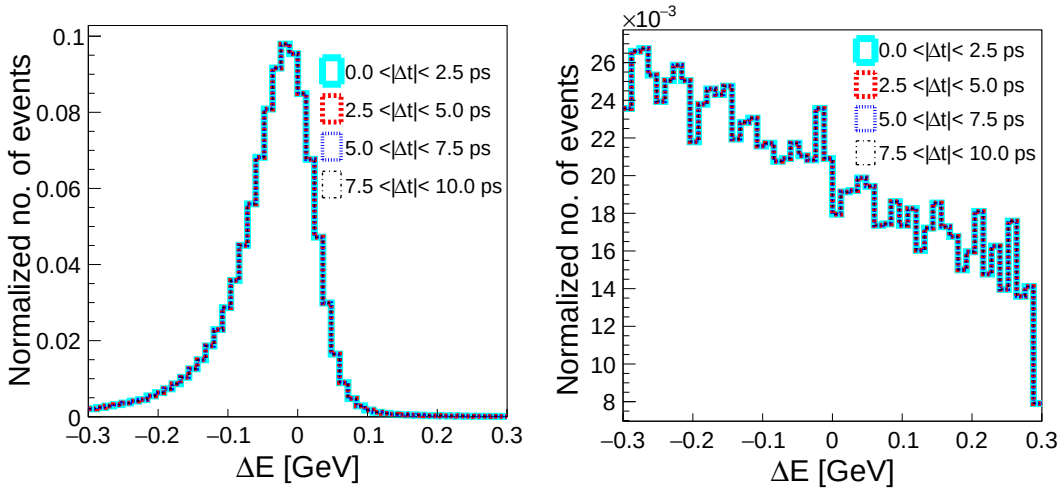

Figure 6.5: Comparison of the normalized shape of ΔE in bins of Δt for signal (left) and continuum (right) components.

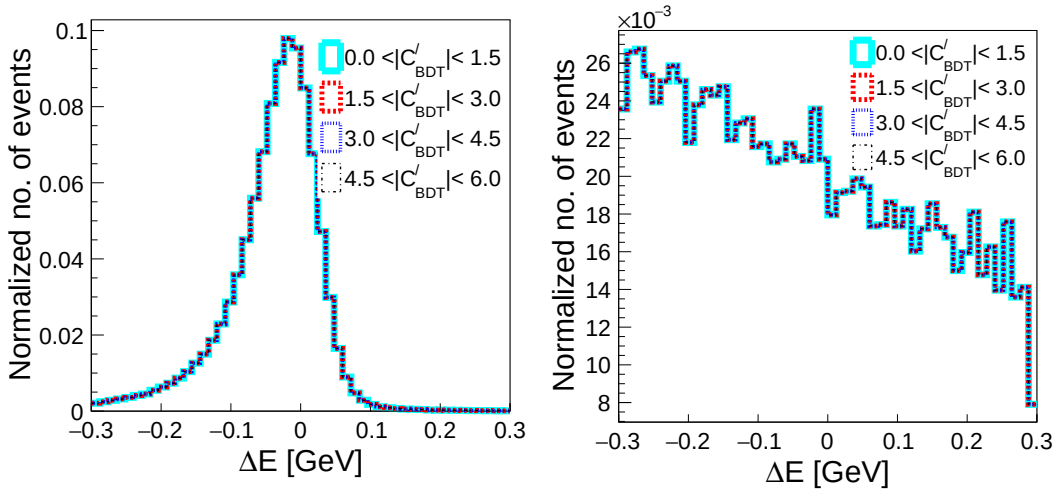

Figure 6.6: Comparison of the normalized shape of ΔE in bins of C'_{BDT} for signal (left) and continuum (right) components.

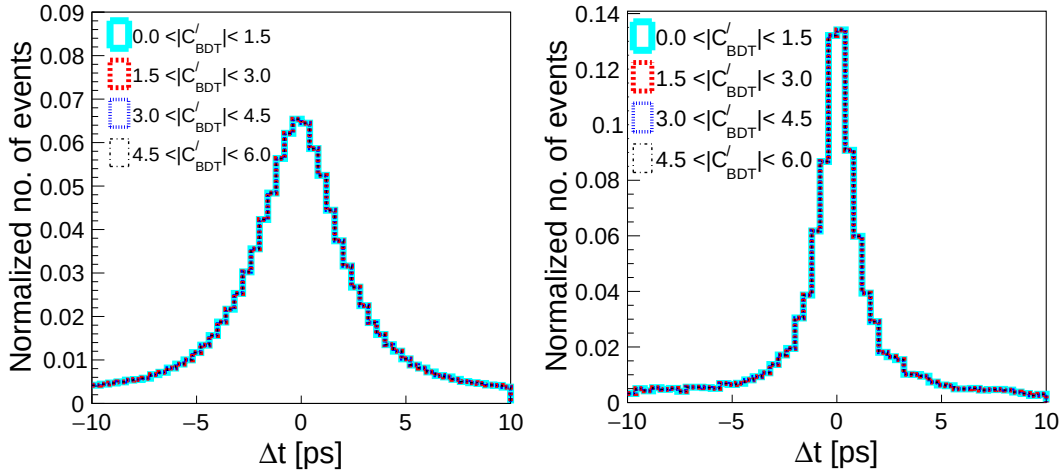

Figure 6.7: Comparison of the normalized shape of Δt in bins of C'_{BDT} for signal (left) and continuum (right) components.

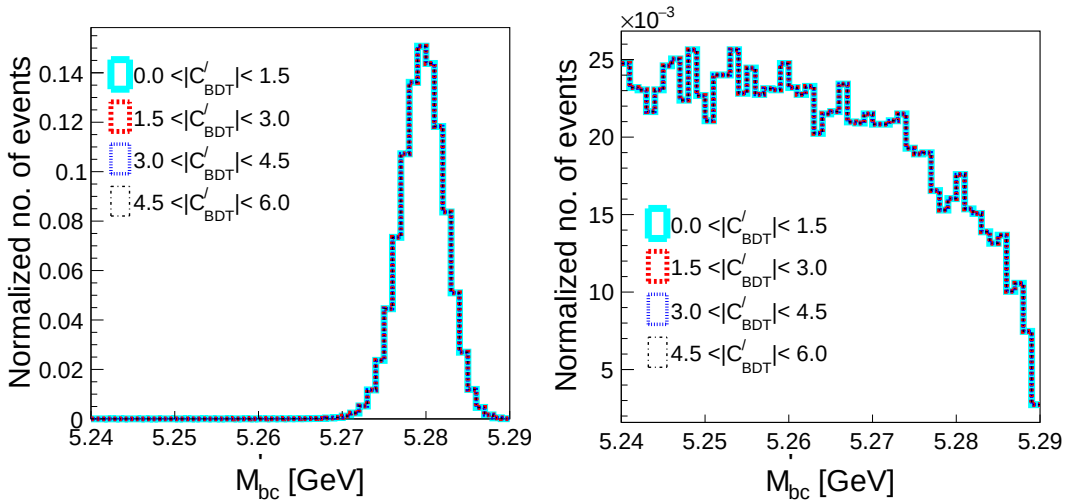

Figure 6.8: Comparison of the normalised shape of M'_{bc} in bins of C'_{BDT} for signal (left) and continuum (right) components.

6.3 Signal modeling

The PDFs for the signal component are as follows: $M'_{\rm bc}$ is modeled with the sum of a Crystal Ball [71] and a Gaussian function with a common mean; ΔE with the sum of a Crystal Ball and two Gaussian functions, all three with a common mean; and $C'_{\rm BDT}$ with the sum of asymmetric and symmetric Gaussian functions. The time-dependent signal PDF is given by,

$$\begin{aligned} P_{\rm sig}(\Delta t, q) &= \frac{e^{-|\Delta t|/\tau_{B^0}}}{4\tau_{B^0}}\Big\{[1 - q\Delta w_r + q\Delta\varepsilon_r(1-2w_r)] + [q(1-2w_r) + \Delta\varepsilon_r(1 - q\Delta w_r)] \\ &\quad [S\,\sin(\Delta m_d \Delta t) - C\cos(\Delta m_d \Delta t)]\Big\}\otimes R_{\rm sig} \end{aligned} \tag{6.3}$$

where w_r is the wrong tag fraction, Δw_r is the wrong tag fraction difference, $\Delta\varepsilon_r$ is the partial efficiency asymmetry in 7 $q \cdot r$ bins, and $\mathcal{R}_{\rm sig}$ is the Δt resolution function. We fix τ_{B^0} and Δm_d to the world averages of 1.519 ± 0.004 ps and $0.5065 \pm 0.0019\,\mathrm{ps}^{-1}$, respectively [29]. The details of the resolution function are given in Eq. 5.2. For the time-integrated analysis, we use the signal PDF as follows:

$$\begin{aligned} P_{\rm sig}(q) &= \{[1 - q\Delta w_r + q\Delta\varepsilon_r(1-2w_r)] + [q(1-2w_r) + \Delta\varepsilon_r(1 - q\Delta w_r)] \\ &\quad (2\chi_d - 1)\cdot C)\} \end{aligned} \tag{6.4}$$

where χ_d is the B^0 time-integrated mixing probability, which is fixed at the value of 0.186 ± 0.001 [29]. Figure 6.9 shows the 4D fit projections for the sixth $q \cdot r$ bin in signal simulation events. The example fit projections of the $B^0/\overline{B}^0$ tag-separated Δt distribution for all $q \cdot r$ bins are shown in Fig. 6.10.

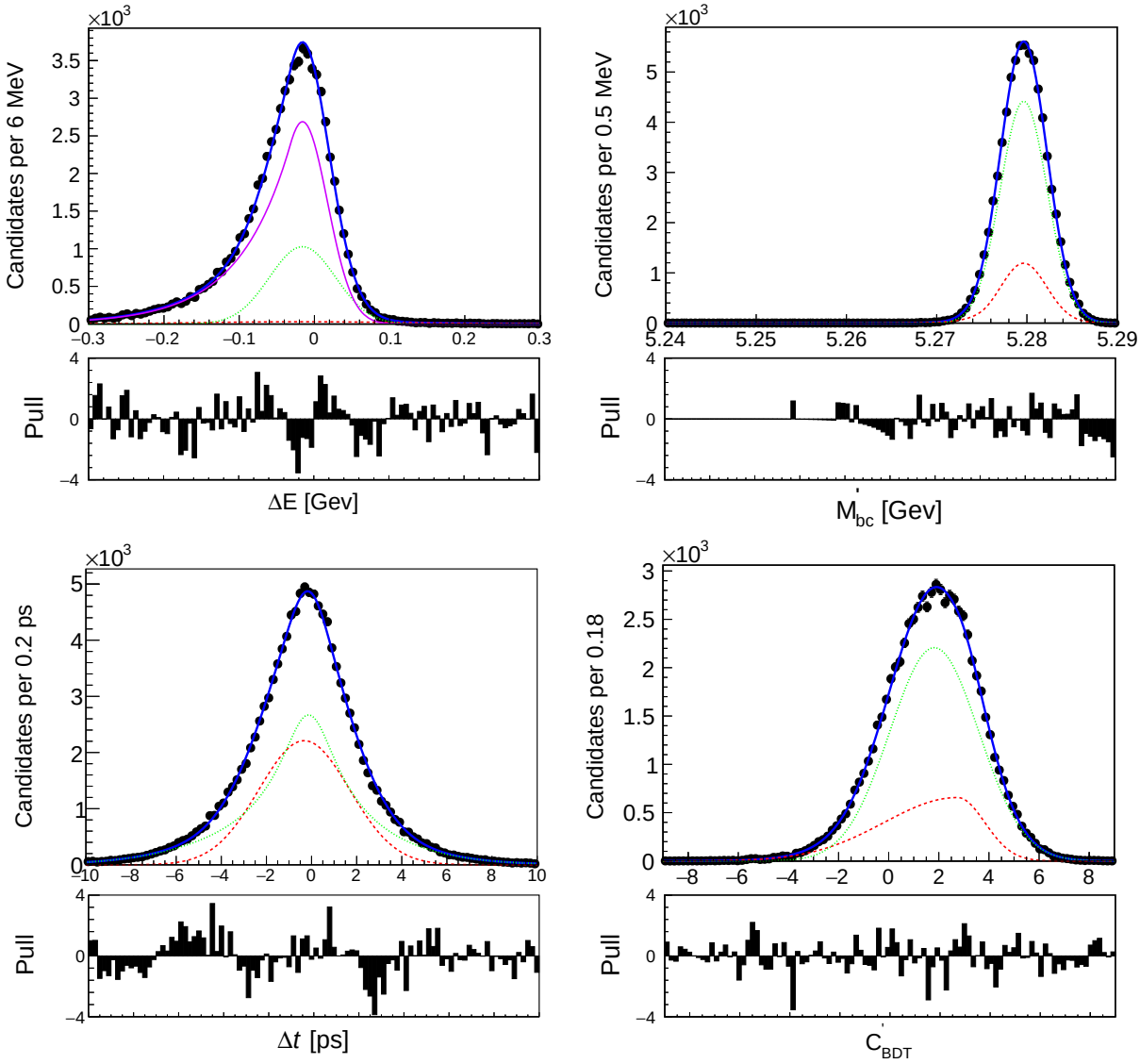

Figure 6.9: Example 4D fit projections for sixth $q \cdot r$ bin in signal simulation events.

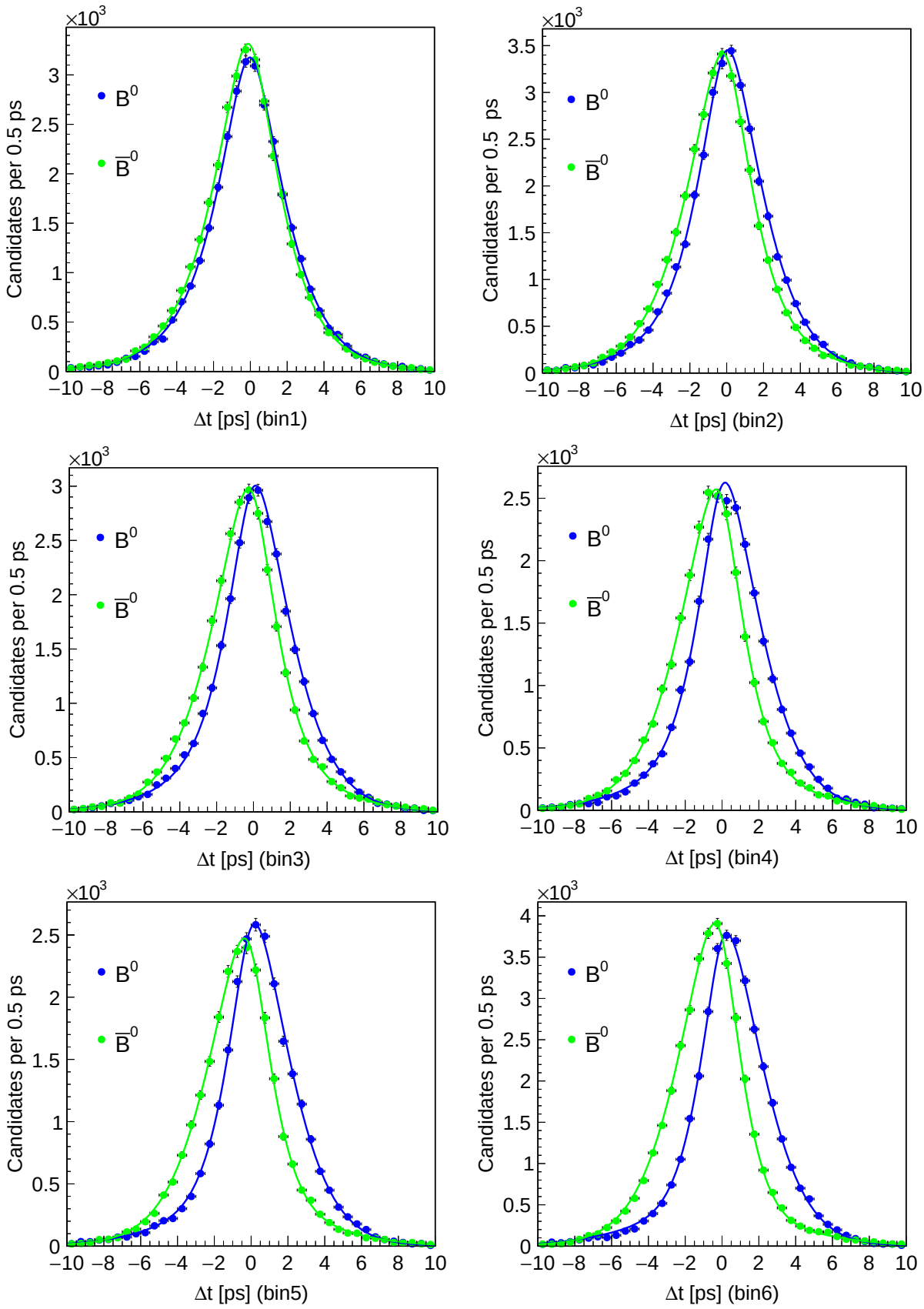

Figure 6.10: Example fit projections of $B^0/\overline{B^0}$ tag separated for all $q \cdot r$ bins in signal simulation events.

6.4 $B\overline{B}$ background modeling

A two-dimensional kernel density estimation PDF [73] is employed to account for the potential correlation between $M'_{\rm bc}$ and ΔE. The sum of asymmetric and symmetric Gaussian functions is used for $C'_{\rm BDT}$. The Δt distribution is modeled with an exponential lifetime function convolved with the resolution function given in Eq. 5.2, where the effective lifetime due to $B\overline{B}$ component is fixed from the simulation sample. We float the yield of $B\overline{B}$ background and fix its shape parameters from a fit to the simulated sample. Figure 6.11 shows the 4D fit projections for the integrated $q \cdot r$ bin in $B\overline{B}$ simulation events.

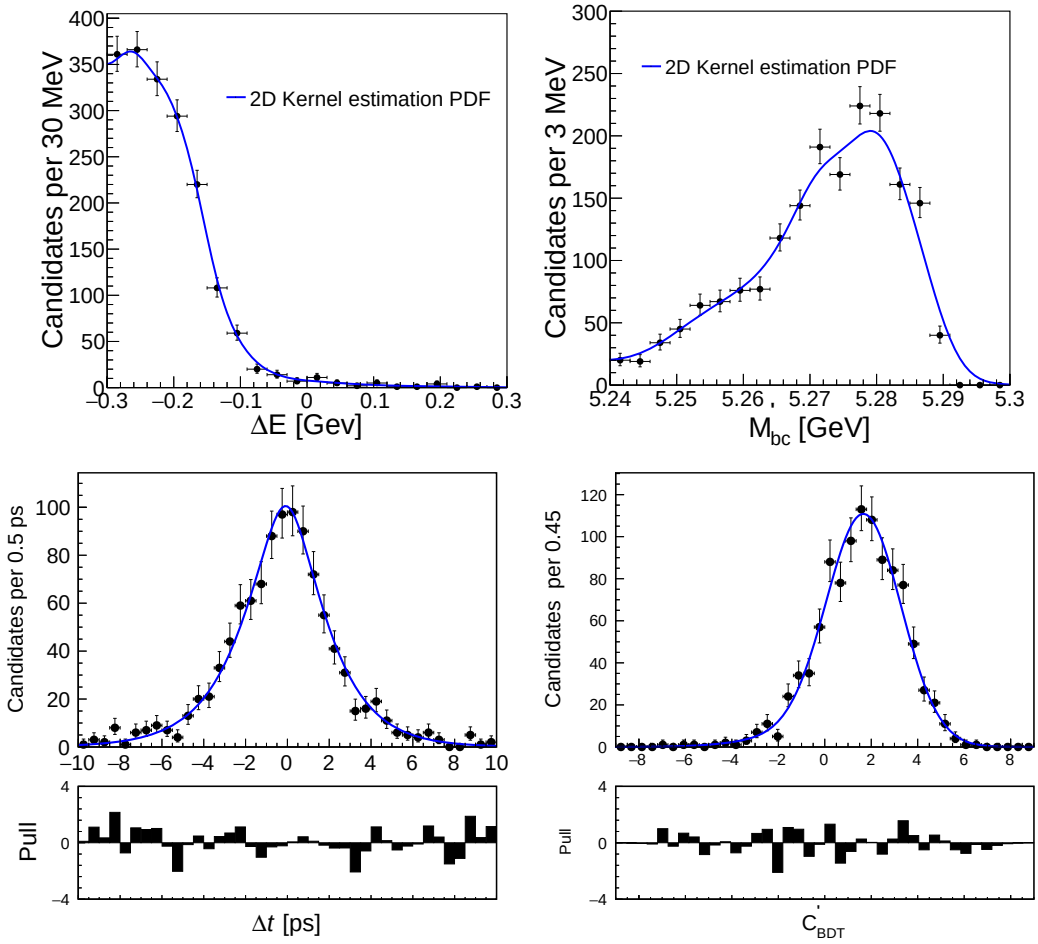

Figure 6.11: 4D fit projections for integrated $q \cdot r$ bin in $B\overline{B}$ simulation events.

6.5 Continuum background modeling

An ARGUS function [72] is used for $M'_{\rm bc}$, a straight line for ΔE, and the sum of asymmetric and symmetric Gaussian functions for $C'_{\rm BDT}$. The Δt distribution is modeled with the signal resolution function given in Eq. 5.2, as this background is dominated by prompt $K^0_{\rm S}$ decays. We float the $q\bar{q}$ background yield, ARGUS curvature parameter, and ΔE slope, but fix the ARGUS endpoint, $C'_{\rm BDT}$, and Δt shape parameters to the values obtained from the data sideband $5.24 < M'_{\rm bc} < 5.27$ GeV. All $q\bar{q}$ shape parameters are taken to be identical for all r bins. Figure 6.12 shows the 4D fit projections for the integrated $q \cdot r$ bin in continuum simulation events.

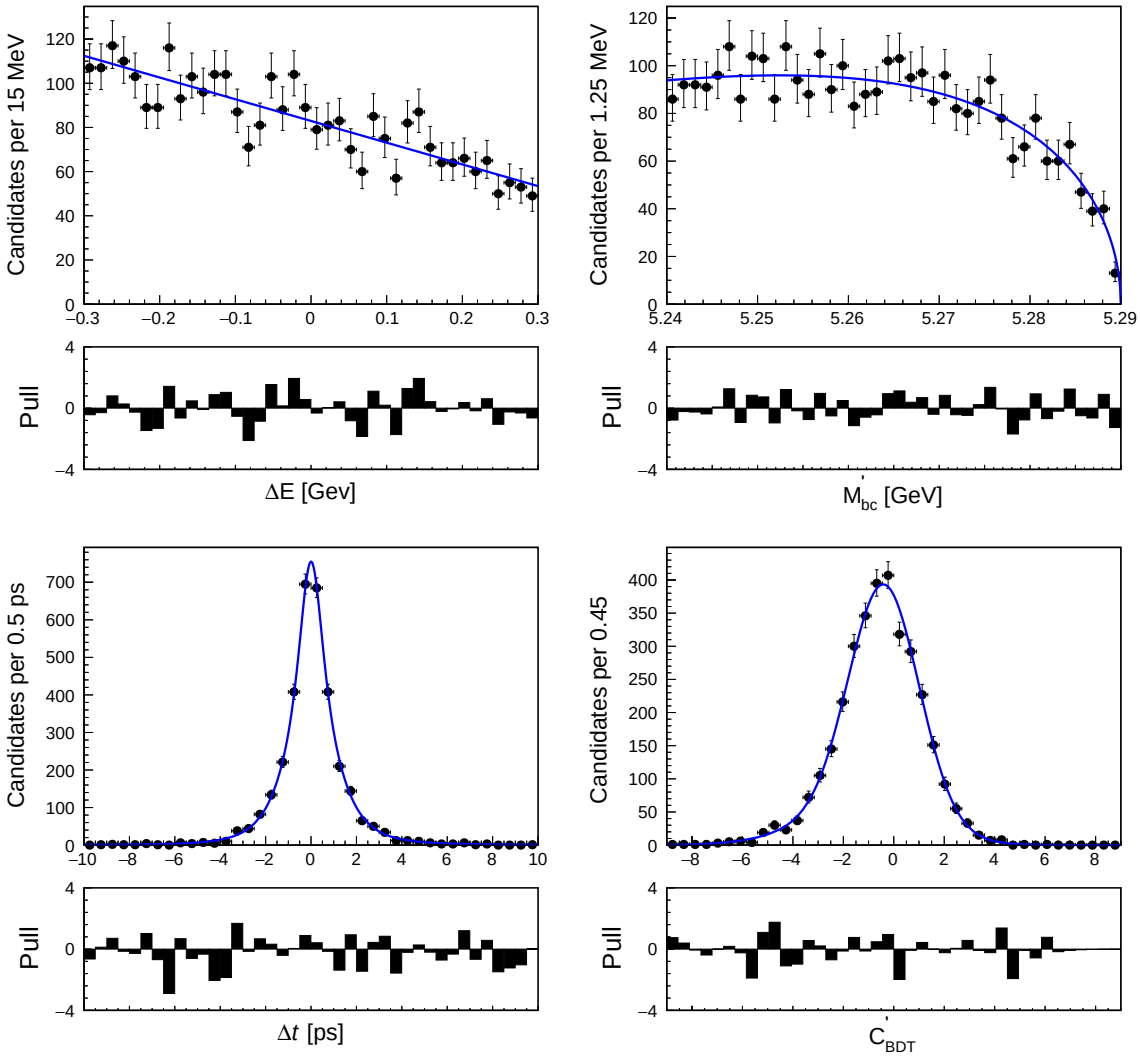

Figure 6.12: 4D fit projections for integrated $q \cdot r$ bin in continuum simulation events.

Chapter 7

Fitter check

7.1 Ensemble toy experiment

We perform 1000 4D ensemble toy experiments, in which the signal and $B\bar{B}$ components are sampled from their simulation samples. However, the continuum components is generated using its PDF shapes, as we have limited statistics available for the $1\,\mathrm{ab}^{-1}$ generic sample. Subsequently, these data sets are fitted using the corresponding PDFs to examine whether there is any bias inherent in the fitter or not. For each test, we calculate the pull for various fit parameters, which is defined as follows:

$$\text{Pull} = \frac{\text{Fitted value} - \text{Expected value}}{\text{Fitted uncertainty}} \tag{7.1}$$

In the absence of bias, we expect the pull to follow a Gaussian distribution with a mean of zero and a standard deviation of one for all the floated parameters. The fit details are described in Table 7.1. We observe no significant bias in the fitter during the ensemble toy experiment. All the fitted values are consistent with their expected values. The ensemble toy experiment plots are shown in Figs. 7.1 and 7.2, and the results are summarized in Table 7.2.

Table 7.1: Fitter details of the 7 $q \cdot r$ bin simultaneous fit.

Components	Fit observables
Signal	PDF shapes are fixed to the values determined from a $q \cdot r$ binned signal MC fit. Floating parameters are signal yield, C, and S.
$B\overline{B}$	PDF shapes are fixed to the simulation values determined from integrated $q \cdot r$ bin. $B\overline{B}$ background yield is floated.
$q\overline{q}$	PDF shapes are set to the values obtained from sideband data and the floating parameter are $q\overline{q}$ yield, ARGUS curvature, and ΔE slope.

Table 7.2: Ensemble toy experiment results using 361.5 fb^{-1} simulation events.

Parameter	Pull mean	Pull width	Fit value with uncertainty	Expected
Signal yield	-0.06 ± 0.03	1.02 ± 0.02	389 ± 24	390
Continuum yield	-0.03 ± 0.03	1.00 ± 0.02	4210 ± 68	4112
$B\overline{B}$ yield	-0.04 ± 0.03	1.02 ± 0.02	142 ± 23	142
C	0.01 ± 0.03	1.06 ± 0.02	-0.003 ± 0.152	0.0
S	0.10 ± 0.03	0.98 ± 0.02	0.714 ± 0.237	0.703

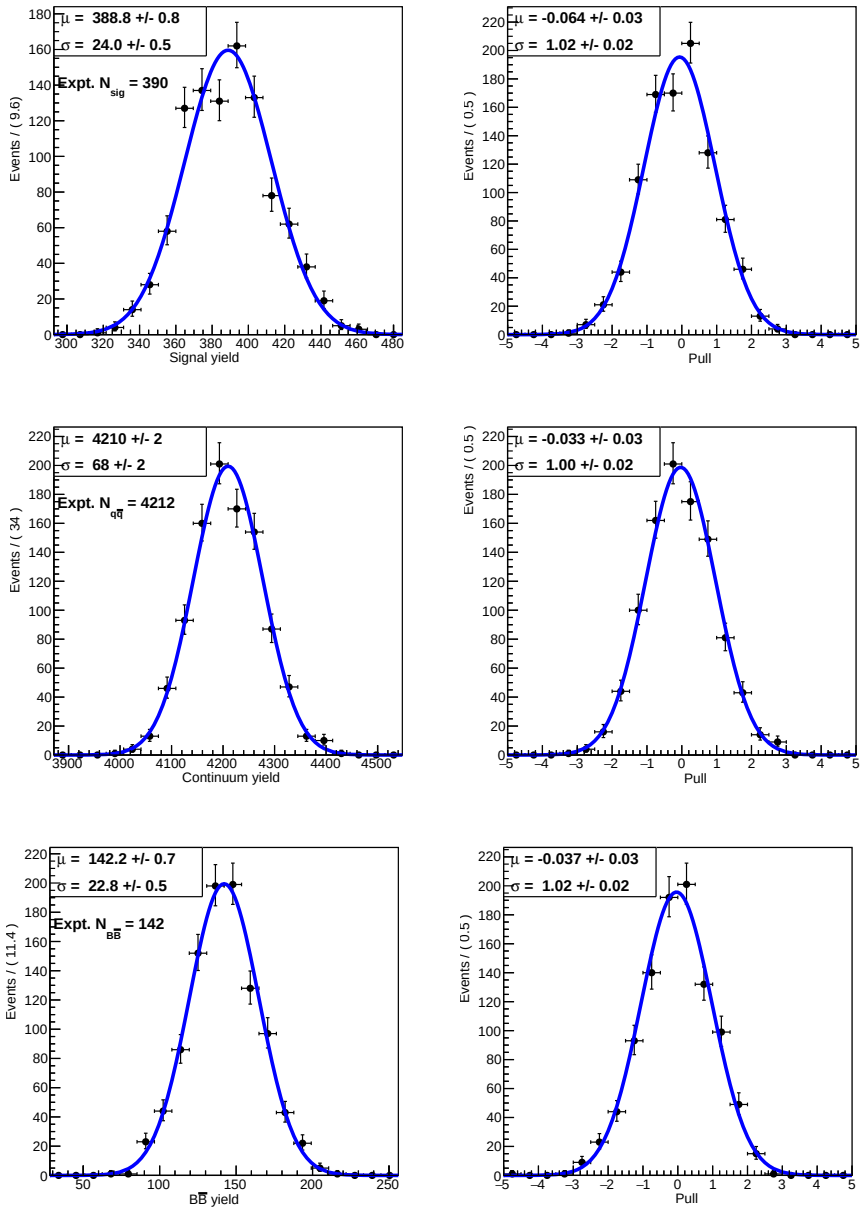

Figure 7.1: Various event yields and corresponding pull distributions.

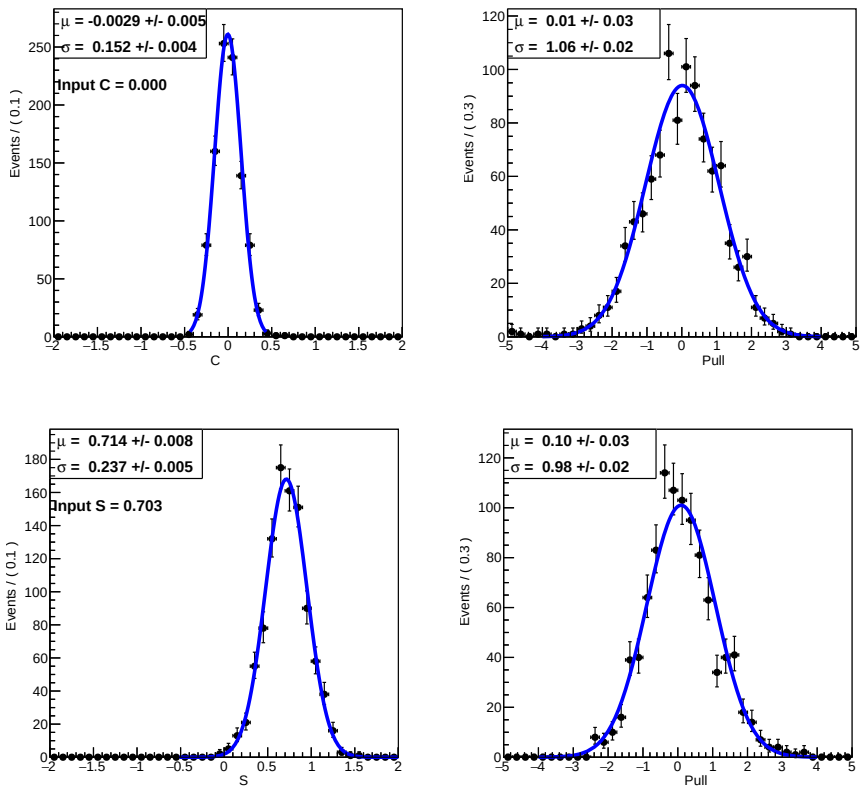

Figure 7.2: C, S, and corresponding pull distributions.

7.2 Linearity test

To assess the stability of the fitter, we test it with different values of *CP* asymmetry parameters C and S. A simulation sample is generated with $C = 0.0$ and four different values of S, namely S =0.5, 0.6, 0.7, and 0.8. We also generate another set of simulation samples, this time with $S = 0.7$ while varying the values of C; the four values chosen are $C = 0.2$, 0.1, 0.0, and -0.1. The average fit results from the 1000 toy tests are subjected to the fitting with a linear function. The linearity test results are shown in Fig. 7.3. No significant bias is visible as expected.

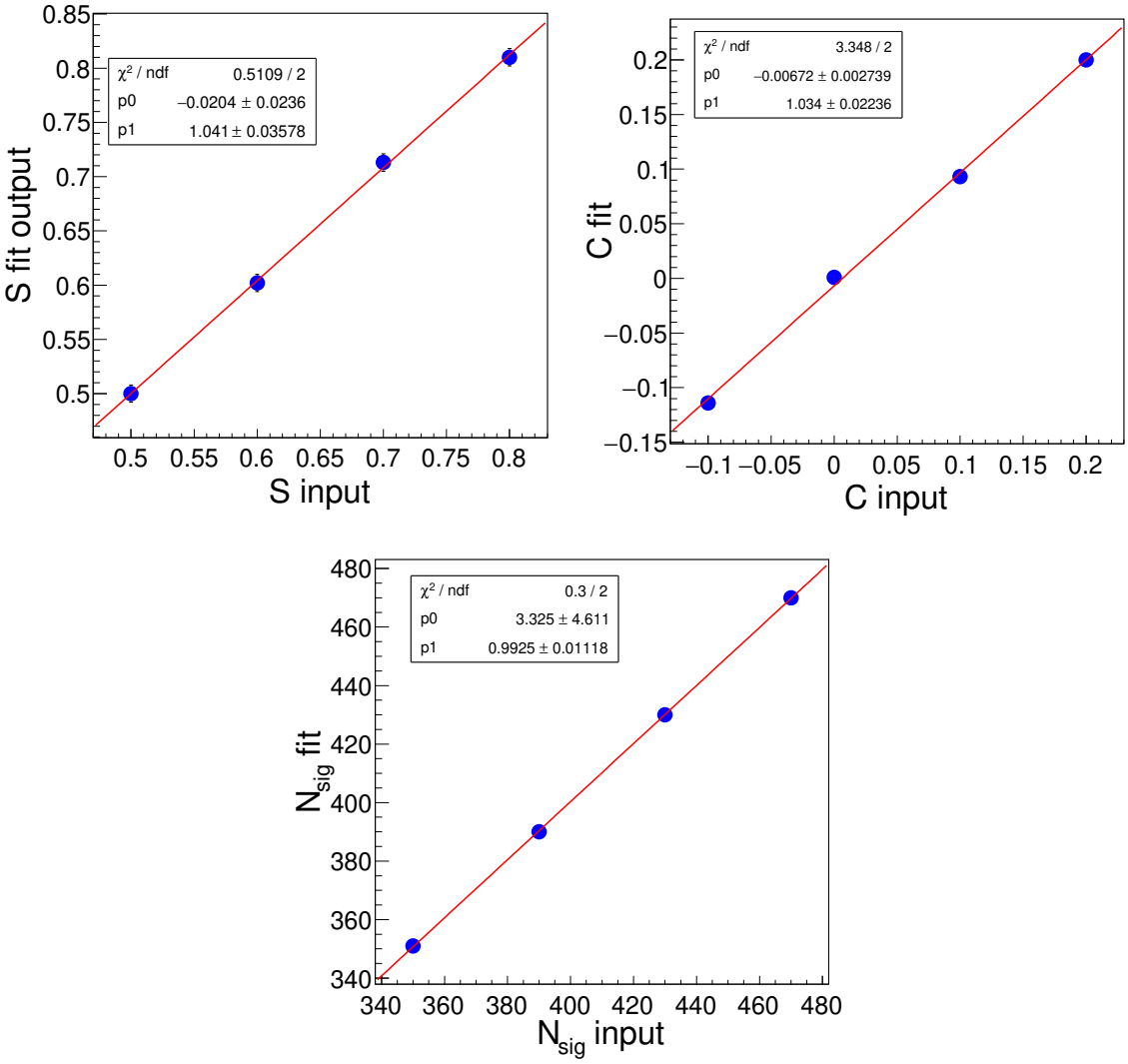

Figure 7.3: Results of the linearity test for S, C, and signal yield.

7.3 Liklihood profile

Figure 7.4 shows the likelihood profile for C, S, and signal yield for an ensemble toy experiment. The profile of the negative log-likelihood also validate that the *CP* asymmetry and signal

yield agree with the expected values that maximize the likelihood function.

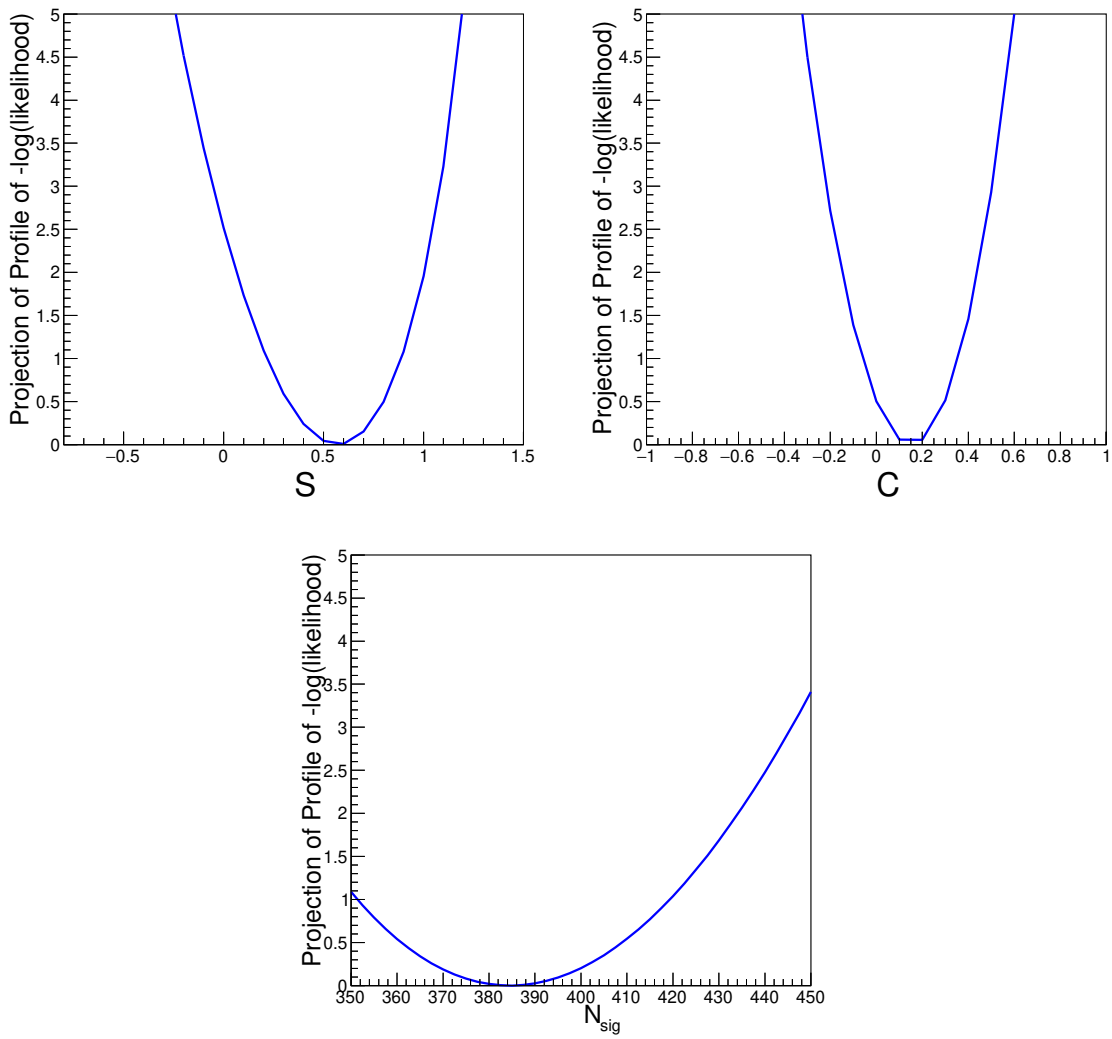

Figure 7.4: Results of the likelihood profile for S, C, and signal yield.

Chapter 8

Study of $B^+ \to \bar{D}^0(\to K_S^0\pi^0)\pi^+$ control sample

8.1 Introduction and fit strategy

We study the $B^+ \to \bar{D}^0(\to K_S^0\pi^0)\pi^+$ control sample to investigate potential data-simulation differences in various signal PDF shape parameters as well as to assess the efficiency correction resulting due to the selection criterion applied on the BDT output. The K_S^0, π^0, and BDT selections are kept identical to those used for our signal mode. To ensure a similar π^0 momentum range with the signal channel, we require a minimum π^0 momentum of 1.5 GeV. The remaining selections are listed in Table 8.1. We use the highest p-value of the vertex-fit χ^2 to select the best candidate. To extract the signal, we perform a 3D unbinned maximum-liklihood fit to ΔE, $M'_{\rm bc}$, and $C'_{\rm BDT}$. Various components of the fit and PDFs used to model them are similar to the signal mode as listed in Table 8.2. Due to the absence of flavor oscillations for charged B mesons, the time-dependent analysis is not commonly conducted. Thus, we exclude the Δt distribution in this fitter.

8.2 Fit result and correction factors

The fit projections are shown in Figs. 8.1 and 8.2. We calculate the data-simulation correction factors, as listed in Table 8.3, which are applied as corrections to the ΔE, $M'_{\rm bc}$, and $C'_{\rm BDT}$ PDF shapes while fitting to the $B \to K_S^0\pi^0$ data. The offset is denoted as the correction for the mean value, while the scaling factor is indicated as the correction for the width value.

Table 8.1: Summary of selections applied on $B \to D\pi$ final-state particles.

π selection	$\lvert dz \rvert < 2.0$ cm $dr < 0.5$ cm nCDCHits > 20 Binary pionID > 0.5
π^0 selection	$116 < M_{\gamma\gamma} < 150$ MeV $\lvert \cos\theta_{\rm hel} \rvert < 0.972$ E_γ (endcap) > 153 MeV E_γ (barrel) > 35 MeV
$K^0_{\rm S}$ selection	$489 < M_{\pi^+\pi^-} < 507$ MeV
D selection	$1.82 < M_D < 1.90$ GeV
B selection	$5.25 < M'_{\rm bc} < 5.29$ GeV $-0.2 < \Delta E < 0.3$ GeV

Table 8.2: PDFs used to model ΔE, $M'_{\rm bc}$ and $C'_{\rm out}$ for $B^+ \to \bar{D}^0\pi^+$. G, AG, CB, KDE, A, Poly1, and Poly3 denote Gaussian, asymmetric Gaussian, Crystal Ball, Kernel density estimation, ARGUS, first, and third-order polynomial, respectively.

Component	ΔE	$M'_{\rm bc}$	$C'_{\rm out}$
Signal	CB+G	2G	AG+G+G
Self cross-feed	AG + Poly1	A+G	AG+G+G
Generic B	KDE	KDE	AG+G
Continuum	Poly3	A	AG+G+G

Table 8.3: Data-MC correction factors determined with the $B^+ \to \bar{D}^0\pi^+$ control mode.

Parameter	Data	MC	Correction factor
ΔE mean (GeV)	-0.0185 ± 0.0017	-0.0163 ± 0.0015	-0.0022 ± 0.0023
ΔE width (GeV)	0.0327 ± 0.0013	0.0336 ± 0.0013	0.9732 ± 0.0540
$M'_{\rm bc}$ mean (GeV)	5.2790 ± 0.0001	5.2792 ± 0.0001	-0.0002 ± 0.0001
$M'_{\rm bc}$ width (GeV)	0.0101 ± 0.0003	0.0098 ± 0.0003	1.0306 ± 0.0440
$C'_{\rm out}$ mean	1.6470 ± 0.0731	1.6591 ± 0.0612	-0.0121 ± 0.0953
$C'_{\rm out}$ width	1.6793 ± 0.0593	1.5694 ± 0.0482	1.0700 ± 0.0501

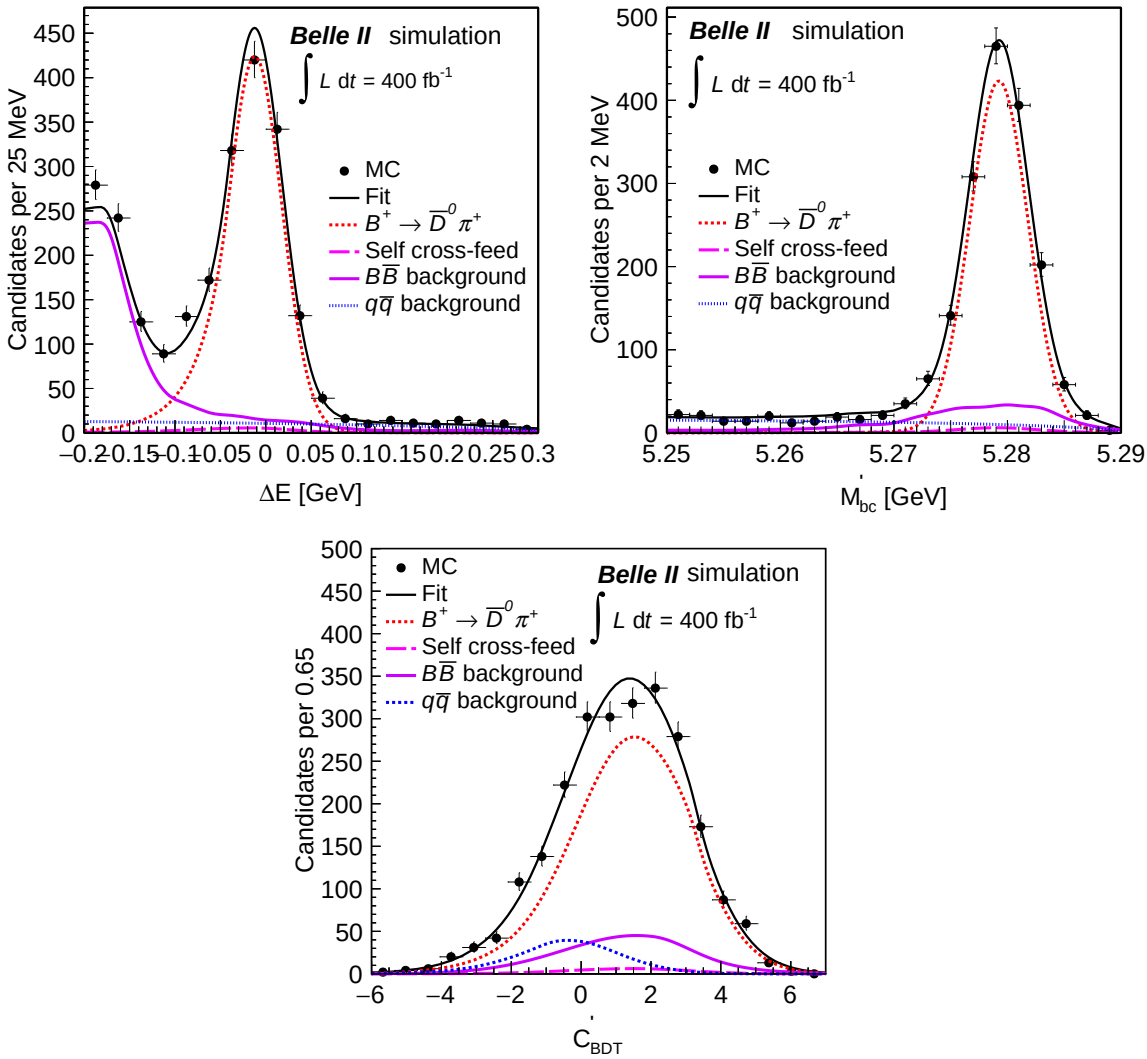

Figure 8.1: 3D fit projections for the $B^+ \to \overline{D}^0\pi^+$ simulation sample.

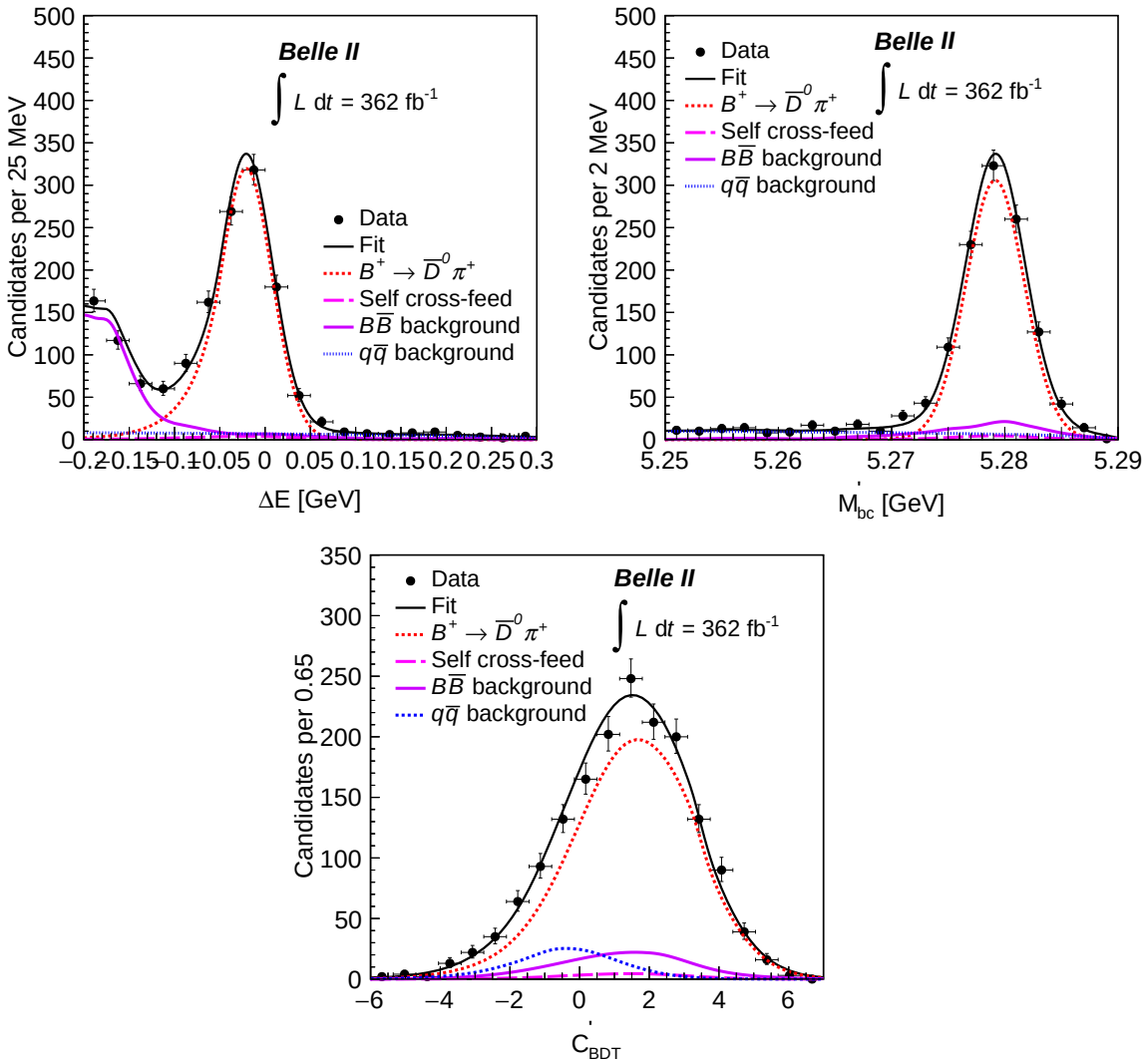

Figure 8.2: 3D fit projections for the $B^+ \to \overline{D}^0\pi^+$ data sample.

Chapter 9

Study of $B^0 \to J/\psi(\mu^+\mu^-)K^0_S$ control sample

9.1 Introduction and fit strategy

We perform a comprehensive analysis of the well-established $B^0 \to J/\psi K^0_S$ decay to validate our time-dependent fit framework. This decay mode is significantly cleaner and possesses higher statistics compared to the signal mode, facilitating a more robust assessment of our fitting methodology. To mimic the signal decay, we do not use information from the two muon tracks to reconstruct the signal B decay-vertex. We first establish the analysis framework using simulation, following the same approach as for the signal mode. Then we apply this framework to examine the collision data. The selection criteria for K^0_S are exactly the same as those used in the signal mode. We closely follow the selection and fitting strategy employed in the $\sin 2\phi_1$ measurement paper [74]. The remaining selections are listed in Table 9.1. As $B^0 \to J/\psi K^0_S$ is a very clean decay, we do not perform a dedicated BDT-based continuum suppression, in contrast to what was done for the signal mode. We apply a simpler criterion $R_2 < 0.4$ to suppress the continuum background. For simplicity, we have also chosen not to incorporate the ΔE distribution in the fitter. The selection criteria for signal, tag-side vertexing, and flavor tagging binning parameters remain the same as those used in the signal mode. The PDF shapes used for $M_{\rm bc}$ and Δt are also identical to those used in the signal mode. The $B\overline{B}$ background is modeled in $M_{\rm bc}$ using a sum of a Crystal Ball and a Gaussian function. We find that approximately 3% of $B\bar{B}$ events peak in the $M_{\rm bc}$ signal region; dominant contribution in $B\overline{B}$ peaking background

comes from $B^0 \to \eta_c(\pi^+\pi^-)K^0_S$ and $B^0 \to J/\psi K^{*0}(K^0_S\pi^0)$ decays [74]. The 2D fit projections for the sixth $q \cdot r$ bin in signal, $B\overline{B}$, and $q\overline{q}$ simulation events are shown in Figs. 9.1, 9.2, and 9.3.

Table 9.1: Summary of selections applied on $B^0 \to J/\psi K^0_S$ final-state particles.

μ selection	$\lvert dz\rvert < 3.0$ cm $dr < 0.5$ cm muonID > 0.2
J/ψ selection	$3.00 < M < 3.15$ GeV
K^0_S selection	$489 < M_{\pi^+\pi^-} < 507$ MeV
B selection	$5.2 < M_{\rm bc} < 5.3$ GeV $\lvert\Delta E\rvert < 0.05$ GeV

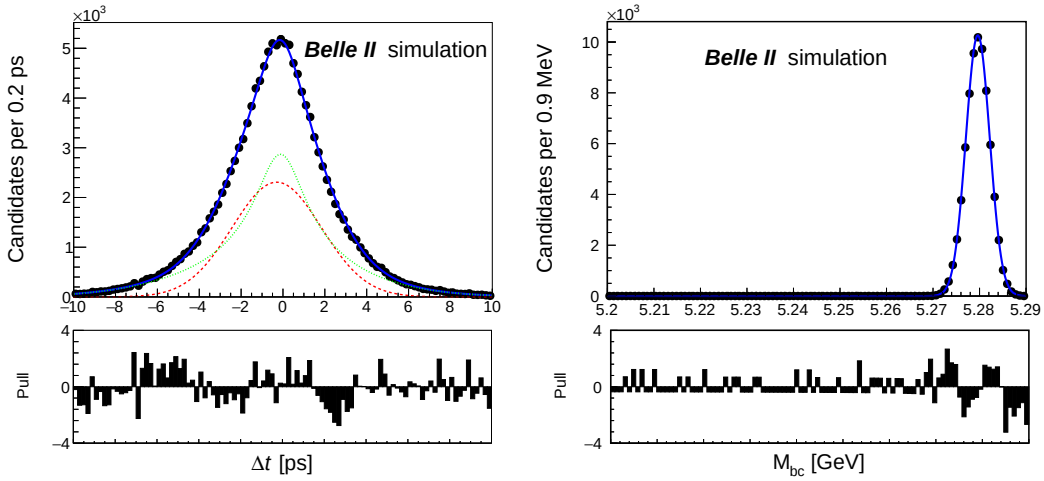

Figure 9.1: Example 2D fit projections for the sixth $q \cdot r$ bin in signal simulation events.

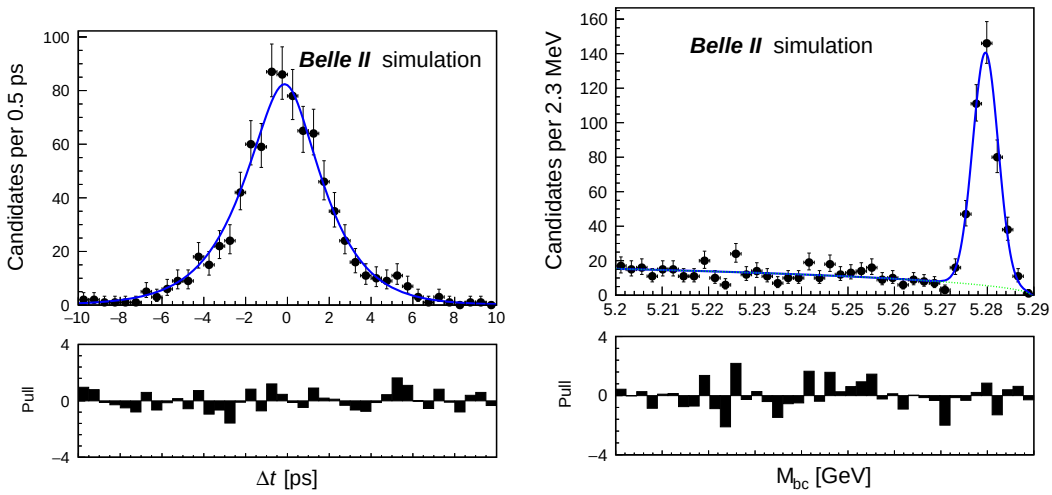

Figure 9.2: 2D fit projections for the integrated $q \cdot r$ bin in $B\overline{B}$ simulation events.

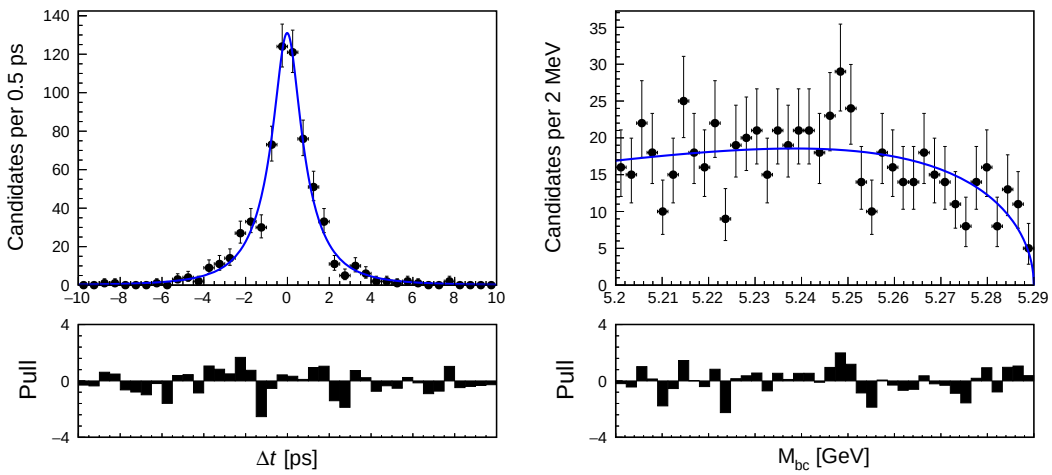

Figure 9.3: 2D fit projections for the integrated $q \cdot r$ bin in continuum simulation events.

9.2 B lifetime measurement

We perform a flavor-integrated fit for the B^0 lifetime measurement. For the flavor integrated case, the time-dependent signal PDF described in Eq. 6.3 becomes

$$P_{\text{sig}}(\Delta t, q) = \frac{\mathrm{e}^{-|\Delta t|/\tau_{B^0}}}{2\tau_{B^0}} \otimes R_{\text{sig}}. \tag{9.1}$$

The shape of the remaining PDFs is described in the previous section. We perform a 2D ($M_{\text{bc}} - \Delta t$) unbinned extended maximum-likelihood fit with the likelihood function:

$$\mathcal{L} = \frac{e^{-\sum_j n_j}}{N!} \prod_i^N \left[\sum_j n_j \mathcal{P}_j^i \right], \tag{9.2}$$

where N is the total number of events, n_j is the yield of event category j, and $\mathcal{P}_j^i$ is the PDF of the same category for event i. To validate the resolution function, a lifetime fit is performed on the reconstructed Δt distribution in both the data and simulation samples. The fit results are summarised in Tables 9.2 and 9.3, and the fit projections are shown in Figs. 9.4 and 9.5 for simulation and data, respectively.

Table 9.2: Lifetime fit results in the 400 fb^{-1} simulation sample.

Parameter	Fitted value	Expected value
Signal yield	2134^{+49}_{-48}	2128
Continuum yield	649^{+29}_{-28}	656
$B\overline{B}$ yield	106 ± 7	106
Lifetime (ps)	1.47 ± 0.05	1.52

Table 9.3: Lifetime fit results in the 361.5 fb^{-1} data sample.

Parameter	Fitted value
Signal yield	1958^{+47}_{-46}
Continuum yield	464^{+26}_{-25}
$B\overline{B}$ yield	94 ± 5
Lifetime (ps)	1.46 ± 0.05

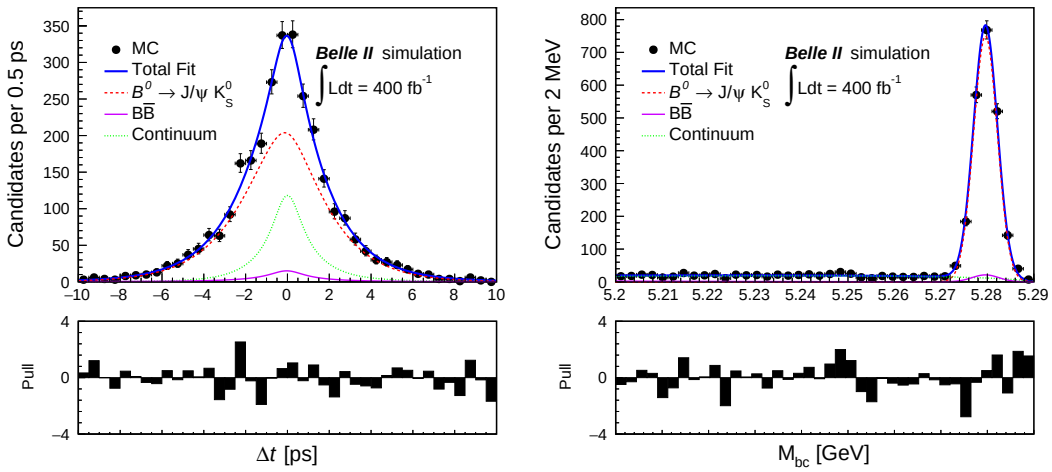

Figure 9.4: Lifetime fit projections in the 400 fb^{-1} simulation sample.

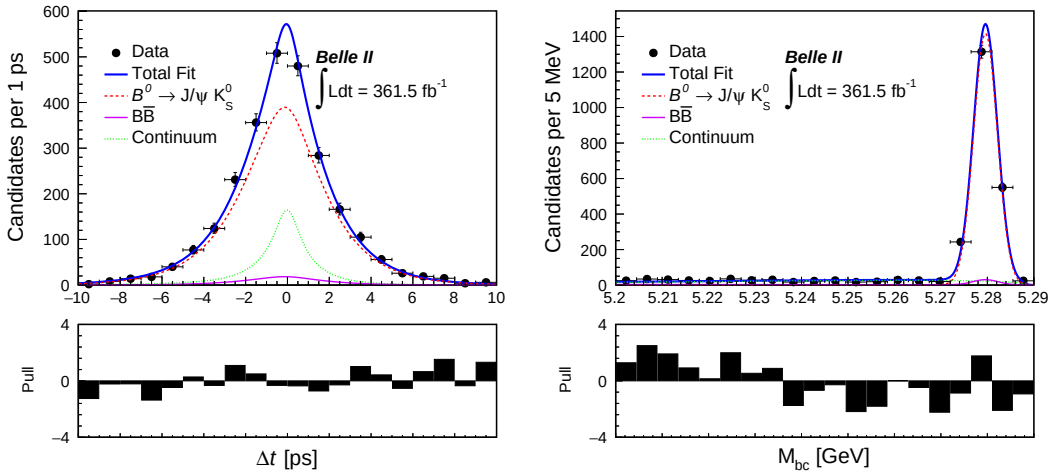

Figure 9.5: Lifetime fit projections in the 361.5 fb^{-1} data sample.

9.3 C and S determination

We perform a comprehensive time-dependent CP violation fit to a data sample corresponding to 189.8 fb^{-1} and determine the values of C and S. Figure 9.6 shows the two projections of the fit to the seven $q \cdot r$-integrated data samples that include both B^0 and $\bar{B}^0$ candidates. The fit results are summarized in Table 9.4. We find the results to be consistent with known values [29]. Therefore, we validate the analysis framework using the control sample.

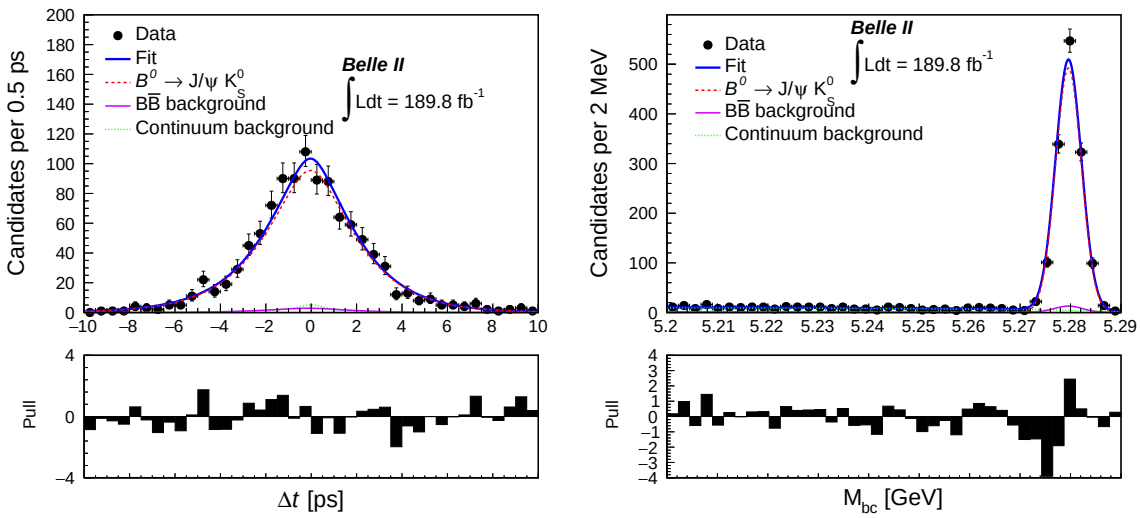

Figure 9.6: Fit projections of Δt (left) and M_{bc} (right) for CP fit in the 189.8 fb^{-1} data sample.

Table 9.4: CP fit results in the 189.8 fb^{-1} data sample.

Parameter	Fitted value
Signal yield	1391^{+39}_{-38}
Continuum yield	280^{+19}_{-18}
$B\bar{B}$ yield	77 ± 6
C	-0.10 ± 0.07
S	$+0.76 \pm 0.12$

9.4 Correction factors

We assess potential differences between data and simulation in the Δt distribution. Table 9.5 provides the correction factors that will be applied to the Δt shapes while fitting to the $B^0 \to K^0_S \pi^0$ data sample. The offset is quoted as the correction for the mean and the scaling factor as the correction for the width.

Table 9.5: Data-simulation correction factors of the Δt PDF.

Parameter	Data	MC	Correction factor
Δt mean (ps)	-0.1861 ± 0.0635	-0.1311 ± 0.0633	-0.055 ± 0.0897
Δt width (ps)	1.3355 ± 0.0657	1.3743 ± 0.0683	0.9718 ± 0.0680

Chapter 10

Fit results

10.1 Fit to simulation

A simultaneous fit is carried out on the two subsamples described in Section 6.1, with seven r bins in the simulation sample. Figure 10.1 shows the four projections of the result of the fit applied to the seven $q \cdot r$-integrated simulated samples, including both B^0 and $\bar{B}^0$ candidates in a 1ab^{-1} dataset. For each projection, the signal enhancing criteria, $5.27 < M'_{\text{bc}} < 5.29\,\text{GeV}$, $-0.15 < \Delta E < 0.10\,\text{GeV}$, $|\Delta t| < 10.0\,\text{ps}$, and $C'_{\text{out}} > 0.0$, are applied on all except for the variable displayed. The results of the fit performed on the $1\,\text{ab}^{-1}$ generic simulation sample are summarized in Table 10.1. The results agree with their expected values. Table 10.2 provides the correlation among fit parameters.

Table 10.1: Parameters determined from *CP* fit in the $1\,\text{ab}^{-1}$ generic simulation sample.

Parameters	Fit value	True value
N_{sig}	1041^{+42}_{-41}	1010
$N_{B\bar{B}}$	324^{+38}_{-37}	326
$N_{q\bar{q}}$	13467^{+124}_{-123}	13535
C	-0.02 ± 0.10	0.0
S	0.07 ± 0.16	0.0
ΔE slope	-1.076 ± 0.05	–
M'_{bc} ARG. curv.	$-29.3^{+18.4}_{-18.3}$	–

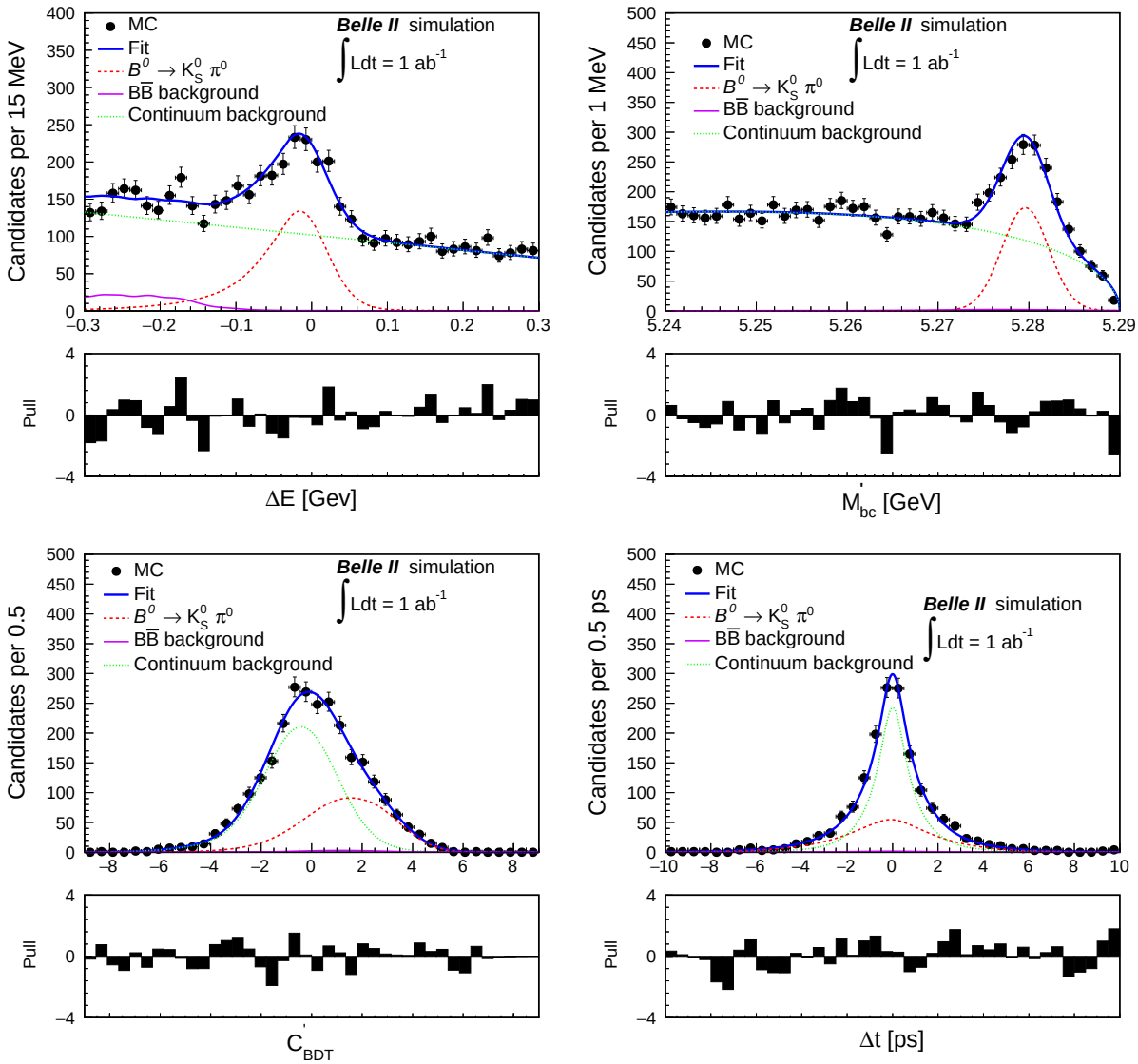

Figure 10.1: Signal enhanced *CP* fit projections of ΔE (upper-left), M'_{bc} (upper-right), C'_{out} (lower-left), and Δt (lower-right) shown for the 1 ab^{-1} simulated sample integrated in the seven $q \cdot r$ bins.

Table 10.2: Correlation among fit parameters.

Parameter	$N_{B\overline{B}}$	$N_{q\overline{q}}$	$N_{\rm sig}$	ΔE slope	$M'_{\rm bc}$ ARG. par.	C	S
$N_{B\overline{B}}$	1.000	0.217	0.073	-0.208	-0.149	+0.027	-0.016
$N_{q\overline{q}}$	0.217	1.000	-0.091	-0.064	-0.085	0.019	-0.002
$N_{\rm sig}$	0.073	-0.091	1.000	0.010	0.127	0.043	-0.011
ΔE slope	-0.208	-0.064	0.010	1.000	0.049	0.007	0.003
$M'_{\rm bc}$ ARG. par.	-0.149	-0.085	0.127	0.049	1.000	0.018	-0.001
C	+0.027	0.019	0.043	0.007	0.018	1.000	-0.017
S	-0.016	-0.002	-0.011	0.003	-0.001	-0.017	1.000

10.2 Fit to data

10.2.1 B^0 lifetime fit

We employ the strategy outlined in section 9.2 for the lifetime fit, using only TD events categorized for the lifetime fit. The projection of the signal-enhanced lifetime fit is presented in Figure 10.2, and the corresponding results are listed in Table 10.3. The obtained B^0 lifetime is consistent with the known value [29].

Table 10.3: Parameters determined from B^0 lifetime fit in 362 fb^{-1} Data sample.

Parameter	Fit value	known value
τ_{B^0}	$1.504^{+0.156}_{-0.141}$	1.519 ± 0.004

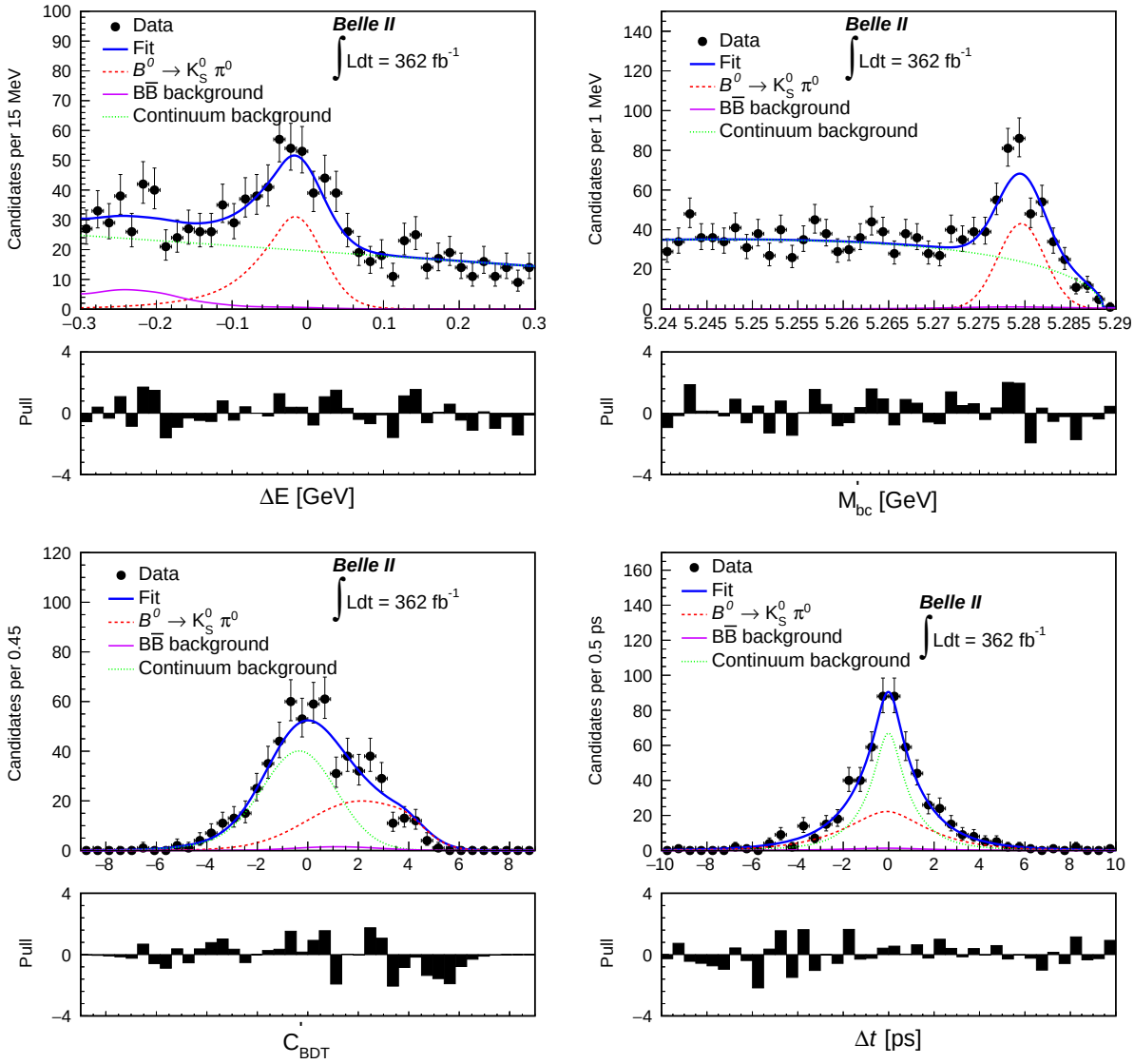

Figure 10.2: Signal enhanced B^0 lifetime fit projections of ΔE (upper-left), M'_{bc} (upper-right), C'_{out} (lower-left), and Δt (lower-right) shown for the data sample flavor integrated in $362\,\mathrm{fb}^{-1}$.

10.2.2 *CP* asymmetry and $\mathcal{B}$ fit

A simultaneous fit is carried out on the two subsamples described in Section 6.1, with seven r bins in the data sample. Figure 10.3 shows the $M'_{\rm bc}$, ΔE, $C'_{\rm BDT}$, and Δt distributions in the data along with the fit projections overlaid. For these plots, the seven r bins have been combined. In addition, for each plot the signal-enhancing criteria $5.27 < M'_{\rm bc} < 5.29\,\text{GeV}$, $-0.15 < \Delta E < 0.10\,\text{GeV}$, $|\Delta t| < 10.0$ ps, and $C'_{\rm BDT} > 0.0$ have been applied except for the variable displayed. The resulting signal yield $N_{\rm sig}$, C, and S are 415^{+26}_{-25}, $-0.04^{+0.14}_{-0.15}$, and $0.75^{+0.20}_{-0.23}$, respectively. The correlation coefficient between two asymmetries is -0.17%. From the signal yield, we determine the branching fraction as $\mathcal{B}(B^0 \to K^0_{\rm S}\pi^0) = N_{\rm sig}/(2N_{B\overline{B}}f^{+0}\varepsilon_{\rm rec}) = (11.15^{+0.69}_{-0.67}) \times 10^{-6}$, which is consistent with the world average [29]. Here, $N_{B\overline{B}}$ is the number of produced $B\bar{B}$ events, f^{+0} is the fraction of $B^0\overline{B}^0$ or B^+B^- production at the $\Upsilon(4S)$ resonance [75], $\varepsilon_{\rm rec}$ is the signal efficiency, and all quoted uncertainties are statistical. Figure10.4 shows the projection of the fit results onto Δt, separately for tagged B^0 and $\overline{B}^0$ candidates, after subtracting background with the ${}_s\mathcal{P}$lot method [78].

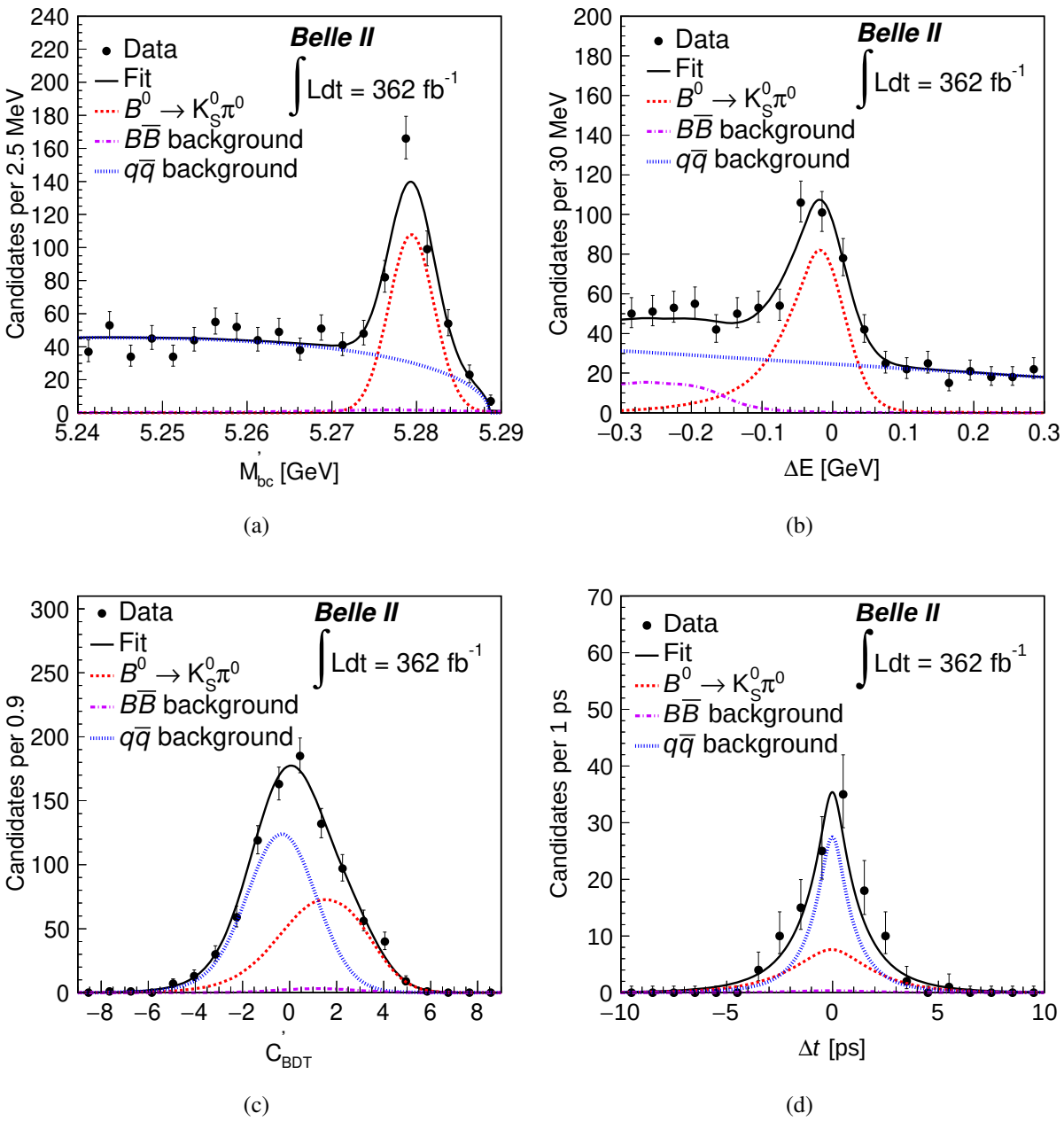

Figure 10.3: Distributions of (a) M'_{bc}, (b) ΔE, (c) C'_{BDT}, and (d) Δt with fit projections overlaid for both B^0 and $\overline{B}^0$ candidates satisfying the criteria $5.27 < M'_{\mathrm{bc}} < 5.29\,\mathrm{GeV}$, $-0.15 < \Delta E < 0.10\,\mathrm{GeV}$, $|\Delta t| < 10.0\,\mathrm{ps}$, and $C'_{\mathrm{BDT}} > 0.0$ (except for the variable displayed). The solid curves represent the fit projection, while various fit components are explained in the legends.

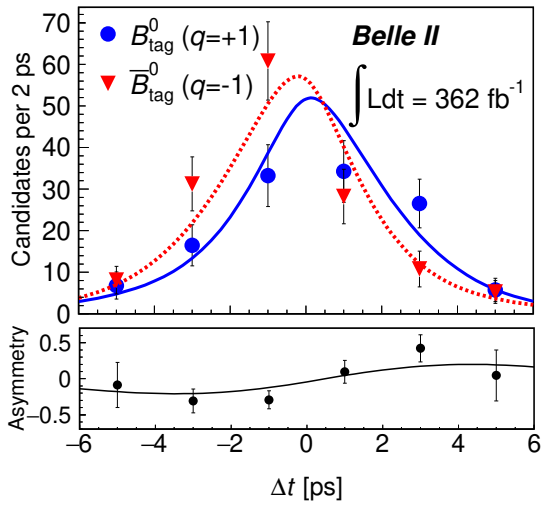

Figure 10.4: Projection of the fit results onto Δt separately for tagged B^0 and $\bar{B}^0$ candidates after subtracting background with the ${}_s\mathcal{P}$lot method [78]; the asymmetry, defined as $[N(B^0_{\text{tag}}) - N(\bar{B}^0_{\text{tag}})]/[N(B^0_{\text{tag}}) + N(\bar{B}^0_{\text{tag}})]$, is displayed underneath, along with the projection of the fit result.

Chapter 11

Systematic uncertainties and summary

11.1 Systematic uncertainties in $\mathcal{B}$

Tracking efficiency

As described in Ref. [79], we linearly add an uncertainty of 0.24% for each of the two pion tracks originating from the K_S^0 decay in the signal side.

K_S^0 reconstruction efficiency

The $D^{*+} \to D^0(\to K_S^0\pi^+\pi^-)\pi^+$ and $D^{*+} \to D^0(\to K_S^0\pi^0)\pi^+$ decays are used to calculate the K_S^0 reconstruction efficiency in bins of the K_S^0 flight distance and cosine of the polar angle. The ratio of the K_S^0 reconstruction efficiency between data and simulation is found to be $94.3 \pm 2.0\%$. The uncertainty on this ratio is assigned as a systematic uncertainty.

Continuum Suppression Efficiency

Since we suppress the continuum background using a selection on the BDT output, we investigate possible difference between data and simulation in efficiency using $B^+ \to \overline{D}^0(\to K_S^0\pi^0)\pi^+$ channel with $361.5\,\mathrm{fb}^{-1}$ data sample. We obtain the selection efficiency by performing a 2D (ΔE-M'_{bc}) fit simultaneously to two disjoint samples: the first one is composed of the candidates that pass the continuum suppression criterion (BDT > 0.6) and the second one is composed of the candidates that fail the selection. We then estimate the data-simulation correction factor and possible systematic uncertainty. The simultaneous fit results are shown in Figs. 11.1 and 11.2. The correction factor $\varepsilon_{\mathrm{BDT}}^{\mathrm{data/simu}}$ is calculated from the ratio of signal events ($R_{\mathrm{data/simu}}$) which is

obtained as a fit parameter.

$$R = \frac{\text{signal events pass the selection}}{\text{Total signal events (pass + fail the selection)}} \tag{11.1}$$

$$R_{\text{data}} = 0.7513 \pm 0.0139 \tag{11.2}$$

$$R_{\text{simu}} = 0.7531 \pm 0.0133 \tag{11.3}$$

$$\varepsilon_{\text{BDT}}^{\text{data/simu}} = 0.9976 \pm 0.0254 \tag{11.4}$$

The systematic uncertainty corresponding to the efficiency correction is obtained as:

$$\text{Syst}^{\text{BDT}} = 2.55\% \tag{11.5}$$

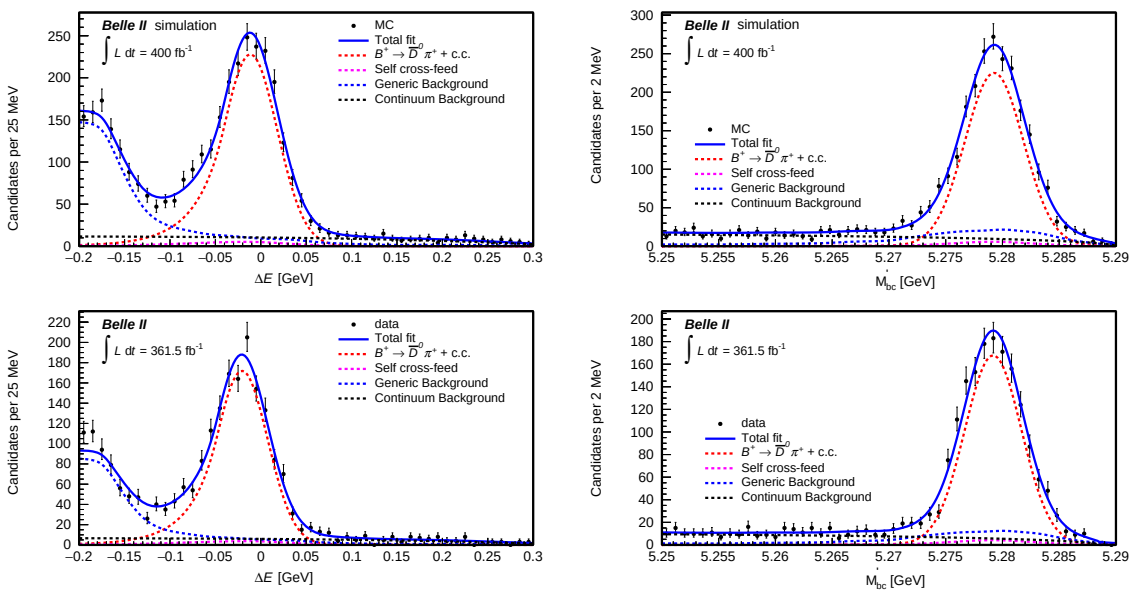

Figure 11.1: Simultaneous fit results on $B^+ \to \bar{D}^0\pi^+$ for events that pass the selection i.e., BDT> 0.6.

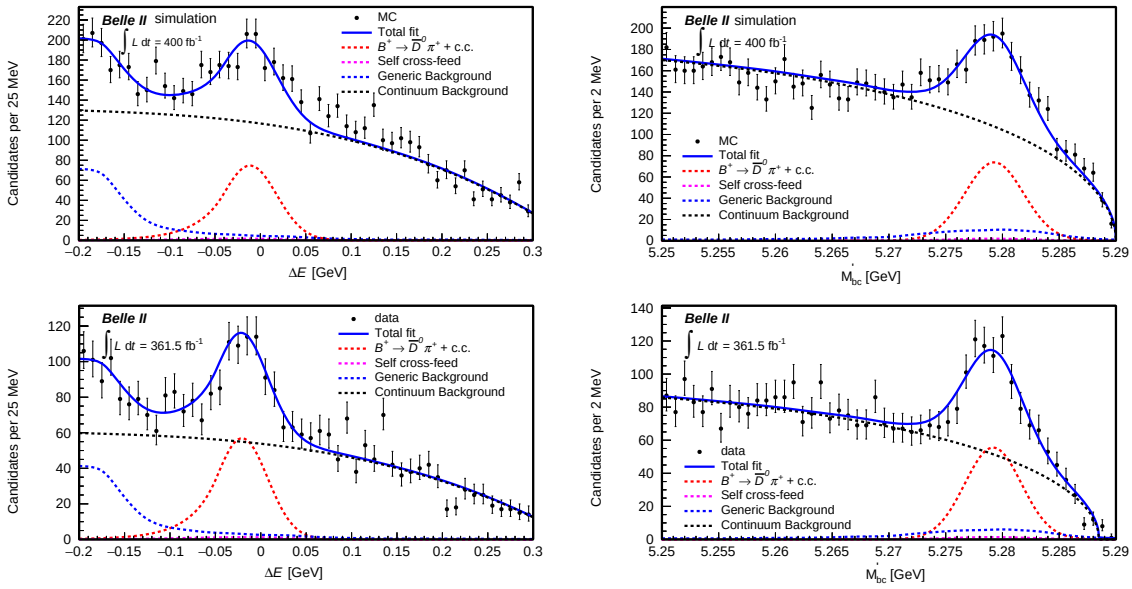

Figure 11.2: Simultaneous fit results on $B^+ \to \overline{D}^0\pi^+$ for events that fail the selection i.e., BDT < 0.6.

π^0 reconstruction efficiency

The $D^0 \to K^-\pi^+\pi^0$, $D^0 \to K^-\pi^+$ decays are used to evaluate the systematic uncertainties to π^0 reconstruction and selection efficiency. The variables ΔE and D^0 invariant mass are used to obtain yields using the known values of the decay branching fraction as input [4], which are then compared in bins of π^0 momentum and cosine of polar angle. The ratio of the π^0 reconstruction efficiency between data and simulation is found to be $99.5 \pm 4.0\%$. The uncertainty on this ratio (4%) is assigned as a systematic uncertainty.

$B\overline{B}$ pair counting

An overall uncertainty of 1.5% is taken as a systematic uncertainty on the number of $B\overline{B}$ used.

Signal modeling

The uncertainty due to signal PDF shape is estimated by varying the fixed shape parameters. We use kernel density estimation PDF of $M'_{\rm bc}$, ΔE and $C'_{\rm BDT}$ for the varied PDF shape model, and then perform 1000 pseudoexperiment fit to evaluate the difference from nominal fit results. We take this difference a systematic uncertainty.

Background modeling

The uncertainties due to background PDF shape are calculated by varying all fixed shape parameters by $\pm 1\sigma$ in data sample.

Fit bias

A potential fit bias is checked by performing an ensemble test comprising 1000 pseudoexperiments in which signal and $B\overline{B}$ events are drawn from its corresponding simulation sample and background events are generated according to their PDF shapes. We calculate the mean shift of signal yield from the input value and assign it as a systematic uncertainty.

Best candidate selection

The systematic uncertainty due to best candidate selection is evaluated by performing an alternative fit with all candidates and taking the difference with respect to the nominal value.

Physics parameters

We have fixed physics parameters τ_{B^0}, χ_d and Δm_d to the world averages in *CP* fit. Therefore, a systematic uncertainty is estimated by varying the parameters by $\pm 1\sigma$ in the data sample.

Table 11.1 summarizes systematic uncertainties for the $\mathcal{B}$ measurement. Each contribution is detailed in the following subsections.

Table 11.1: Systematic uncertainties (relative) contributing to the branching fraction.

Source	$\delta\mathcal{B}(\%)$
Tracking efficiency	0.5
K_S^0 reconstruction efficiency	2.0
π^0 reconstruction efficiency	4.0
Continuum suppression efficiency	2.5
Number of $B\overline{B}$ events	1.5
Signal modeling	0.7
Background modeling	0.2
Fit bias	0.3
Best candidate selection	0.6
Physics parameters	<0.1
Total	5.5

11.2 Systematic uncertainties in C and S

Flavor tagging

We account for the systematic uncertainty arising due to flavor tagging by independently varying the related parameters ($w_r, \Delta w_r, \Delta\varepsilon_{\text{tag},r}$) according to their respective uncertainties for each r bin, while also taking correlations into account. We consider the maximum deviations with respect to nominal results as the systematic uncertainties.

Δt resolution function

The systematic uncertainty arising due to Δt resolution function is assessed by varying each resolution parameter (including Δt mean and width correction factor listed in Table 9.5) according to their respective $\pm 1\sigma$ uncertainties in data.

$B\overline{B}$ background asymmetry

In the nominal fit, we consider the charmless B decay background to exhibit no CP symmetry. Nevertheless, it is possible that this component may have a nontrivial asymmetry. To account for this possibility, we incorporate the PDF given by

$$P_{B\overline{B}}(\Delta t, q) = \frac{e^{-|\Delta t|/\tau'_{B^0}}}{4\tau'_{B^0}}[1 + q\{S' \sin(\Delta m_d \Delta t) - C' \cos(\Delta m_d \Delta t)\}] \otimes R_{B\overline{B}} \tag{11.6}$$

We perform a series of fits with the above PDF formed by varying the C and S values from -1 to $+1$ while fixing the effective lifetime (τ'_{B^0}) value to that determined from simulation. We then calculate the deviations in signal C and S from their nominal values; the largest deviation is assigned as a systematic uncertainty.

$q\overline{q}$ background asymmetry

We perform an alternative fit to fix the CP asymmetry of the $q\bar{q}$ background obtained from sideband data. The difference between results of the nominal and alternate fits attributed as a systematic uncertainty.

Signal and background modeling

The uncertainty due to signal PDF shape is estimated using an alternative model based on kernel density estimation. Similarly, the uncertainty due to background PDF shape is calculated by varying all fixed parameters by their uncertainties and taking the maximum deviation from nominal results as the uncertainty.

Fit bias

To assess the potential fit bias, we perform an ensemble test involving 1000 simulated experiments. In each experiment, signal and $B\bar{B}$ background events are drawn from simulated samples, while $q\bar{q}$ background events are generated based on the respective PDF shapes. We then determine the mean differences between the fitted and input values of C and S and assign these differences as systematic uncertainties.

Best candidate selection

To estimate the systematic uncertainty arising due to best candidate selection, we perform an alternative fit including all candidates and measure the difference with respect to the nominal value.

Physics parameters

The uncertainties due to fixed τ_{B^0} and Δm_d values are determined by varying these physics parameters according to their uncertainties and conducting the fit again. The maximum differences found in C and S values as a result of these variations are considered as systematic uncertainties.

Tag-side interference

The tag-side interference can occur when both CKM-favored and CKM-suppressed tree amplitudes contribute to the tag-side decay [82]. The resulting impact is evaluated by assuming that all events are tagged with such hadronic decays.

VXD misalignment

The uncertainty arising due to VXD misalignment is assessed by reconstructing events under different misalignment hypotheses, following the approach described in Ref. [84].

The systematic uncertainties contributing to C and S are listed in Table 11.2.

Table 11.2: Systematic uncertainties (absolute) contributing to time-dependent CP asymmetries.

Source	δC	δS
Flavor tagging	0.013	0.011
Δt resolution function	0.014	0.022
$B\bar{B}$ background asymmetry	0.030	0.018
$q\bar{q}$ background asymmetry	0.028	< 0.001
Signal modeling	0.004	0.003
Background modeling	0.006	0.018
Fit bias	0.005	0.011
Best candidate selection	0.005	0.010
Physics parameters	< 0.001	< 0.001
Tag-side interference	0.006	0.011
VXD misalignment	0.004	0.005
Total	0.047	0.040

11.3 Summary

We determine the branching fraction ($\mathcal{B}$) and CP-violating parameters C and S in the $B^0 \to K_S^0\pi^0$ decay using a dataset of 387×10^6 $B\bar{B}$ events collected by Belle II in e^+e^- collisions at the $\Upsilon(4S)$ resonance. From a signal yield of 415^{+26}_{-25} events, we obtain:

$$\mathcal{B} = (11.15^{+0.69}_{-0.67} \pm 0.61) \times 10^{-6}, \tag{11.7}$$

$$C = -0.04^{+0.14}_{-0.15} \pm 0.05, \tag{11.8}$$

and

$$S = 0.75^{+0.20}_{-0.23} \pm 0.04, \tag{11.9}$$

where the first (second) uncertainties represent the statistical (systematic) components. This constitutes the first Belle II measurement of CP asymmetries in this decay. Our results are in agreement with previous determinations [35, 36], and we achieve a superior precision for S compared to that achieved at Belle (BABAR), despite using a data sample that is 60–80% of the size of the samples employed in those experiments. We combine the time-dependent and time-integrated [76] measurements to obtain the best sensitivity of $C = +0.01 \pm 0.12 \pm 0.04$ and $\mathcal{B} = (10.73 \pm 0.63 \pm 0.62) \times 10^{-6}$. Putting all $\mathcal{B}$ and $\mathcal{A}_{CP}$ values of the $K\pi$ system together, we obtain an overall Belle II sum-rule:

$$I_{K\pi} = -0.03 \pm 0.13(\text{stat}) \pm 0.04(\text{syst}) = -0.03 \pm 0.14,$$

which is consistent with the SM prediction having a comparable precision with world's best result (-0.13 ± 0.11) [29] even with a smaller sample. The increased acceptance of the vertex detector allowing for improved K_S^0 reconstruction as well as enhanced continuum suppression are main contributors to such competitive measurements. These results agree with the SM predictions and offer valuable constraints on non-SM physics.

Chapter 12

Low-momentum π/K identification with SVD

12.1 Data and simulation sample

This study involves a two-step process. First, we calibrate the $\mathrm{d}E/\mathrm{d}x$ using both data and simulation samples equivalent to 6.1 fb^{-1}. In the second step, we assess the performance of updated calibration payloads by comparing results with data and simulation samples corresponding to 3.7 fb^{-1}.

12.2 Analysis method

The $\mathrm{d}E/\mathrm{d}x$ method is especially useful to identify charged hadrons with momentum below their MIP values. Of particular importance is the applicability of this method for distinguishing charged pions from kaons, which is the focus of our subsequent discussion. We use the self-tagging decay $D^{*+} \to D^0(\to K^-\pi^+)\pi^+$ to develop the $\mathrm{d}E/\mathrm{d}x$ PID method. To reconstruct the D^{*+} candidate, we consider all possible combinations of three charged tracks in an event, with two of them being positively or negatively charged. One of the two same-charged tracks with lower momentum is assumed to be the 'slow pion' arising from the D^{*+} meson. The remaining two tracks of opposite charge are assumed to be the kaon and pion coming from the D^0 decay, where the second track is required to have the same charge as the slow pion. We require all selected charged tracks to have a transverse (longitudinal) impact parameter less than 0.5 cm (2.0 cm). The tracks must have at least one SVD hit and track-fit p-value greater than 10^{-5}. In order to purify the sample, we require the reconstructed D^0 mass to lie between 1.85 and

1.88 GeV, corresponding to about a $\pm 3\sigma$ window around the nominal D^0 mass [4]. To increase the event count, we do not impose any requirement on the D^* momentum in the c.m. frame, ensuring that the D^* comes from both $c\bar{c}$ continuum and B decay events. Table 12.1 summarizes the list of selection criteria used for the D^* selection. For D^* candidates satisfying the above

Table 12.1: List of selection criteria used for the D^* selection.

Sl.no.	Selection
1.	$dr < 0.5\,\text{cm}$
2.	$\lvert dz \rvert < 2.0\,\text{cm}$
3.	track-fit $\chi^2 > 10^{-5}$
4.	nSVDHits > 1
5.	$1.85 < M_{D^0} < 1.88\,\text{GeV}$
6.	$139.5 < \Delta M < 151\,\text{MeV}$
7.	$1.95 < M_{D^*} < 2.05\,\text{GeV}$

selections, we model signal and background shape in the D^*–D^0 mass difference (Δm) by a sum of two Gaussian functions with a common mean and a threshold function, respectively. The latter is given by

$$f(x) = c\,(x - m_\pi)^a\, e^{-b(x-m_\pi)}, \tag{12.1}$$

where a, b, and c are the shape parameters, and m_π is the known charged pion mass [4]. We obtain background-subtracted distributions using the *sPlot* technique [78]. Figure 12.1 shows the Δm fit results in data and MC events. As shown in Fig. 12.3, the slow pions tend to have

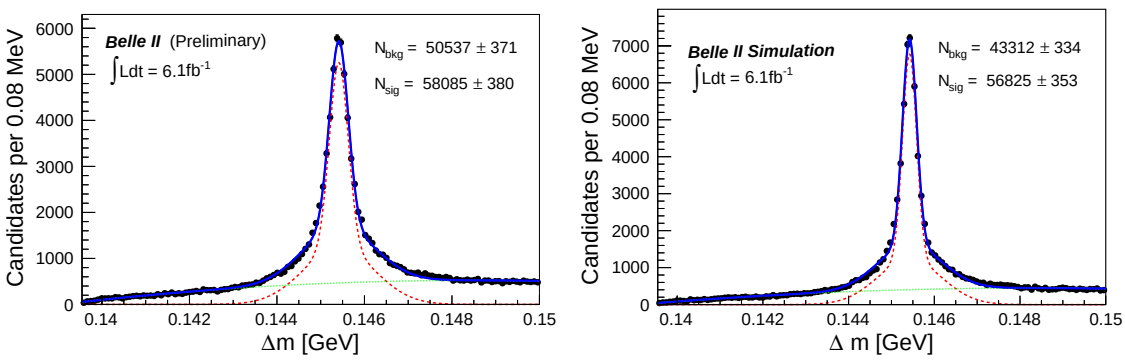

Figure 12.1: Results of the Δm fit to data (left) and MC (right) events.

a momentum below 500 MeV, while the two D^0 decay products (pions and kaons) are distributed around 1 GeV in both data and MC events. The latter pions and kaons are required

to build PDFs above 500 MeV. We validate the method by comparing the *sPlot* extracted MC signal distributions of kaon and pion momentum with the corresponding truth-matched (TM) distributions as shown in Fig. 12.2. Furthermore, a data-MC comparison of the *sPlot* signal is presented in Fig. 12.3.

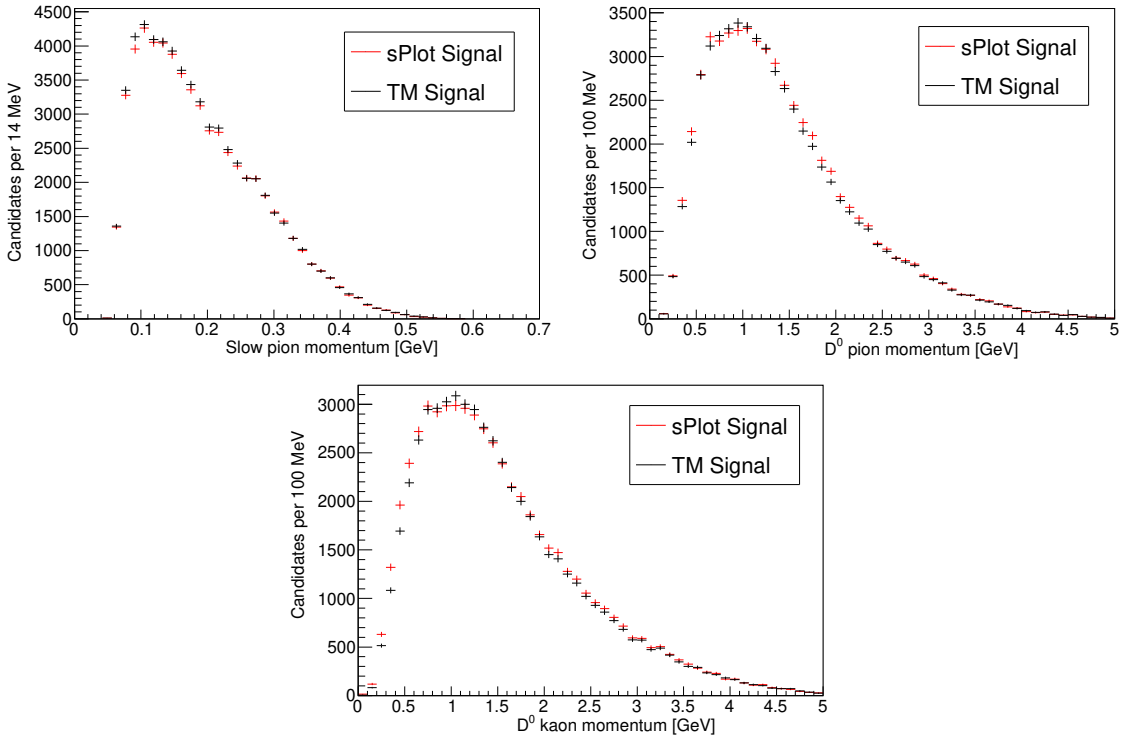

Figure 12.2: Comparison of kaon and pion momentum between the *sPlot* and truth-matched signal events.

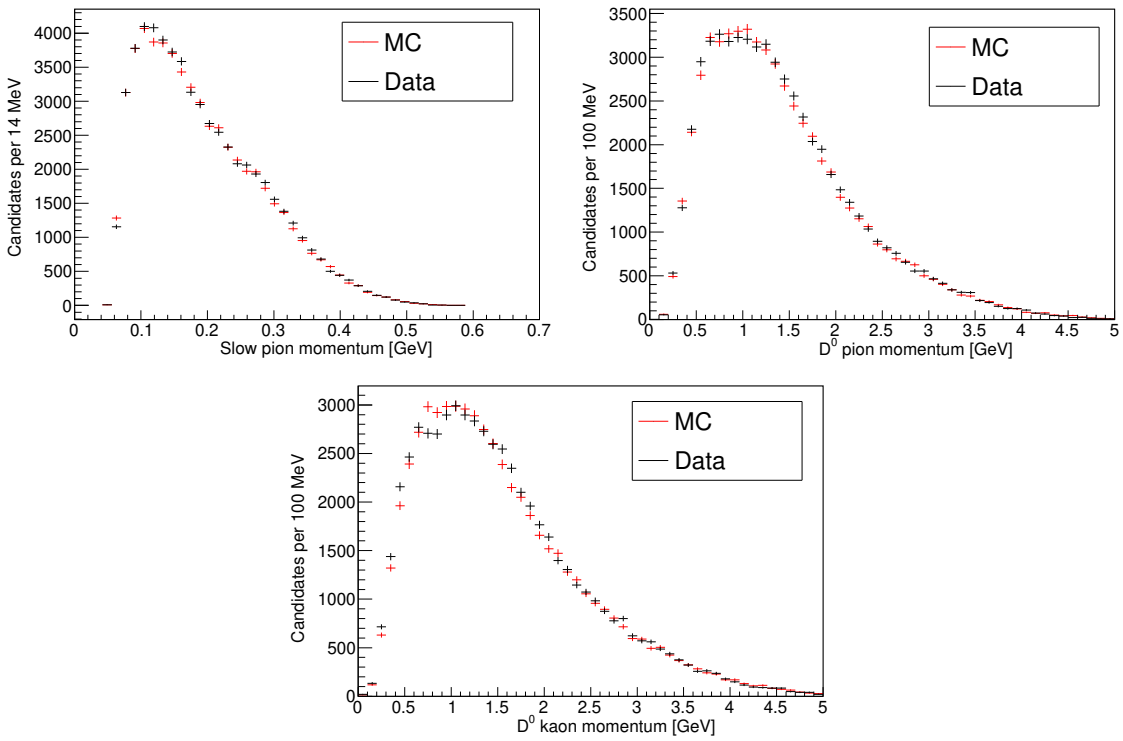

Figure 12.3: Comparison of kaon and pion momentum between data and simulation events with the latter scaled to the number of data events.

12.3 SVD dE/dx calibration

12.3.1 Reconstruction of dE/dx

The energy loss due to ionization by a charged particle is proportional to the distance it traversed in the detector medium, so the cluster charge divided by the distance or the path length is used to calculate dE/dx. This is not exactly equal to the specific ionization, rather both are related by a detector-dependent constant. The path length is defined as $s = d/\cos\phi$, where d is the thickness of the silicon sensor, and ϕ is the angle between the normal vector to the sensor and the track (Fig. 12.4) [86] The momentum of the track at its hit position is used to calculate the above angle. The position and momentum of each particle hit are available through the track representation of fitted tracks. The cluster charge information of each hit is also provided by the hit class as assigned to the track.

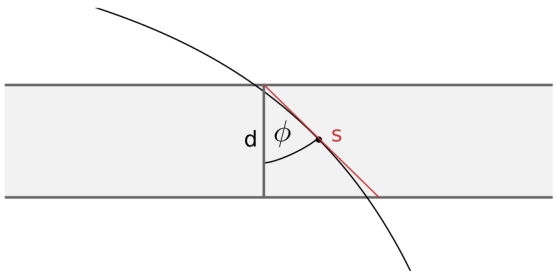

Figure 12.4: Schematic of the path of a charged track and the distance traversed in a silicon sensor.

The dE/dx value obtained from each SVD hit for a given charged particle follows a Landau distribution [87]; an example is shown in Fig. 12.5. The hit-level dE/dx information is then combined to reconstruct the track-level dE/dx value. It turns out that a simple arithmetic mean would be insufficient as the mean of the Landau distribution is undefined. Thus we need to apply some sort of truncation while combining the individual hit-level dE/dx measurements. When a particle traverses through the entire SVD, we get at least eight dE/dx values: four for the U side and four for the V side. To get a better truncation of dE/dx, we use the energy of all clusters except for the two highest ones. To verify this point, in Fig. 12.6 we compare the dE/dx distributions truncated after removing only the highest and two highest dE/dx values. It is evident that the truncation works better when we remove the two highest dE/dx values than removing only the highest dE/dx value. Indeed, removing just a single hit will not make any sense as the two highest hits come from the same wafer and are fully correlated.

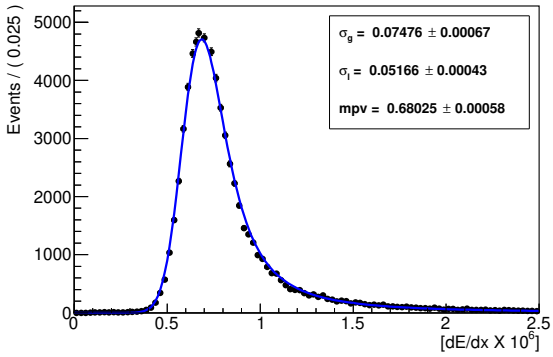

Figure 12.5: dE/dx distribution for pions in the momentum range 300–315 MeV fitted to a Landau convolved with a Gaussian function.

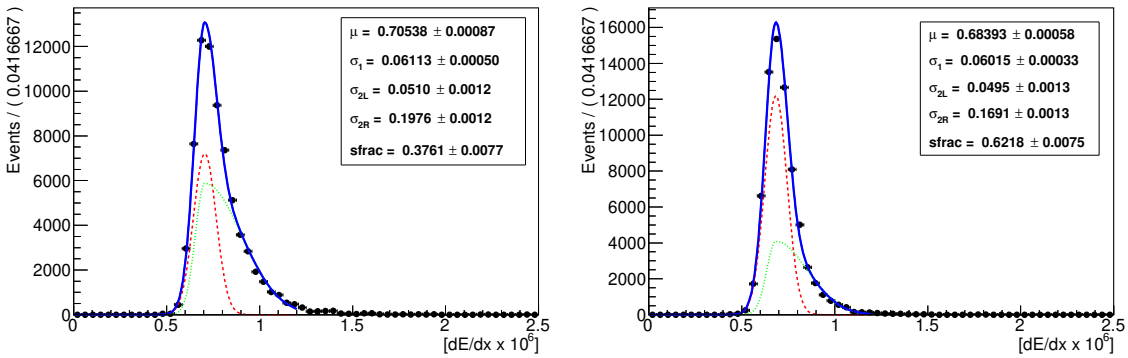

Figure 12.6: dE/dx distributions for pions in the momentum range 300–315 MeV (left and right after removing one and two dE/dx values, respectively) fitted to the sum of a Gaussian and an asymmetric Gaussian function.

12.3.2 Likelihood-based PID method

The likelihood-based PID method [86] is based on a two-dimensional PDF. For this, we need to construct a likelihood function for each particle hypothesis m:

$$\mathcal{L}_m\left(\mathrm{d}E/\mathrm{d}x, p\right) = \prod_i \mathcal{P}_m\left[\left(\mathrm{d}E/\mathrm{d}x\right)_i, p\right], \tag{12.2}$$

where $m = \pi$, K, and i runs over all dE/dx values assigned to a track. For each track, the likelihood for each particle type is given by the interpolated value of the appropriate PDF, which is nothing but a two-dimensional histogram of dE/dx vs. momentum for various particle hypotheses. Such PDFs are updated in the database as payloads. The scatter plot of dE/dx as a function of momentum in data and MC events (Fig. 12.7) shows a clear separation between kaon and pion bands below 0.6 GeV. Next, we look at the mean dE/dx values for different particles in narrow momentum bins of 15 MeV as shown in Fig. 12.8. We notice some data-simulation

difference for the mean of the dE/dx distribution. The dE/dx is proportional to the energy deposited by a charged particle passing through the SVD, or the SVD cluster charge, where there is a known issue with simulation [42] and work is underway to improve the overall data-simulation agreement. Once it is fixed, we believe that there will be a better data-simulation agreement for dE/dx distributions.

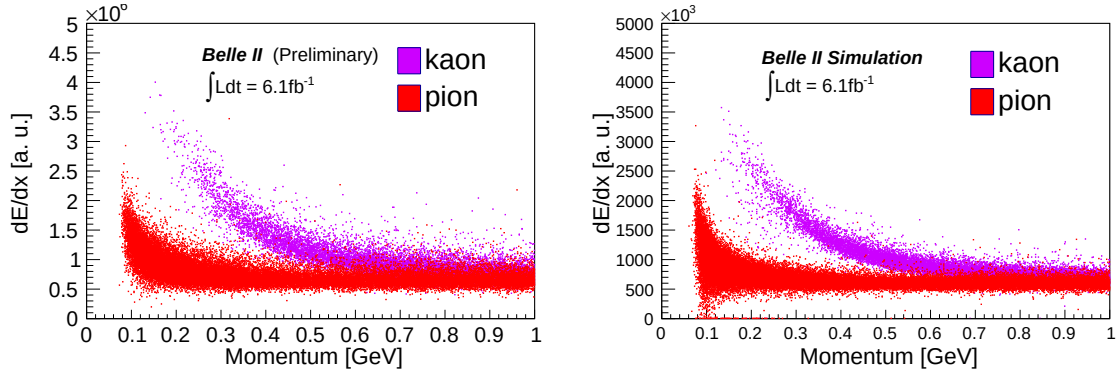

Figure 12.7: Scatter plot of dE/dx values of charged pions and kaons as a function of their momentum for data (left) and simulation (right) events.

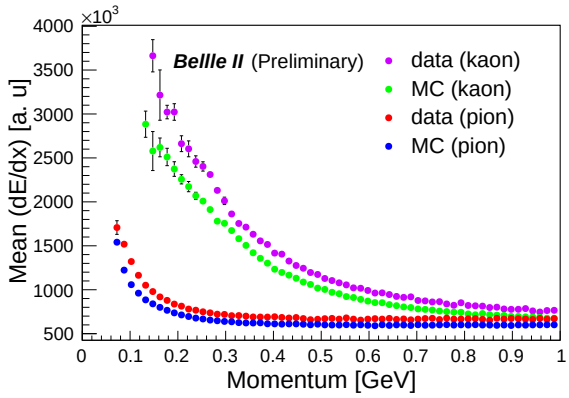

Figure 12.8: dE/dx mean of pions and kaons as a function of their momentum.

12.4 SVD PID performance

12.4.1 Efficiency and fake rate

To assess the impact of SVD $\mathrm{d}E/\mathrm{d}x$ information on the overall PID, we prepare a separate sample with SVD PID information. To assess the impact of SVD $\mathrm{d}E/\mathrm{d}x$ information on the overall PID performance, we plot the identification efficiency and fake rate as a function of momentum applying a requirement on the binary PID likelihood $\mathcal{L}(i/j) > 0.5$. The efficiency is defined as:

$$\epsilon_i = \frac{\text{\# tracks identified kinematically and with PID requirement under the hypo. } i}{\text{\# tracks identified kinematically under the hypo. } i} \tag{12.3}$$

and the fake rate is given by:

$$f_{j\to i} = \frac{\text{\# j tracks identified kinematically and with PID requirement under the hypo. } i}{\text{\# tracks identified kinematically under the hypo. } j} \tag{12.4}$$

The PID is assigned based on a criterion on the likelihood ratio, defined in terms of binary ID:

$$\text{Binary ID} = \frac{\mathcal{L}_{\text{hypo1}}}{\mathcal{L}_{\text{hypo1}} + \mathcal{L}_{\text{hypo2}}} \tag{12.5}$$

Information from different subdetectors including SVD is added at the level of log-likelihoods:

$$\ln \mathcal{L}_h^{\text{all}} = \ln \mathcal{L}_h^{\text{SVD}} + \ln \mathcal{L}_h^{\text{CDC}} + \ln \mathcal{L}_h^{\text{TOP}} + \ln \mathcal{L}_h^{\text{ARICH}} \tag{12.6}$$

Using this information we evaluate the PID performance with and without SVD log-likelihood $\ln \mathcal{L}_h^{\text{SVD}}$. As already noted earlier, the SVD is useful in the low momentum region especially below 1 GeV. We first check the kaon ID distributions in the low momentum region (< 1.0 GeV). The binary kaon ID $\mathcal{L}(K/\pi)$ distributions for SVD alone in this region are shown in Fig. 12.9. Figure 12.10 shows the same distributions including all subdetectors and all except SVD.

Thanks to the good resolution of SVD $\mathrm{d}E/\mathrm{d}x$, we are able to get a decent separation between pions and kaons. To assess the impact of adding SVD information to the overall binary ID, we plot the efficiency and fake rate as a function of momentum with a threshold of 0.5 on the binary ID. The study shows an improvement in efficiency after adding SVD information. The distributions with and without SVD binary ID for kaon identification efficiency and pion fake rate in bins of momentum and polar angle ($\cos\theta$) are shown in Fig. 12.11. We also plot the fake rate as a function of efficiency (ROC curve) to better appreciate this improvement. We choose a momentum range up to 1 GeV and vary the binary ID from 0 to 1 in order to produce the

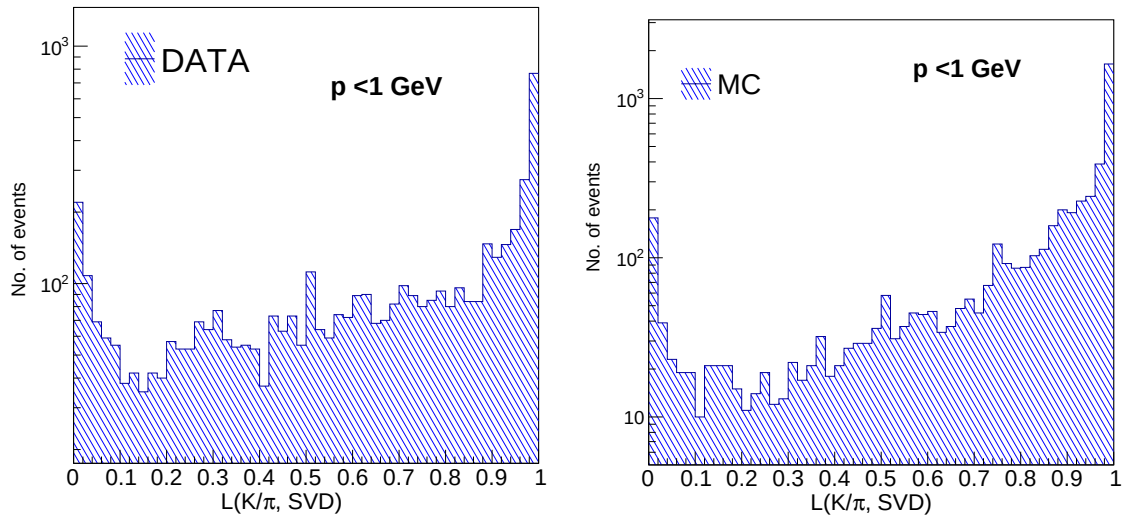

Figure 12.9: Binary kaon ID distribution in data (left) and simulation (right) events for SVD alone for a momentum less than 1 GeV

.

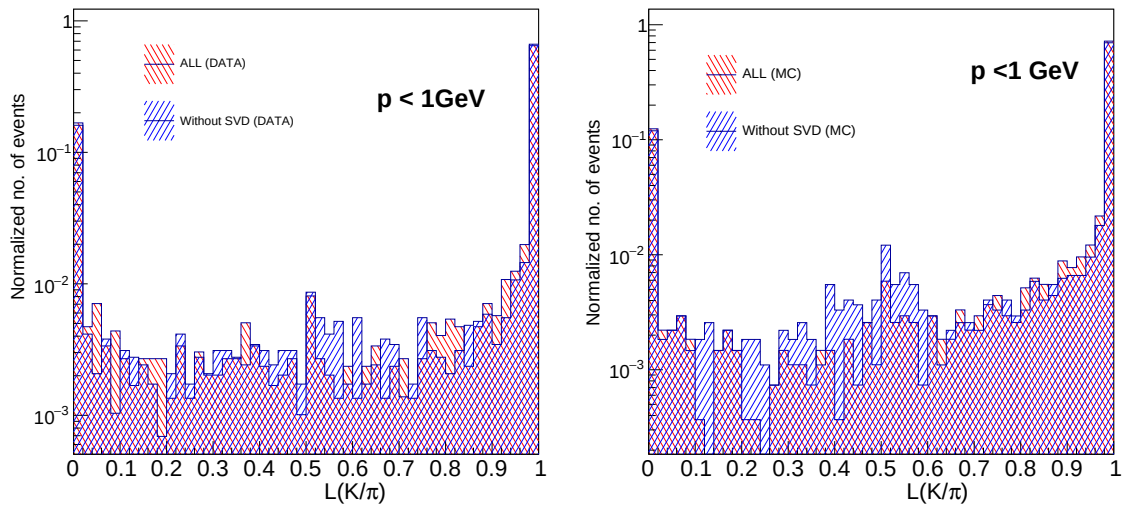

Figure 12.10: Binary kaon ID distributions in data (left) and simulation (right) events for a momentum less than 1 GeV

.

ROC curve. In the ROC curve, each point represents a pair of efficiency and fake rate values for a given PID criterion. The ROC curve (Figs. 12.12) confirms that for a given efficiency value the fake rate decreases or alternatively, for a given fake rate value the efficiency increases after adding the SVD PID to the overall PID. This confirms that adding SVD $\mathrm{d}E/\mathrm{d}x$ based PID improves the overall pion and kaon ID efficiency in the low momentum region.

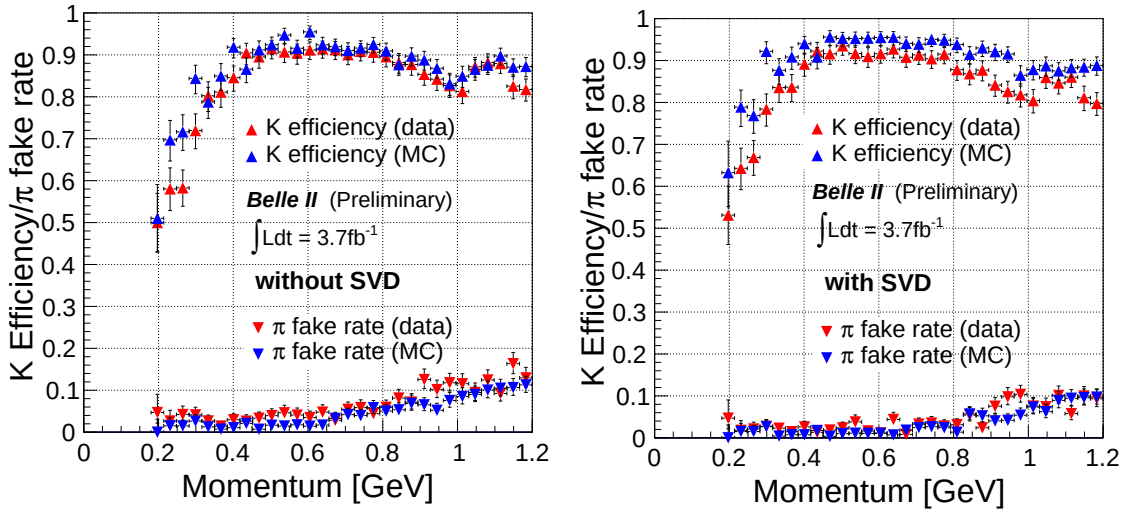

Figure 12.11: K efficiency and π fake rate vs momentum without (left) and with (right) SVD for binary ID $\mathcal{L}(K/\pi) > 0.5$.

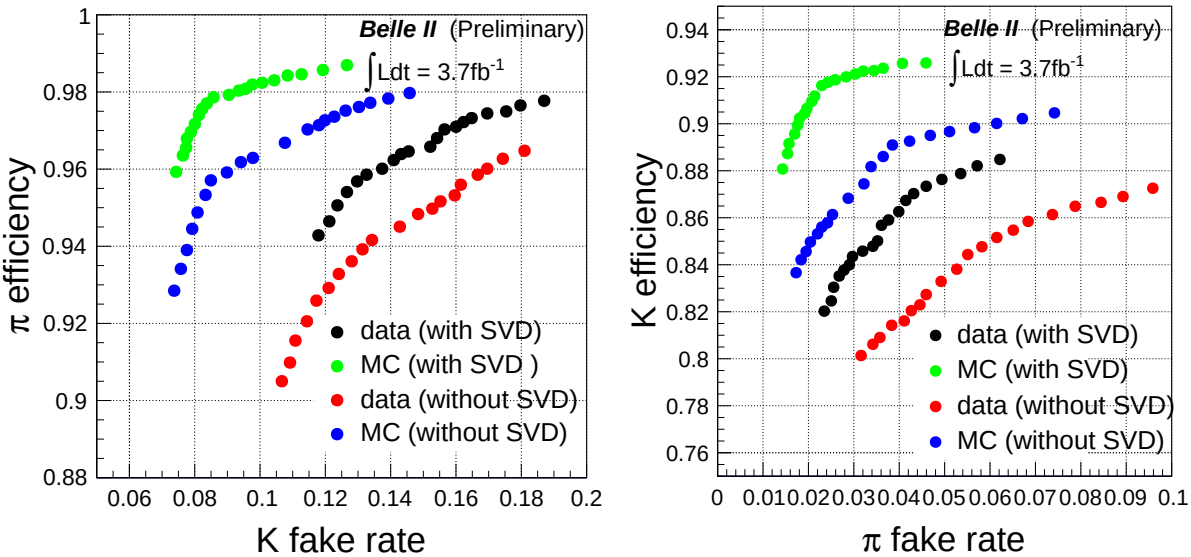

Figure 12.12: Efficiency vs. fake rate with and without SVD for a momentum less than 1 GeV.

12.5 Summary

We undertake a study on how to improve the PID performance for charged hadrons using information from the SVD of the Belle II experiment. Our study confirms that the addition of $\mathrm{d}E/\mathrm{d}x$ information improves the pion and kaon efficiency for a given fake rate in the low momentum region.

Chapter 13

Conclusion

As part of my Ph.D. thesis, I have mainly worked on two projects. On the physics side, we performed the first measurement of *CP* violation in the $B^0 \to K_S^0\pi^0$ decay at Belle II using 362 fb^{-1} data sample. With a signal yield of 415^{+26}_{-25} events, we determine $\mathcal{B} = (11.15^{+0.69}_{-0.67} \pm 0.61) \times 10^{-6}$, $C = -0.04^{+0.14}_{-0.15} \pm 0.05$ and $S = 0.75^{+0.20}_{-0.23} \pm 0.04$, where the first uncertainty represents the statistical and the second uncertainty corresponds to the systematic. Importantly, this constitutes the first Belle II measurement of *CP* asymmetries in this specific decay channel. Our results not only agree with previous determinations [35, 36] but also exhibit a notable improvement in precision for S when compared to the earlier Belle and *BABAR* experiments, despite using a data sample that is 60–80% of the size of their respective datasets. This enhanced precision is primarily due to the increased acceptance of the vertex detector, which has facilitated more accurate K_S^0 reconstruction, and more effective suppression of continuum background. These results agree with the SM expectations and provide important constraints on physics beyond the SM. This result has been published in the Physical Review Letters. On the detector side, we have developed a PID framework using specific ionization information of the SVD subdetector at Belle II. PID plays an important role in the physics program of the Belle II experiment. Particles with low momentum cannot reach the CDC, the primary tracking subdetector of the experiment, due to the significant curvature in their trajectory. We use the specific ionization ($\mathrm{d}E/\mathrm{d}x$) of these low-momentum particles within SVD for their identification. We find the addition of SVD information provides complementary information towards low-momentum pion and kaon identification. This result has been published in the Journal of Instrumentation.

Appendix A

Suplementary information related to BDT training

The significance of the BDT input variables can be found in Table A.1. The distribution of BDT input variables for both signal and background events are shown in Figs. A.1-A.4.

Table A.1: Importance of BDT variables

Ranking	variables
1	cosTBTO
2	KSFWVariables(hso02)
3	KSFWVariables(hso12)
4	R2
5	KSFWVariables(hoo2)
6	thrustAxisCosTheta
7	thrustOm
8	CleoConeCS(2,ROE)
9	cosTBz
10	KSFWVariables(hso20)
11	cosHelicityAngleMomentum
12	KSFWVariables(hso04)
13	KSFWVariables(hso22)
14	CleoConeCS(3,ROE)
15	KSFWVariables(hoo0)
16	KSFWVariables(et)
17	KSFWVariables(hso24)
18	KSFWVariables(hso10)
19	KSFWVariables(hso14)
20	KSFWVariables(hso00)
21	KSFWVariables(hoo1)
22	KSFWVariables(mm2)
23	CleoConeCS(7,ROE)
24	useCMSFrame__bocosTheta__bc
25	CleoConeCS(4,ROE)
26	KSFWVariables(hoo4)
27	KSFWVariables(hoo3)
28	CleoConeCS(6,ROE)
29	CleoConeCS(9,ROE)
30	CleoConeCS(8,ROE)
31	CleoConeCS(5,ROE)

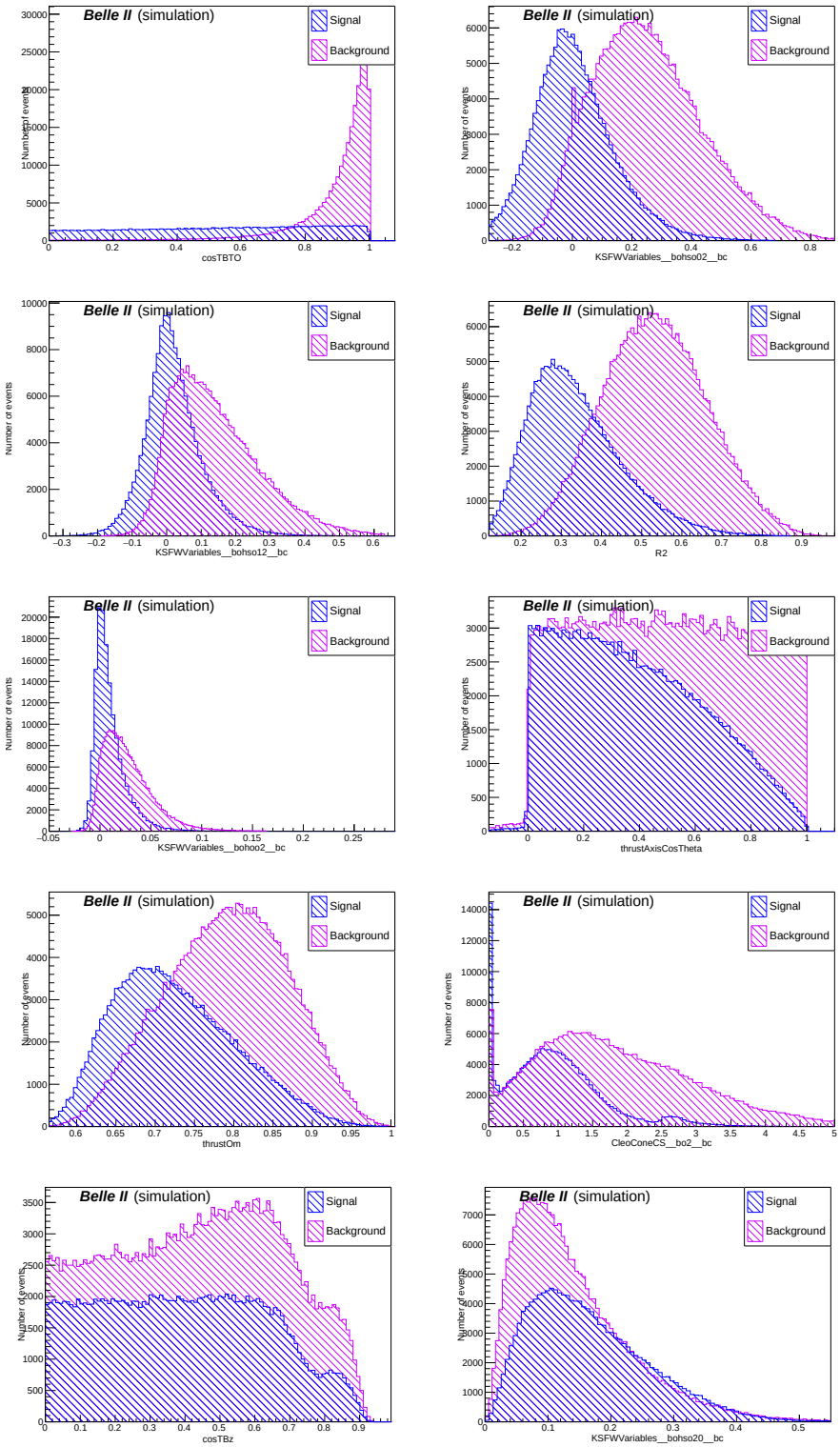

Figure A.1: Comparison of BDT input variables between signal and background simulated $B^0 \to K_S^0 \pi^0$ events.

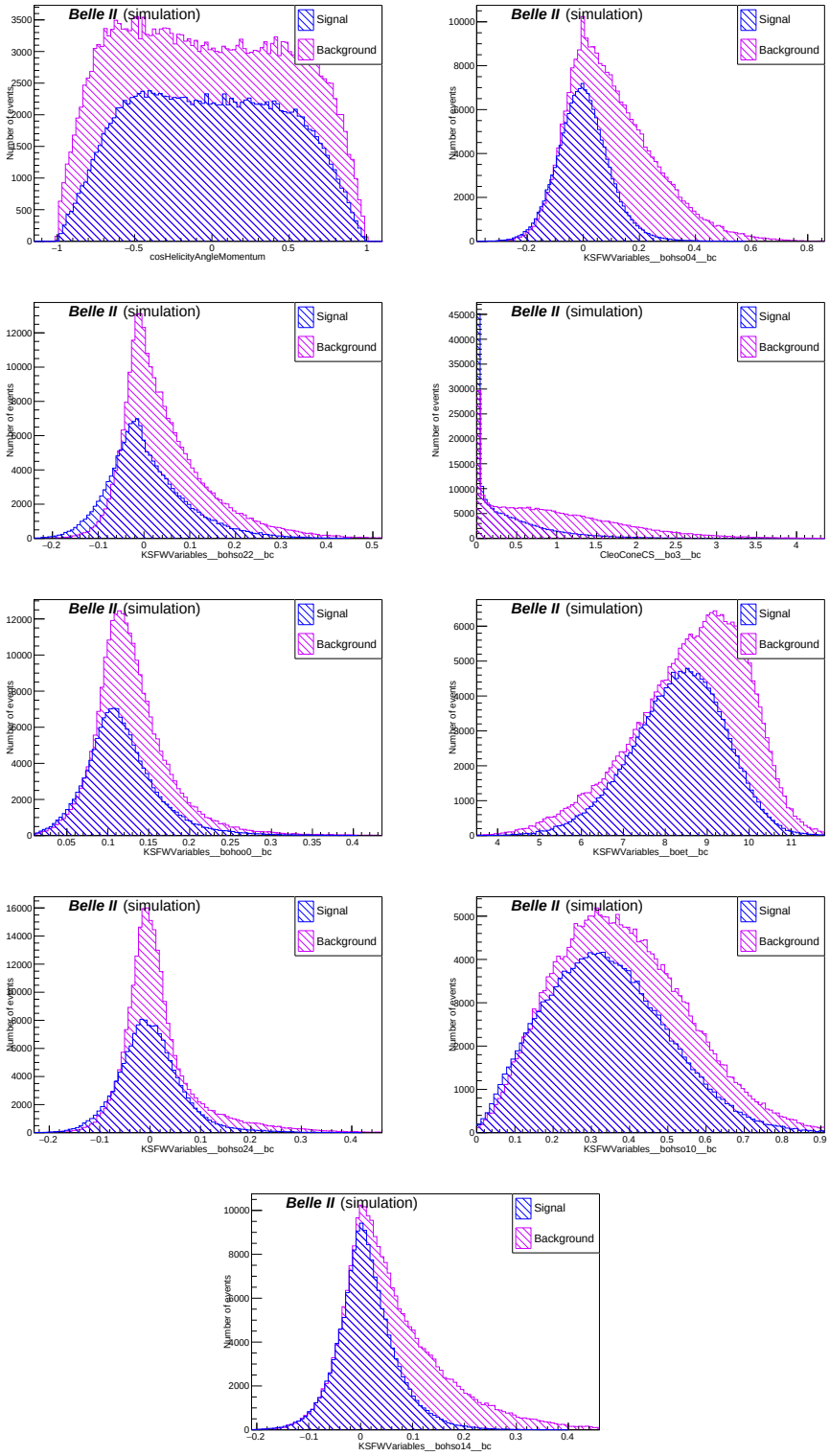

Figure A.2: Comparison of BDT input variables between signal and background simulated $B^0 \to K_S^0 \pi^0$ events.

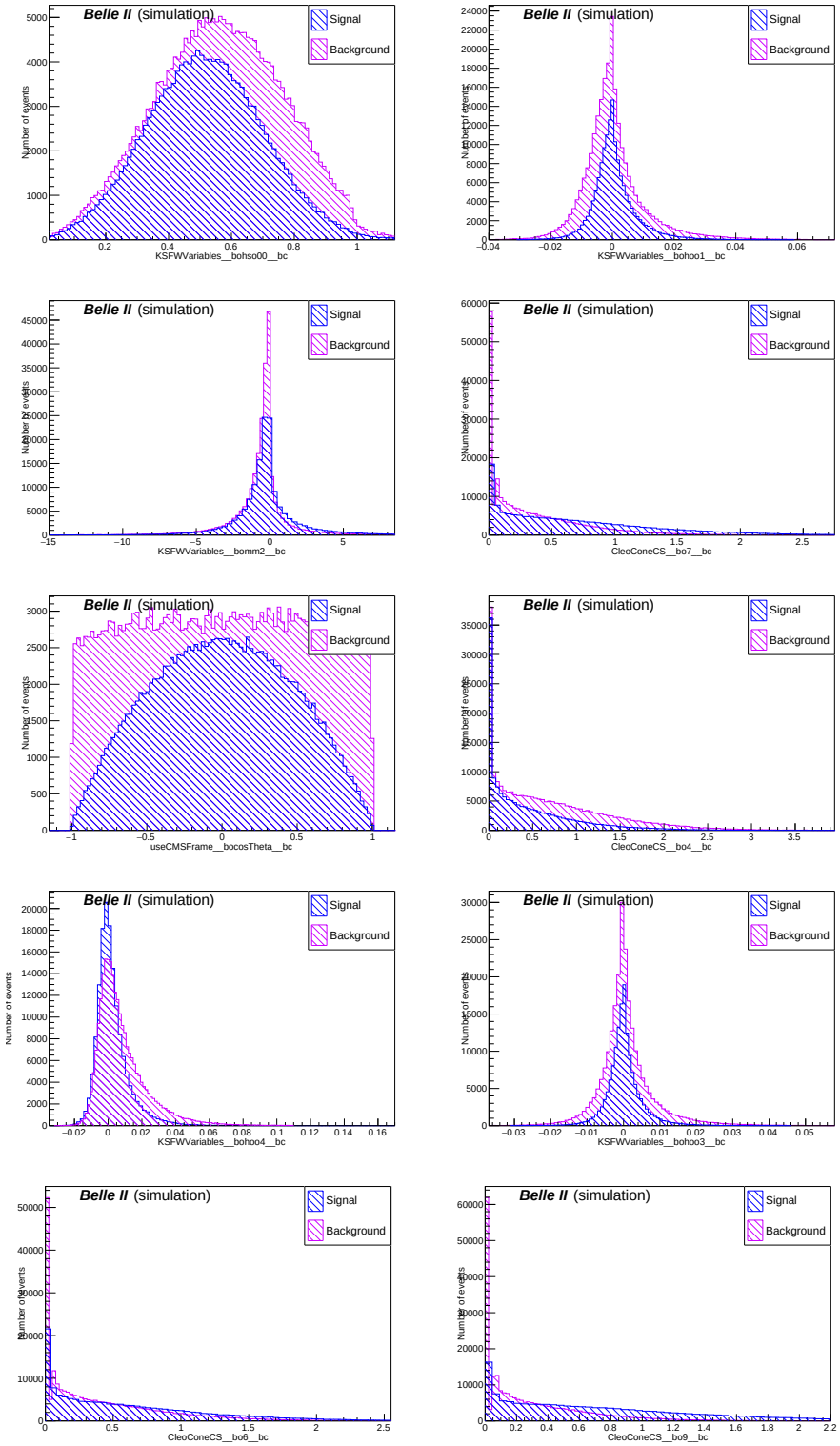

Figure A.3: Comparison of BDT input variables between signal and background simulated $B^0 \to K_S^0 \pi^0$ events.

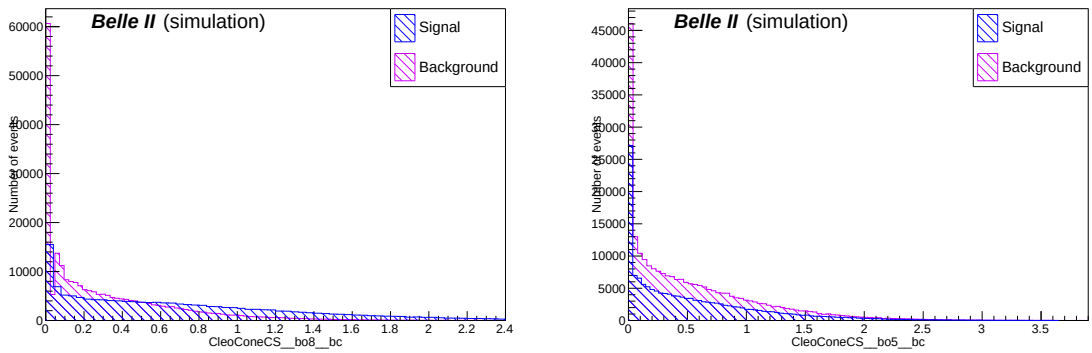

Figure A.4: Comparison of BDT input variables between signal and background simulated $B^0 \to K_S^0 \pi^0$ events.

Appendix B

Supplementary information related to fit

B.1 Fit variables distribution across $q \cdot r$ bin

We compare the shapes of fit variables across various $q \cdot r$ bins for both $B\overline{B}$ and $q\overline{q}$, and find them to be consistent within their respective statistical uncertainties. The distributions of fit variable shapes are shown in Figs. B.1 and B.2.

B.2 Δt distribution between signal and sideband region

We compare the Δt distributions between the signal region and sideband in the simulation. The observed distributions are consistent between the two regions, as shown in Fig. B.3.

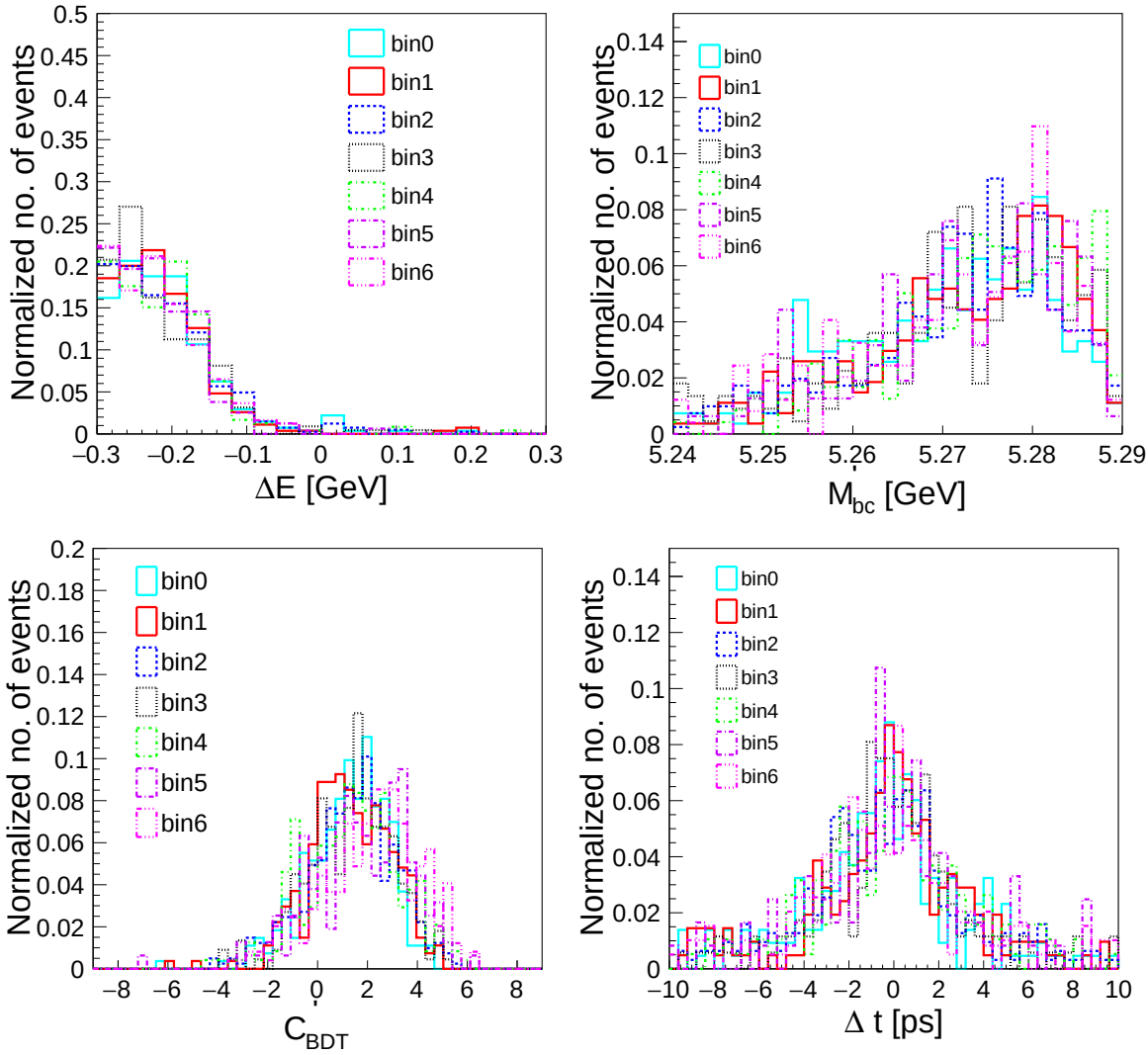

Figure B.1: The distribution of fit variables shapes in $B\overline{B}$ background events.

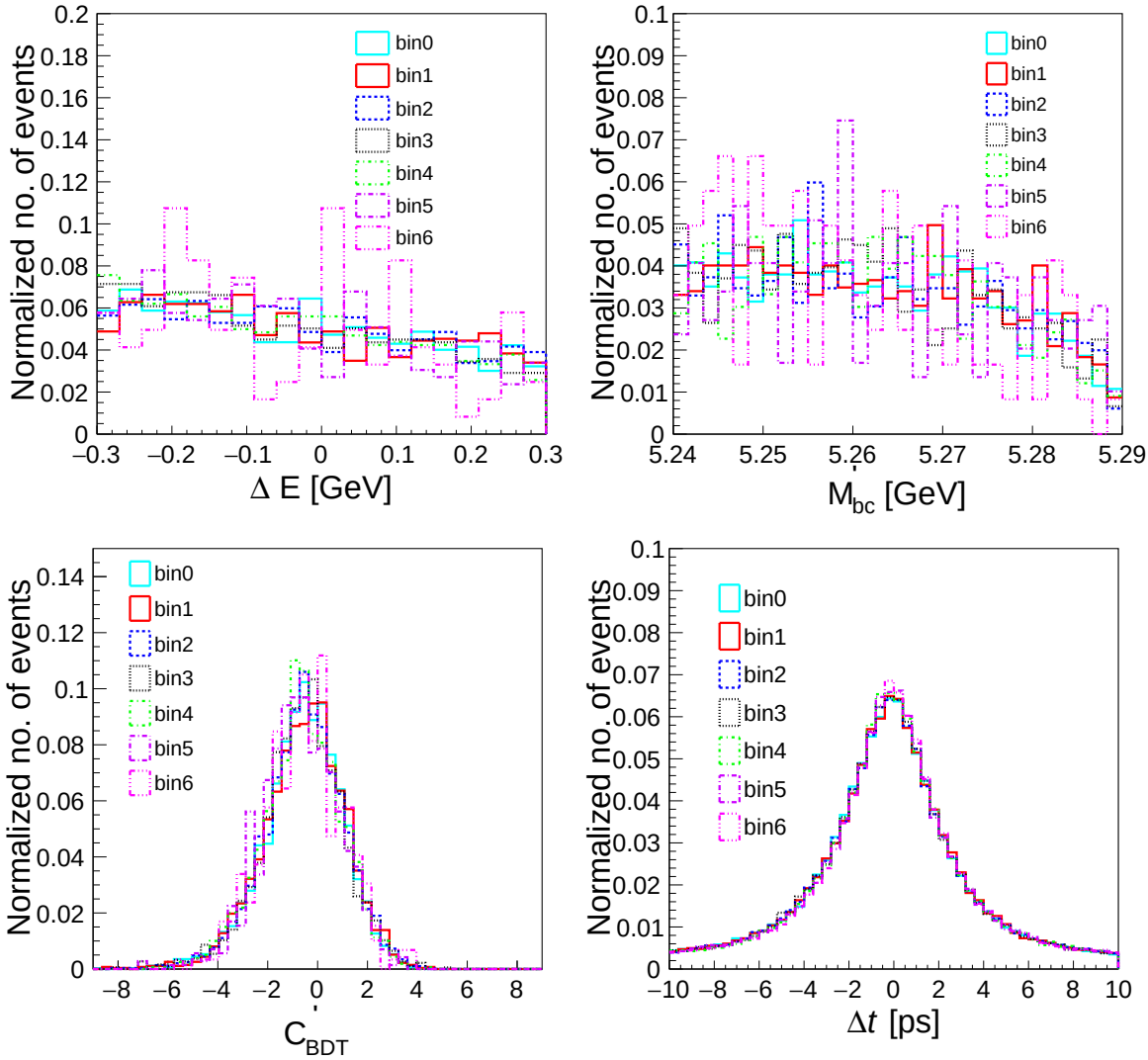

Figure B.2: The distribution of fit variables shapes in $q\bar{q}$ background events.

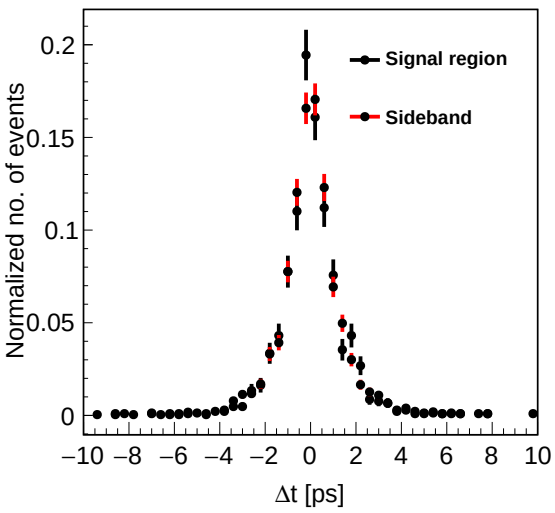

Figure B.3: Distribution of Δt shape between signal and sideband region.

B.3 C and S results for TD and TI subsamples

We also separate the C and S results for TD and TI subsamples to validate the impact of combined results. We find

$$C = 0.13 \pm 0.18, \tag{B.1}$$

and

$$S = 0.75^{+0.20}_{-0.23}, \tag{B.2}$$

and

$$C = -0.30^{+0.26}_{-0.25}, \tag{B.3}$$

for TD and TI subsamples. We find individual results are consistent with combined result within systematic uncertainties.

Appendix C

Supplementary information related to SVD $\mathrm{d}E/\mathrm{d}x$

C.1 ROC plot

As a validation, we generate ROC curves (Figs. C.1) for tracks with momenta ranging from 1.5 to 2.5 GeV. We expect for high-momentum tracks, the black and red (green and blue) points for data (MC) should overlap. Our findings agree with expectations, confirming the validity of the analysis.

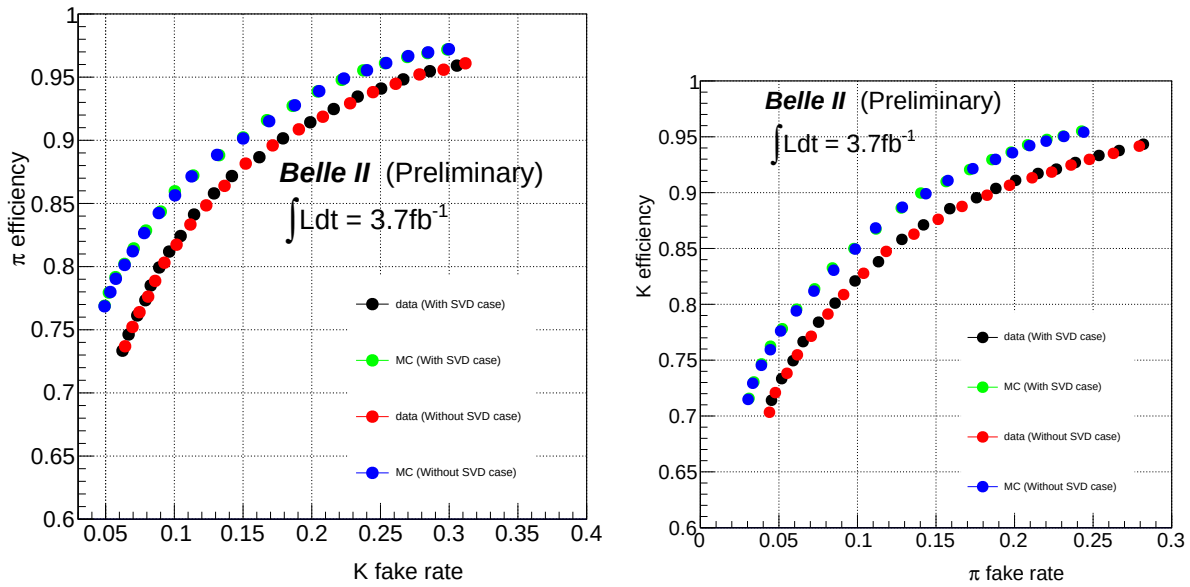

Figure C.1: Efficiency vs. fake rate with and without SVD for a momentum ranging from 1.5 to 2.5 GeV.

C.2 Truncation of $\mathrm{d}E/\mathrm{d}x$ distribution

We check the truncation of $\mathrm{d}E/\mathrm{d}x$ distribution in Fig. C.2 after removing four $\mathrm{d}E/\mathrm{d}x$ values. We find the $\mathrm{d}E/\mathrm{d}x$ truncation as well as resolution is poor for this case.

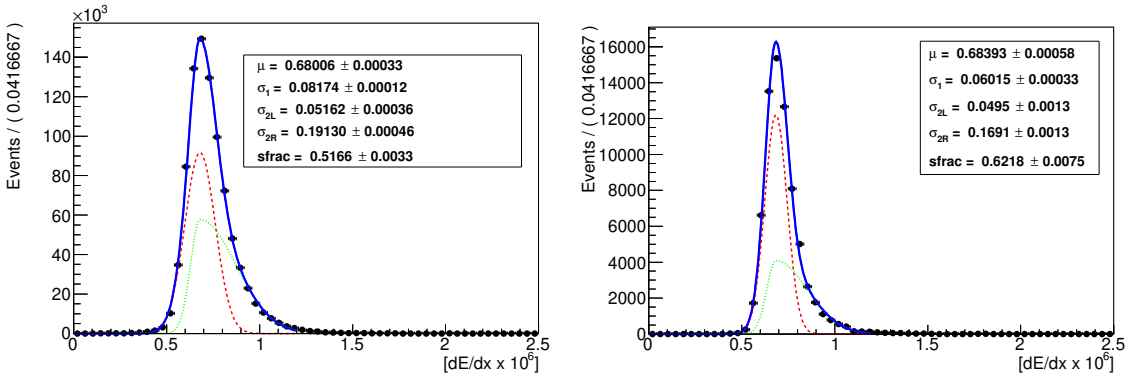

Figure C.2: $\mathrm{d}E/\mathrm{d}x$ distributions for pions after removing four (left) and two (right) $\mathrm{d}E/\mathrm{d}x$ values, fitted to the sum of a Gaussian and an asymmetric Gaussian function.

Bibliography

[1] G. L. Glashow, Nucl. Phys. **22**, 579 (1961).

[2] A. Salam and J. C. Ward, Phys. Lett. **13**, 168 (1964).

[3] S. Weinberg, Phys. Rev. Lett. **19**, 1264 (1967).

[4] R. L. Workman *et al*. (Particle Data Group), Prog. Theor. Exp. Phys. **2022**, 083C01 (2022).

[5] M. Gronau, Phys. Lett. B **627**, 82 (2005).

[6] R. Aaij et al. (LHCb Collaboration), Phys. Rev. Lett. **126**, 091802 (2021).

[7] A.D. Sakharov, Sov. Phys. JETP Lett. **5**, 24 (1967); A. D. Sakharov, Sov. Phys. JETP **49**, 594 (1979).

[8] T. D. Lee and C. N. Yang, Phys. Rev. **104**, 254 (1956).

[9] C. S. Wu, E. Ambler, R. W. Hayward, D. D. Hoppes, and R. P. Hudson, Phys. Rev. Lett. **105**, 1413 (1957).

[10] J. H. Christenson, J. W. Cronin, V. L. Fitch, and R. Turlay, Phys. Rev. Lett. **13**, 138 (1964).

[11] N. Cabibbo, Phys. Rev. Lett. **10**, 531 (1963).

[12] S. L. Glashow, J. Iliopoulos, and L. Maiani, Phys. Rev. D. **2**, 1285 (1970).

[13] J.-E. Augustin *et al*., Phys. Rev. Lett. **33**, 1406 (1974); J. J. Aubert *et al*. Phys. Rev. Lett. **33**, 1404 (1974).

[14] M. Kobayashi and T. Maskawa, Prog. Theor. Phys. **49**, 652 (1973).

[15] L. Wolfenstein, Phys. Rev. Lett. **51**, 1945 (1985).

[16] CKM fitter, Moriond 2021, `http://ckmfitter.in2p3.fr/www/results/plots_spring21/ckm_res_spring21.html`

[17] K. Abe *et al.*, (Belle Collaboration), Phys. Rev. Lett. **87**, 091802 (2001).

[18] B. Aubert *et al.*, (BABAR Collaboration), Phys. Rev. Lett. **87**, 091801 (2001).

[19] G. R. Farrar and M. E. Shaposhnikov, Phys. Rev. D **50**, 774 (1994).

[20] M. B. Gavela et al., Nucl. Phys. B **430**, 382 (1994).

[21] P. Huet and E. Sather, Phys. Rev. D **51**, 379 (1995).

[22] N. Cabibbo, Phys. Rev. Lett. **10**, 531 (1963).

[23] M. Kobayashi and T. Maskawa, Prog. Theo. Phys. **49**, 652 (1973).

[24] Y. Grossman and M. P. Worah, Phys. Lett. B **395**, 241 (1997).

[25] D. London and A. Soni, Phys. Lett. B **407**, 61 (1997).

[26] M. Beneke, Phys. Lett. B **620**, 143 (2005).

[27] M. Beneke and M. Neubert, Nucl. Phys. B **675**, 333 (2003).

[28] C.-W. Chiang, M. Gronau, and J. L. Rosner, Phys. Rev. D **68**, 074012 (2003); M. Gronau, J. L. Rosner, and J. Zupan, Phys. Lett. B **596**, 107 (2004).

[29] Y. Amhis *et al.* (Heavy Flavor Averaging Group), Phys. Rev. D **107**, 052008 (2023).

[30] M. Gronau, Phys. Lett. B **627**, 82 (2005).

[31] R. Aaij et al. (LHCb Collaboration), Phys. Rev. Lett. **126**, 091802 (2021).

[32] M. Beneke, Phys. Lett. B **620**, 143 (2005).

[33] M. Gronau, J. L. Rosner, and J. Zupan, Phys. Rev. D **74**, 093003 (2006).

[34] R. Fleischer, R. Jaarsma, and K. Keri Vos, Phys. Lett. B **785**, 525 (2018).

[35] B. Aubert *et al.* (*BABAR* Collaboration), Phys. Rev. D **79**, 052003 (2009).

[36] M. Fujikawa *et al.* (Belle Collaboration), Phys. Rev. D **81**, 011101(R) (2010).

[37] T. Abe *et al.* (Belle II Collaboration), KEK Report 2010-1, arXiv:1011.0352.

[38] E. Kou *et al.*, Prog. Theor. Exp. Phys. **2019**, 123C01 (2019).

[39] K. Akai, K. Furukawa, and H. Koiso (SuperKEKB Group), Nucl. Instrum. Meth. A **907**, 188 (2018).

[40] M. Baszczyk et al. SuperB Technical Design Report. 2013, arXiv:1306.5655

[41] J. Kemmer and G. Lutz, Nucl. Instrum. Meth. A **253** (1987) 365.

[42] K. Adamczyk *et al.* (Belle II SVD Collaboration), JINST **17**, P11042 (2022).

[43] W. R. Leo, "Techniques for Nuclear and Particle Physics Experiments", Springer-Verlag (1994).

[44] I. Adachi *et al.*, Nucl. Instrum. Meth. Phys. Res. A **907**, 46-59 (2018).

[45] K. Inami, Nucl. Instrum. Meth. A **595**, 96 (2008).

[46] B. N. Ratcliff, Nucl. Instrum. Meth. A **502**, 211 (2003).

[47] M. Staric *et al.*, Nucl. Instrum. Meth. A **595**, 252-255 (2008).

[48] T. Matsumoto *et al.*, Nucl. Instrum. Meth. Phys. Res. A **521**, 367 (2004).

[49] T. Iijima *et al.*, Nucl. Instrum. Meth. Phys. Res. A **548**, 383 (2005).

[50] S. Iwata *et al.*, Prog. Theor. Exp. Phys. **2016**, 033H01 (2016) .

[51] A. Abashian *et al.*, Nucl. Instrum. Meth. Phys. Res. A **449**, 112 (2000).

[52] A. Abashian et al., Nucl. Instrum. Meth. Phys. Res. A **479**, 117 (2002).

[53] D. Lange, Nucl. Instrum. Meth. A **462**, 152 (2001).

[54] E. Barberio, B. van Eijk, and Z. Was, Comp. Phys. Comm. **66**, 115 (1991).

[55] B. Ward, S. Jadach, and Z. Was, Nucl. Phys. B Proc. Suppl. **116**, 73 (2003)

[56] T. Sjöstrand, S. Mrenna, and P. Skands, Comp. Phys. Comm. **178**, 852 (2008).

[57] S. Agostinelli et al. (GEANT4 Collaboration), Nucl. Instrum. Meth. A **506**, 250 (2003).

[58] T. Kuhr, C. Pulvermacher, M. Ritter, T. Hauth, and N. Braun (Belle II Framework Software Group), Comput. Software Big Sci. 3, 1 (2019).

[59] `https://doi.org/10.5281/zenodo.5574115`

[60] T. Schlüter and M. Prim, The Belle II V0 Finder , Oct, 2015. BELLE2-NOTE-TE-2015-034.

[61] T. Keck, arXiv:1609.06119.

[62] T. Keck et al., arXiv:1609.06119 (2016).

[63] W. D. Hulsbergen, Nucl. Instrum. Meth. **552**, 566 (2005).

[64] J.-F. Krohn et al. (Belle II Analysis Software Group), Nucl. Instrum. Meth. **A976**, 164269 (2020).

[65] W. Waltenberger, W. Mitaroff, F. Moser, B. Pflugfelder, and H. V. Riedel, Journal of Physics: Conference Series **119**, 032037 (2008).

[66] G. C. Fox and S. Wolfram, Phys. Rev. Lett. **41**, 1581 (1978).

[67] D. M. Asner et al. (CLEO Collaboration), Phys. Rev. D **53**, 1039 (1996).

[68] T. Humair et al, Measurement of the B^0 lifetime and mixing frequency using hadronic decays with the moriond 2022 dataset. BELLE2-NOTE-PH-2021-046, Oct 2021.

[69] F. Abudinén et al. (Belle II Collaboration), Eur. Phys. J. C **82**, 283 (2022).

[70] A. J. Bevan et al. (*BABAR* and Belle Collaboraton), Eur. Phys. J. C **74**, 3026 (2014).

[71] T. Skwarnicki, PhD thesis, INP Krakow, DESY-F31-86-02 (1986).

[72] H. Albrecht et al. (ARGUS Collaboration), Phys. Lett. B **241**, 278 (1990).

[73] K. S. Cranmer, Comp. Phys. Comm. **136**, 198 (2001).

[74] F. Abudinén *et al*. (Belle II Collaboration), arXiv:2302.12898.

[75] S. Choudhury *et al*. (Belle Collaboration), Phys. Rev. D **107**, L031102 (2023).

[76] I. Adachi *et al*. (Belle II Collaboration), arXiv:2310.06381.

[77] F. Abudinén et al. (Belle II Collaboration), BELLE2-CONF-PH-2021-001, arXiv:2104.14871.

[78] M. Pivk and F. R. Le Diberder, Nucl. Instrum. Meth. A **555**, 356 (2005).

[79] V. Bertacchi et al. (Belle II Tracking Group), Comp. Phys. Comm. **259**, 107610 (2021).

[80] G. Bonvicini et al. (CLEO Collaboration), Phys. Rev. D **89**, 072002 (2014).

[81] L. Šantelj et al. (Belle Collaboration), JHEP **10**, 165 (2014).

[82] O. Long, M. Baak, R. N. Cahn, and D. P. Kirkby, Phys. Rev. D **68**, 034010 (2003).

[83] F. pham et al, Measurement of $B^0 \to \pi^0\pi^0$ branching fraction and C in 2019-2021 Belle II data, BELLE2-NOTE-PH-2021-009.

[84] F. Abudinén *et al*. (Belle II Collaboration), Phys. Rev. Lett. **127**, 211801 (2021).

[85] M. Pivk and F. R. Le Diberder, Nucl. Instrum. Meth. A555, 356 (2005).

[86] C. Pulvermacher, Diploma thesis, KIT, Germany (2012) `https://ekp-invenio.physik.uni-karlsruhe.de/record/48263`.

[87] L. Landau, J. Phys. (USSR) 8 (1944) 201.